Theory of Disks and Outflows around Massive Young Stellar Objects

Bhargav Vaidya
Max-Planck-Institut für Astronomie

Heidelberg 2011

Dissertation in Astronomy

SUBMITTED TO THE

COMBINED FACULTIES OF THE NATURAL SCIENCES AND MATHEMATICS

OF THE RUPERTO-CAROLA-UNIVERSITY OF HEIDELBERG, GERMANY,

FOR THE DEGREE OF

Doctor of Natural Sciences

PUT FORWARD BY

Bhargav Vaidya

BORN IN JALNA, INDIA

ORAL EXAMINATION: 26.10.11

Theory of Disks and Outflows around Massive Young Stellar Objects

Referees: **Priv. Doz. Dr. Christian Fendt**
Prof. Dr. Cornelis Dullemond

To my parents

Abstract

The inner most regions around massive young stellar objects (YSO) are associated with complex interactions between numerous physical processes. Since the inner few Astronomical Units (AU) are tough to resolve observationally, a theoretical approach is important to create a qualitative picture for these regions around young high-mass stars. This thesis investigates the interplay between important physical processes with respect to the dynamics of jets and inner accretion disks. This thesis provides a bridge between the physical structures of the inner and the outer disk, where the later is observationally easier to access. Above all, the importance of the radiative force in altering the dynamics of a magnetically launched jet is outlined in this thesis.

A thin accretion disk model with proper gas and dust opacities is applied for a luminous young high-mass star. This study has furnished estimates of various physical quantities in the inner few AU of the accretion disk. In particular, I have found that the mid-plane temperature around 0.1 AU could be as high as 10^5 K for a 10 $M_\odot$ star. Such high temperatures in the disk destroy most of the dust grains already at large radii from the central star. This in turn reduces the opacity of the accreted matter thereby overcoming the central radiation-pressure from the young massive star. In addition, such disks are stable to gravitational fragmentation inside of 100 AU from the central star. Thus they form an ideal launching base for long-lasting outflows.

Outflows and jets are an ubiquitous phenomenon in young massive star forming regions. Observational surveys have suggested that the outflows become wider as the star grows in luminosity (thus mass) with time. I have performed magneto-hydrodynamical simulations of jet launching in presence of radiative forces from the luminous star and the inner hot accretion disk. The major outcome of this work, is that the radiative force from the *central star* plays a dominating role in accelerating and de-collimating the magnetically launched jet, while the influence of the *disk radiative force* is rather small. In addition, conducting an extensive parameter study, I have found that the outflows become wider as the mass (or luminosity) of the central star increases. The degree of collimation is also affected by the magnetic field strength and optical thickness of the line. This interplay of radiative and magnetic forces provides a physical insight to the trend in degree of collimation suggested by observations.

Finally, a fully three-dimensional simulation is conducted to understand the manner in which the inner accretion disk transports material onto the central massive star. The hydrodynamic flow in the disk is simulated in the presence of radiative transfer and/or self-gravity. The transport of angular momentum is solely due to gravitational torques. My first results indicate that a locally isothermal disk becomes gravitationally instable and fragments in the inner parts as it is fed with matter from the outer massive core with a steady accretion of 10^{-3} $M_\odot\,yr^{-1}$. About 10% of the mass added onto the disk is accreted onto the central star in form of clumps. On the other hand, no fragmentation is seen in an adiabatic disk whose initial temperature profile is consistently derived from radiative transfer calculations. This investigation complements the above semi-

analytical study of the inner disk to single out the physics of angular momentum transport in massive accretion disks.

Zusammenfassung

In den innersten Regionen um junge, massereiche Sterne treten komplexe Wechselwirkungen zwischen einer Vielzahl physikalischer Prozesse auf. Da es mit Beobachtungen schwierig ist, die inneren Astronomischen Einheiten (AE) aufzulösen, ist ein theoretischer Ansatz wichtig, um sich ein qualitatives Bild dieser Regionen um junge, massereiche Sterne zu schaffen. Diese Arbeit untersucht das Zusammenspiel wichtiger physikalischer Prozesse hinsichtlich der Dynamik von Jets und der der inneren Akkretionsscheiben. Sie spannt eine Brücke zwischen den Morphologien der inneren und äußeren Scheibe, wobei letztere für Beobachtungen leichter zugänglich ist. Zudem wird die Bedeutung der Strahlungsdruck für die Änderung der Dynamik von magnetisch beschleunigten Jets behandelt.

Für die Akkretionsscheibe um den leuchtkräftigen, jungen, massereichen Stern wird das Modell einer dünnen Scheibe mit geeigneten Gas- und Staubopazitäten angewandt. Diese Studie liefert Abschätzungen für zahlreiche physikalische Größen innerhalb der inneren AE der Akkretionsscheibe. Im Besonderen habe ich herausgefunden, dass die Temperatur in der Mittelebene bei einem Radius von 0,1 AE um einen Stern der Masse 10 $M_\odot$ bis zu 10^5 K erreichen kann. Solch hohe Temperaturen in der Scheibe zerstören den größten Teil der Staubteilchen bereits innerhalb eines relativ großen Radius um den Stern. Dies wiederum reduziert die Opazität der akkretierten Materie, wodurch der zentrale Strahlungsdruck des jungen, massereichen Sterns überwunden wird. Zudem sind solche Scheiben innerhalb von 100 AE um den Stern stabil gegenüber einer gravitativer Instabilität. Somit herrschen in diesen Scheiben ideale Voraussetzungen zur Entstehung von langanhaltenden Ausflüssen.

Ausflüsse und Jets sind allgegenwärtige Phänomene in jungen, massereichen Sternentstehungsgebieten. Beobachtungsprogramme gaben Hinweise darauf, dass sich diese Ausflüsse mit der zeitlich ansteigenden Leuchtkraft (oder Masse) des Sterns aufweiten. Dazu habe ich magneto-hydro-dynamische Simulationen über den einsetzenden Jet durchgeführt, unter Berücksichtigung der Strahlungskräfte des leuchkräftigen Sterns und der inneren, heißen Akkretionsscheibe. Ein wichtiges Resultat dieser Arbeit ist dabei, dass die Strahlungsdruck *des Sterns* eine dominierende Rolle bei der Beschleunigung und Aufweitung der magnetisch hervorgerufenen Jets spielt. Der Einfluss der Strahlungskraft *der Scheibe* ist dagegen vergleichsweise gering. Zusätzlich habe ich durch eine umfassende Untersuchung der relevanten Parameter herausgefunden, dass sich die Ausflüsse mit zunehmender Masse des Sterns aufweiten. Zudem wird der Grad der Bündelung durch die magnetische Feldstärke und die optische Tiefe beeinflußt. Diese erlaubt eine physikalische Erklärung der Beobachtungsergebnisse.

Schließlich wurde eine, dreidimensionale Simulation durchgeführt, um die Art und Weise, in der die innere Akkretionsscheibe Materie auf den Stern transportiert, zu verstehen. Die hydrodynamische Gasdynamik in der Scheibe wurde dabei unter Rücksichtnahme von Strahlungstransport und/oder Eigengravitation simuliert. Der Drehimpulstransport ist dabei ausschlielich durch

die Eigengravitation bedingt. Meine ersten Ergebnisse lassen darauf schließen, dass eine lokal isotherme Scheibe gravitativ instabil wird und in den inneren Gebieten fragmentiert, wenn sie mit Materie aus den äußeren Bereichen mit einer stetigen Rate von 10^{-3} $M_{\odot}\,yr^{-1}$ versorgt wird. Etwa 10% der der Scheibe hinzugeführten Masse wird dabei in klumpiger Form auf den Stern akkretiert. hingegen lässt sich keine Fragmentation in einer adiabatischen Scheibe erkennen, deren ursprüngliches Temperaturprofil mittels Strahlungstransportberechnungen bestimmt wurde. Diese Untersuchung ergänzt die oben diskutierte semi-analytische Studie der inneren Scheibe, um die Physik des Drehimpulstransports in massereichen Akkretionsscheiben herauszuarbeiten.

Contents

List of Tables

List of Figures

What we observe is not nature itself, but
nature exposed to our method of questioning

Werner Heisenberg (1901-1976)

1 Introduction

"Nobody really understands how star formation proceeds. Its really remarkable." [a]
Star formation is indeed remarkable. About five decades ago, how star formation proceeds was a mystery to many scientists. However, now with the advent of state-of-art telescopes and computational equipments, numerous mysteries have been unraveled in the study of star formation. Even though the field of low-mass star formation is more developed there are still many fundamental questions to be answered. This is also true in case of massive star formation studies, which are still in a stage of infancy.

1.1 Massive star formation

Stars are the building blocks of a galaxy. In general, they form via collapse of molecular clouds. The standard picture of low-mass star formation initiates with the gravitational collapse of a rotating core typically having mass of the order of tens of solar masses. Angular momentum conservation ensures that such a cloud collapse leads to formation of an accretion disk typically having a size of $\sim$ 100 AU. The matter inflows via this disk on to the central star. Such an accretion event coevolve in presence of collimated jets and disk winds. Eventually when the core runs of out of in falling matter, the underlying disk also begins to disperse into a *transitional disk*. During this stage, the disk has an ideal structure to form a proto-planetary system. Finally, as the central star start burning hydrogen and reach the main sequence all the surrounding matter is cleared out leaving a system of planets orbiting around the central star. Typically all low-mass stars are believed to form in this manner. While the dominant fraction of mass of the galaxy is due to numerous low-mass stars, the brightness of the galaxy is determined by few high-mass

[a] Rogier A. Windhorst, as quoted by Corey S. Powell, A Matter of Timing, Scientific American, Vol. 267, October 1992., p. 30

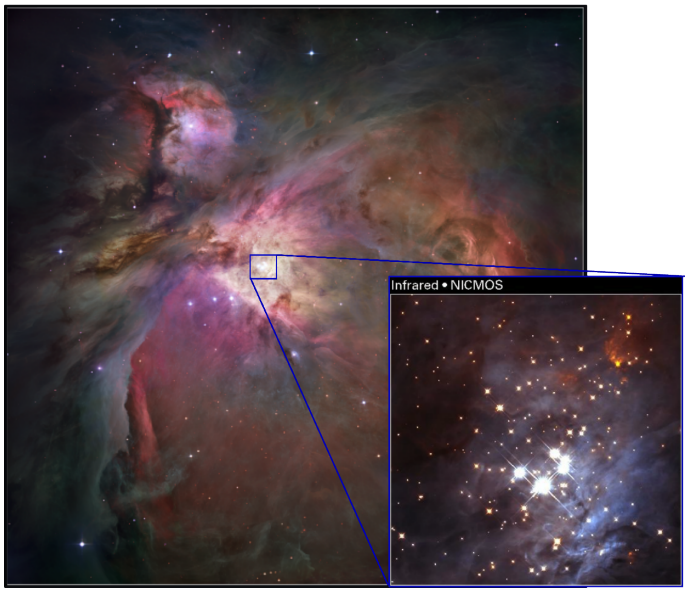

Figure 1.1: Hubble Space Telescope (HST) optical image of the Orion Nebula [M42] using the Wide Field Camera (WFC). *Inset:* Image of the Trapezium cluster obtained from near infrared camera NICMOS at HST. For the optical image credit goes to NASA, ESA, M. Robberto (STScI/ESA) and the HST Orion Treasure Project Team. For the Infrared image credit goes to NASA and K. Luhman (Harvard Smithsonian Center for Astrophysics).

stars.

Recently, studying formation of massive stars has gained importance in the field of star formation. The main reason being the complex nature of physical processes involved in formation of these stars that have $M_* > 8$ $M_\odot$. The fact that the massive stars are very rare in the universe not only makes them interesting for study but also makes it more challenging. Usually, massive stars have a large multiplicity as they form in pairs or are part of a multiple system (e.g. Trapezium cluster at the heart of Orion Nebula, see Fig. 1.1) at the centre of the cluster. In addition, all the physical processes take place rapidly as the formation time scales for massive stars are short. However, it is critical to study these stars as they are important from the point of view of feedback they provide. Young massive stars influence their surrounding via ionization, radiation pressure, powerful massive jets and outflows, and during more evolved states they provide feedback via strong stellar winds. Due to the rapid evolution, they undergo frequent supernovae, furnishing the environment with energy and momentum. Detailed reviews on massive star formation are given by Zinnecker & Yorke (2007) and Beuther et al. (2007).

1.1.1 Physical Understanding

On the basis of standard star formation theory, stars having mass greater than eight solar masses ($M_* > 8\,M_\odot$) have the *Kelvin-Helmholtz* time scale shorter than the dynamical time scale. The major implication being that these stars reach the main-sequence while they are still accreting matter from the core. In order words, massive stars do not have a well defined pre-main sequence stage. The fact that such massive stars shine light while they are gathering matter from the core made the scientists ponder over the formation mechanism. The main worry was how these stars can build up on mass in presence of strong radiation pressure from the central luminous source.

In mid 70s and late 80s, first attempts were made to understand massive star formation (Kahn 1974, Wolfire & Cassinelli 1987). The basic idea was to vary the dust grain properties and comprehend the influence of radiation pressure from the central bright source on the spherical infall of gas and dust from the massive core. These initial one-dimensional (1D) calculations pointed that the radiation pressure from the bright central star on in-falling dust grains will dominate over its gravitational pull and stars more massive then $20\,M_\odot$ can not be formed. However, this was in contradiction to the well known observational fact of stars having masses much greater than $20\,M_\odot$. In the mid 90s and early 2000, one of the first attempt was made to understand massive star formation by relaxing the fundamental assumption of spherical symmetry used for the previous calculations (Jijina & Adams 1996, Yorke & Sonnhalter 2002). In the two-dimensional axially symmetric numerical calculations (Yorke & Sonnhalter 2002), first evidence of massive star formation via accretion through massive disks was seen. The authors did take into account proper frequency-dependent radiative transfer and found out that the maximum mass the star could have is $40\,M_\odot$, which already is a factor two more than obtained from initial spherically symmetric estimates. Also with advances in computational power, it was possible to extend such calculations to even three dimensional massive core collapse simulations (Krumholz et al. 2009, Kuiper et al. 2011). These recent calculations have indeed enhanced the limit on maximum mass possible for these stars.

Massive stars form in a rather dense and crowded environment. Thus, it becomes difficult to disentangle different evolutionary stages during its formation. In a review by Beuther et al. (2007), a detailed classification of the various stages of massive stars through out its formation cycle are described. Based on this classification a single core, defined as molecular condensation associated with formation of single massive protostar or gravitationally bound multiple massive protostars, would have the following evolutionary stages -

- High-Mass Starless Cores (HMSCs)
- Low/Intermediate mass star accreting matter from the core that would eventually form a high-mass star(s).

- High-Mass Protostellar Objects (HMPOs)
- Final Massive Star.

A huge amount of physical and chemical processes evolve during the whole phase of high-mass star formation (for details see the review by Beuther et al. 2007). In this thesis, I will mostly concentrate on the last three stages of massive star formation where outflows and disk accretion play a vital role.

1.1.2 Modes of formation

The simple treatment of spherical infall of dust grains was not sufficient to form stars more massive than $20\,M_{\odot}$. In order to form stars more massive than this limit, three main scenarios were proposed and discussed in literature viz. *Competitive accretion, Coalescence* and *Monolithic collapse*. A detailed description of each of this mode of massive star formation is discussed in the review by Zinnecker & Yorke (2007).

In the view of competitive accretion, stars that are formed at the centre of the cluster enjoy the benefit of accreting larger amount of gas as compared to stars formed away from the cluster center (Bonnell et al. 1997, Bonnell et al. 2001, Bonnell et al. 2004). This is due to the fact that stars at the centre of the cluster are in a much deeper gravitational potential well. Numerical simulations of global cloud collapse supporting this idea of preferential accretion were carried out (e.g Bonnell & Bate 2006, Clark et al. 2008, Hsu et al. 2010). Based on this scenario, massive stars would form more at the centre while the low-mass stars would predominantly form in the outskirts of the cluster.

Another scenario describing massive star formation is that of coalescence (Bonnell & Davies 1998, Bally & Zinnecker 2005) which requires very high stellar density environment. In view of this formation mechanism, many low-mass stars merge to form massive stars. Although such a scenario would simply explain formation of high-mass stars in a very crowded environment, they fail to explain the observational evidences of disk formation and large scale outflows.

The mode of formation of massive stars based on accretion via rotating disks is that of monolithic collapse (Krumholz et al. 2005b). This mode is very similar to low-mass star formation, however, on a different scale. Based on this scenario, accretion rates onto massive protostars are of the order of 10^{-4} – 10^{-3} solar masses per year (McKee & Tan 2003, Banerjee & Pudritz 2007). These estimates of accretion rates are about 2-3 orders of magnitude higher than that found in the low-mass counterparts. The major advantage of this scenario is that it naturally explains the formation of molecular outflows and jets from underlying accretion disks that are ubiquitous

in massive star forming regions. Based on the idea proposed by Yorke & Sonnhalter (2002) in which preferential emission of radiation via the optically thin outflow cavity could circumvent the radiation pressure problem, Krumholz et al. (2005a) with help of semi-analytic modeling gave a quantitative proof to this idea. Further, it was also shown that even when the massive protostar has created a HCH II region, the accretion on the central star is not inhibited, rather it continues via an ionized accretion disk (Keto & Wood 2006, Keto 2007). The fact that massive stars usually form in binary or as a multiple system was shown to be true in the domain of monolithic collapse (Krumholz et al. 2009).

In principle, all these scenarios may play a role at various stages of star formation. All of these modes of star formation have exactly the same initial conditions of forming a star from collapse of an gravitationally bound gas core. The major differences in these scenarios mainly arises in the predictions of subsequent processes (e.g fragmentation) leading to formation of a stellar system. In this thesis, I follow the mode of forming massive stars in a similar manner to low-mass stars. In the following sections, I discuss advances in observations of disks and jets around young massive stars.

1.2 Accretion Disks : An Observational Perspective

Accretion disks form an integral part of star formation. In the standard picture of star formation due to collapse of the rotating core under gravity, the formation of disk like structures is inevitable. The principle of conservation of angular momentum points out the fact that any rotating gas can only be accreted on the central object via formation of a flattened disk like structure. Accretion disks not only supply the material onto the central object but also forms the launching base of jets and outflows.

With the advent of state-of-art telescopes accretion disks have been observed with high resolution and studied in details in case of young low-mass stellar objects. Detailed reviews on theoretical and observational advances in low and intermediate mass stellar disk exists in the literature (e.g. Mundy et al. 2000; Hollenbach et al. 2000; Dullemond & Monnier 2010). Low-mass stars spend about 10^7 yrs at the pre-main sequence stage before reaching the main sequence track. In contrast, massive stars do not have a well defined pre-main sequence phase and they evolve quickly towards the main sequence. Due to such rapid evolution, dense molecular cores around massive young stars do not have enough time to dissipate molecular gas before the UV radiation from the main-sequence star ionizes the immediate surroundings. This situation makes it difficult for the observers to search for disks around young and embedded massive stars. The disks around young massive stars are not only be embedded in highly opaque clouds of gas and dust but also its signatures are mixed with those of the core making the matter worse for the observers.

In addition, massive stars are usually found in a clustered environment at large distances which makes the search for disks even more challenging.

Ad-mist all these difficulties, there have been various attempts to study accretion disks around young massive stars using thermal and non-thermal emission. Most of the thermal studies of such embedded disks are related to observations in radio and sub-mm wavelength regime (see reviews by Zhang 2005 and Cesaroni et al. 2007 and references therein). At these long wavelengths, emission mainly arises from the outer part of the disk and possibly the inner part of the envelope. Thus, with such a study it is possible to observe outer parts of disks i.e. at scales of 1000 - 10,000 AU from the central object. To understand the physics of the inner disk region ($\leq$ 500 AU), it is imperative to use the help of infrared emission from the dust. One of the widely used tracer for the study of the inner accretion disk is the band head of CO overtone at 2.4 μm. Disks around T-Tauri stars can be identified by fitting line profiles of CO overtone emission with rotation (e.g. Carr 1987). With the advent of IR interferometry it has become viable to study the inner edge of the disks in greater details using the similar principles even for Herbig Ae/Be stars. Recently, this technique has even been extended to study massive accretion disks (e.g. Wheelwright et al. 2010). Another approach used to unravel the inner disk physics around young massive stars is the use of non-thermal emission in form of masers (e.g. Norris et al. 1998, Phillips et al. 1998, Torrelles et al. 1998). The most common masers used for the study of massive star forming regions are CH_3OH maser with transition at 6 GHz and H_2O maser with 22 GHz. Maser emission require special conditions to invoke population inversion, thus, they act like local tracers and do not necessarily trace the bulk of molecular gas. The linear structures in maser emission often observed around young massive stellar objects are associated with the presence of disks around these objects (Wright et al. 1995, Norris et al. 1998). However, the claims of existence of accretion disks via methanol maser measurements are highly debated due to contamination of maser signals from outflows (Pestalozzi et al. 2009).

Currently, there are many evidences of massive rotating structures observed in YSOs with luminosity $\geq 10^5$ $L_\odot$ that typically have radius of $1000 - 30,000$ AU and a mass of $60 - 500$ $M_\odot$. The observed rotational velocities are of the order of few $\mathrm{km\,s^{-1}}$. Some of the typical examples are listed in the Table 2 of the review by Cesaroni et al. (2007). Among them the best studied is a Keplerian disk around massive YSO IRAS 20126+4104 (Cesaroni et al. 2005; see Fig. 1.2). The spectral energy distribution of this IRAS point source supplies us with a luminosity of $10^4\,L_\odot$ (Cesaroni et al. 1999) for a distance of 1.7 kpc. The most part of this luminosity has been proven to be coming from the inner 1000 AU (Sridharan et al. 2005). A bipolar molecular outflow observed in many tracers, including CO and HCO^+ have been associated with this IRAS source. A hot molecular core of ~ 200 K has been detected at the geometrical center of the bipolar outflow. Imaging of this core in $CH_3CN(12-11)$ (Cesaroni et al. 1999), $NH_3(1,1)$ and $(2,2)$ (Zhang et al. 1998) and $C^{34}S(2-1)$ and $(5-4)$ (Cesaroni et al. 2005) have revealed existence of a Keplerian

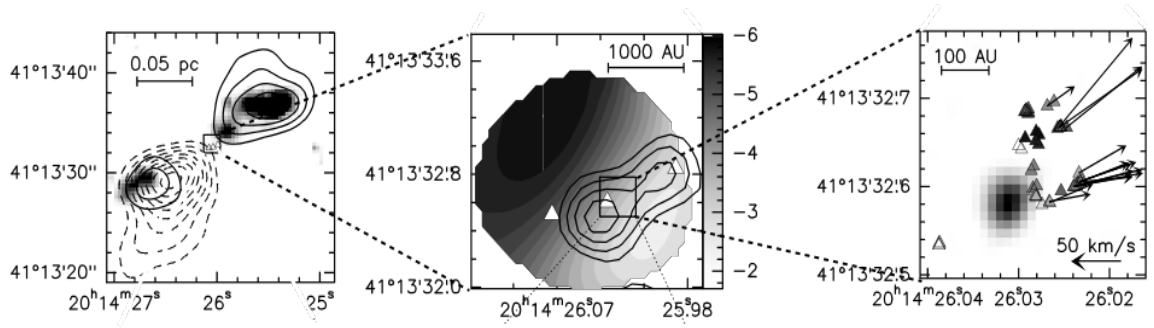

Figure 1.2: *Left*: Grey scale is the 2.2 μm H_2 line emission, over plotted are the solid and dashed contours (of the HCO^+(1-0) line) that corresponds respectively to blue and red-shifted gas. *Middle:* Velocity map as measured in the $C^{34}S$(5-4) line by Cesaroni et al. (2005), overlaid are the contours from the 3.6 continuum from (Hofner et al. 1999). *Right:* Distribution of the H_2O maser spots compared to a VLA map (grey scale image) of the 7 mm continuum emission. The arrows denote the absolute proper motions of the spots, measured by Moscadelli et al. (2005).

disk around the central star of mass $\sim 7\,M_\odot$ (Fig. 1.2) with a temperature profile that seems to be compatible with standard disk ($T \sim R^{-3/4}$). Another evidence of massive rotating structure of 10,000 AU around a possible B type star - IRAS 18151-1208 that shows similar properties of T-Tauri disks has been extensively studied (Fallscheer et al. 2011). The disk's flaring parameters obtained from this work are similar to the parameters obtained for the low mass Butterfly star (Wolf et al. 2008). In addition, massive molecular outflows have been observed in the direction perpendicular to the flattened rotating structure.

Numerical modeling of massive star formation via accretion disks indicate the presence of high accretion rates in the elongated rotating structure (Krumholz et al. 2009, Kuiper et al. 2011). Observationally, it is possible to measure the accretion rates in these massive disks in a rather indirect manner. The technique used to measure the mass inflow rate has an underlying assumption for the ratio of outflow rate to accretion rate. Molecular outflow rates can be easily measured from sub-mm CO emission. Beuther et al. (2002b) estimated the mass accretion rate of the order of $10^{-4}\,M_\odot\,yr^{-1}$. These accretion rates are about two orders of magnitude higher then that found in typical low-mass accretion disks. However, such high accretion rates are consistent with early phases of high-mass star formation.

The present status of observations suggests that like in low-mass stars accretion in case of young massive stars takes place via Keplerian disks. The various evidences of high accretion rates in these disks is consistent with rapid evolution of young massive stars. The existence of magnetic fields on large scales and presence of fast and collimated jets around young forming massive stars imply towards a scenario where massive star formation is a scaled up version of low-mass star formation.

1.3 Outflows : An Observational Perspective

Jets and outflows are common phenomena around young stellar objects. Apart from young stars, they are observed around a plethora of other astronomical objects from new born brown dwarfs to black holes at the center of the Active Galactic Nuclei (AGN). The process of ejecting gas as jets is a natural and efficient way of removing excess angular momentum from accretion disks, thereby allowing accretion to occur. While, AGNs harbor around them highly relativistic jets. The typical velocities measured for young stellar jets range from 100 - 500 $\mathrm{km\,s^{-1}}$(see review by Ray et al. 2007).

Jets ejected from these sources emit spectral lines and continuous radiation which have been detected in all bands of the electro-magnetic spectrum. In addition they also produce a rich variety of phenomena like masers, free-free emission and synchrotron radiation at radio wavelengths. Bipolar molecular outflows are also visible in sub-mm tracers such as CO, shock-excited SiO and many other molecules. Shocks generated in outflows tend to excite various near-IR and visible forbidden line emission (e.g. [FeII], [SII], [OI], [OIII])(e.g Hirth et al. 1994, Hartigan et al. 2004). Emissions in X-ray are quite common in relativistic AGN jets while in a few extreme cases, they are even observed around jets from young stellar objects. Protostellar jets generate turbulent motions and can even disrupt the parent molecular cloud. Thus, they represent a major channel in the self-regulation of star formation.

The major goal of observing jets and outflows is to understand the mechanism that controls its acceleration and collimation from the base of the accretion disk to the scales of 0.1-1 pc. Wu et al. 2004 complied a large set of outflow sources mapped in emission lines of low transitions (J = 1-0 and J = 2-1) of the CO molecule. Although, this large sample of outflow sources comes from different evolutionary stages in star formation, they represent the overall physical characteristics of outflows. Fig. 1.3 relates two important physical properties of these outflows with the bolometric luminosity L_{bol} [$L_{\odot}$]. The top panel depicts the correlation between the bolometric luminosity and the collimation factor. The collimation factor is calculated approximating the outflow to be an ellipsoid. The area and maximum angular extent (the major radius) of the outflow are then estimated, and thus the minor radius is calculated. The ratio of the major and minor radii is the collimation factor (Bally & Lada 1983) The variation of mechanical force that drives the outflow with bolometric luminosity is shown in the bottom panel. The bolometric luminosity cut-off of 10^3 $L_{\odot}$ is used to separate the low-mass outflows with the ones ejected from high-mass stars.

It is evident from Fig. 1.3, that as the luminosity of the driving source increases, the outflows ejected from them have a wider morphology. However, the correlation between them is weak. The sample under consideration is a heterogenous one obtained from a wide variety of obser-

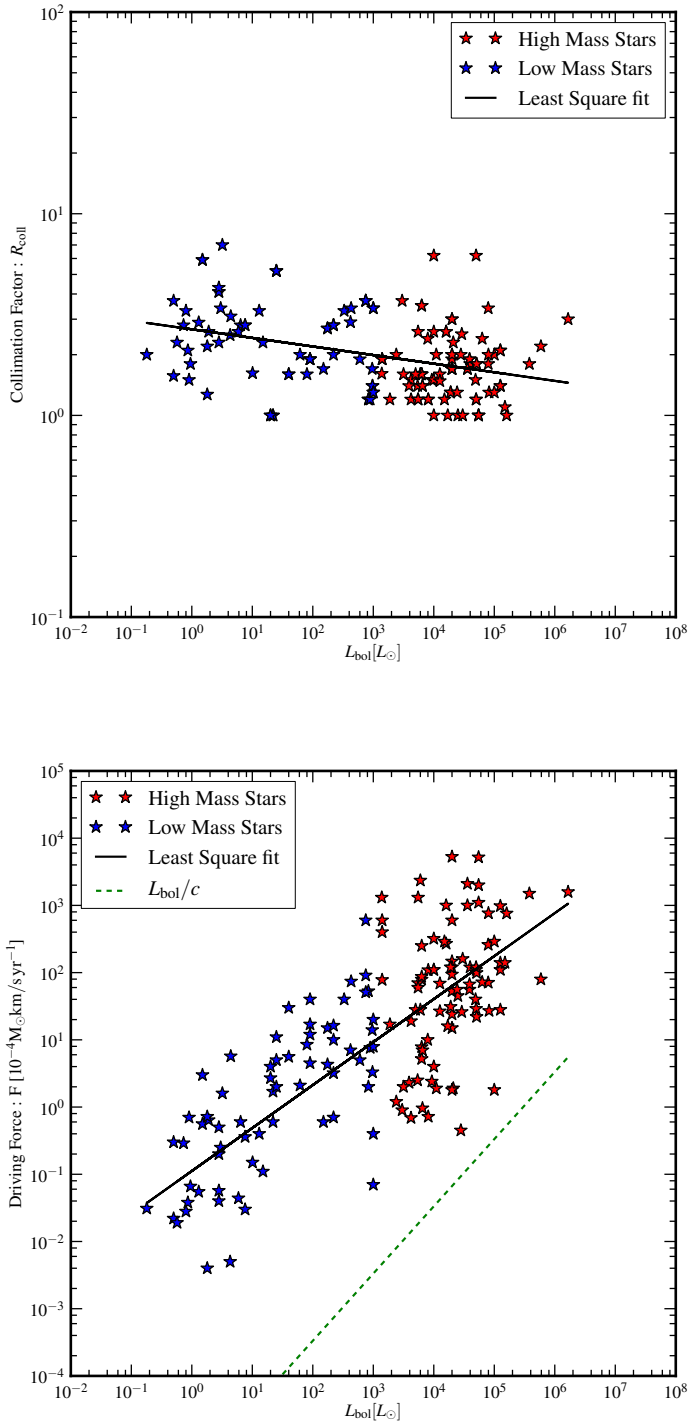

Figure 1.3: Physical properties of outflows and its relation with bolometric luminosity (Wu et al. 2004). *Top :* Collimation factor - R_{coll}, *Bottom :* Driving force F in units of $10^{-4}\,M_\odot\,km\,s^{-1}yr^{-1}$. In both panels *blue* stars mark the low-mass stars and *red* depicts the massive stars. The *green dotted* line shown in the right panel represents the driving force due to radiation alone and the *black solid* line in both panels are least square fits to the data respectively.

vations with different telescopes. In order to correlate them, it is imperative that some kind of averaging has to be done. Considering the approximations used for averaging the data along with their respective errors, Wu et al. 2004 pointed out a trend of decreasing outflow collimation with later evolutionary stages in star formation. The dependence of the mechanical driving force F, derived from the outflow parameters (Bally & Lada 1983, Goldsmith et al. 1984, Snell et al. 1984) on the bolometric luminosity is evident. The *green dashed* line represents the radiative driving force ($F \sim L_{bol}/c$, c being the speed of light) due to the central luminous source. The fact that it lies much below the linear fit for the data indicates that the radiation pressure due to single scattering of photons is not sufficient in launching outflows from young stellar objects. Thus, in order to interpret this result it was necessary to incorporate other viable mechanisms that can drive outflows from young low-mass as well as high-mass stellar sources. The mechanism that has successfully explained the process of launching jets or outflows in myriad sources was first proposed by Blandford & Payne (Blandford & Payne 1982, Pudritz et al. 2007). In the view of this framework, the launching process from low-mass protostars (and most probably also for extragalactic jets) is carried out via magnetic fields, where the disk wind is accelerated and collimated by magneto-centrifugal and magnetohydrodynamic forces (see Chapter 2 Sect. 2.2.1 for theoretical and numerical details).

Low extinction due to gas and dust around low-mass protostars provide a better environment for observing outflows with great accuracy and resolution. Most of the current understanding about the formation and propagation of jets/outflows comes from observations of low-mass stars. In this case we are fortunate to know the leading physical parameters such as outflow velocity, density, and temperature (e.g. Hartigan & Morse 2007, Ray et al. 2007). The formation of the jets around young, still forming high-mass stars takes place in the deeply embedded cold dust and gas cocoons exhibiting large visual extinction of the order 100 to 1000 mag (Arce et al. 2007). Therefore, a number of leading physical parameters concerning the inner launching base for massive outflows still remain uncertain. Large multi-wavelength studies for massive star forming regions have been done over the last decade (Beuther et al. 2002a, Stanke et al. 2002, Zhang et al. 2005, López-Sepulcre et al. 2009, López-Sepulcre et al. 2010, Torrelles et al. 2011). These studies suggest that outflows are an ubiquitous phenomenon not only for low-mass stars, but also in massive star forming regions.

While the existence of a jet magnetic field in extragalactic sources is directly confirmed by the observed radio synchrotron emission, the evidence magnetic field in jets around proto-stars is mainly indirect, namely derived from the existence of interstellar magnetic fields (e.g. Hartigan et al. 1994), or from proto-stellar flares and or field-aligned accretion columns and subsequent stellar variability (Andre et al. 1988, Bouvier et al. 2007). For many years the role of magnetic fields in massive star formation was not really known. However, recent observations made progress by clearly detecting relatively strong magnetic fields in massive star forming regions

(Vlemmings 2008). Polarimetric observations of the hot molecular core HMC G31.41 have revealed a large-scale hourglass-shaped magnetic field configuration (Girart et al. 2009). Another example is the observed 3D magnetic field structure around the massive protostar Cepheus A HW2, indicating mG-fields from maser measurements (Vlemmings et al. 2010). Furthermore, Beuther et al. (2010) detected a magnetic field aligned with the outflow via polarimetric CO emission. Very recent observations have also detected synchrotron emission in the stellar outflow HH 80-81, indicating a $\sim$ 0.2 mG magnetic field in the jet knots while the stellar mass of $\sim$ 10 $M_\odot$ is in the range of massive stars (Carrasco-González et al. 2010)

The wide observational survey of outflows around low-mass and high-mass stars suggests that launching of outflows in these stars have many common qualitative features. As far as jets from low-mass stars are concerned, there is a consensus that they are launched from a standard magneto-centrifugal process, whereas, the picture for high mass outflows is still not clear. However, the presence of magnetic fields in close by regions of massive star formation indicates the vital role they could play in launching of outflows from these stars. Quantitatively, physical parameters pertaining to low-mass stellar outflows are well defined, while most of these quantities are difficult to constraint from high-mass outflows due to the opaque environment.

1.4 Aims & Motivation

In the previous section, qualitative similarity of outflows from low-mass and high-mass stars were discussed. To understand the jets and outflows from young massive stars in more details, numerous observational surveys were carried out over the last decade. Early low-spatial-resolution single-dish studies suggested that massive outflows may have a lower collimation degree than those of their low-mass counterparts (Shepherd & Churchwell 1996). Also the most studied outflow system, Orion-KL, exhibits a more chaotic and not collimated structure (e.g., Schulz et al. 1995). However, later studies indicated that the collimation degree of jets from high-mass protostars can be as high as from low-mass regions (e.g. Beuther et al. 2002a, Beuther et al. 2002b, Gibb et al. 2003, Garay et al. 2003, Brooks et al. 2003, Beuther et al. 2004, Davis et al. 2004). Typical outflow rates in high-mass systems are estimated to be a few times 10^{-5} to $10^{-3}\,M_\odot\,yr^{-1}$, implying accretion rates on the same order of magnitude (e.g. Beuther et al. 2002b).

The originally puzzling result that different studies found different degrees of jet collimation for high-mass star-forming regions could qualitatively be resolved when it was realized that these studies in fact targeted different evolutionary stages. While jets found in the youngest star forming regions appear similarly collimated as their low-mass counterparts, jets from more evolved (massive) stars exhibit much broader outflow cones. To account for this effect Beuther & Shepherd (2005) proposed an evolutionary picture for high-mass outflows, where the jet formation

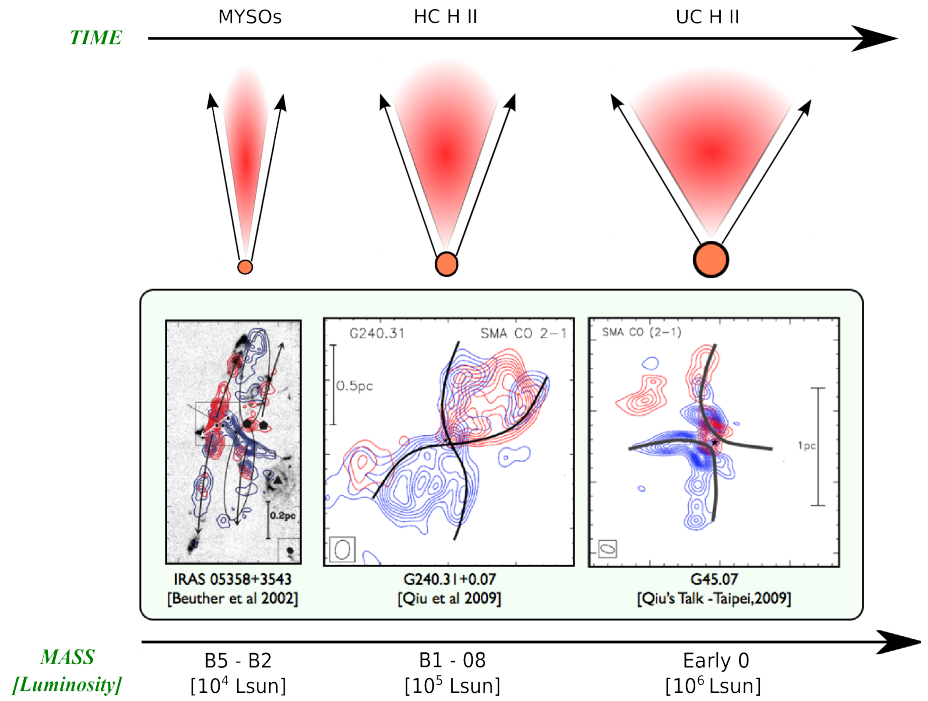

Figure 1.4: Cartoon description of the evolutionary picture of outflows in young high-mass stars (Beuther & Shepherd 2005). The CO (2-1) contours for suitable examples are also shown below.

starts with similar MHD acceleration processes compared to the low-mass models during the earliest evolutionary stages (see Fig. 1.4). However, as soon as the central sources gain significant mass, other processes come into play, for example, the radiation from the central star or more turbulence at the base of the jet. Any combination of this and other processes was expected to lower the degree of collimation. However, the evolutionary sequence proposed by Beuther & Shepherd (2005) was largely observationally motivated and could only provide a qualitative explanation.

Main Objective : The major question I would like to address in this thesis is as follows - *What kind of physics lies beneath the inner regions of young massive stellar objects that could explain the essence of the evolutionary sequence in their outflows ?*

The primary objective is to understand the dynamics of outflow launching region around young massive stars. In doing so, I derive numerical estimates of various dynamically important quantities of the inner accretion disk around massive star and study its stability. Further, I contemplate the influence of these inner disk quantities on dictating the dynamics of outflows with respect to collimation and acceleration. Additionally, I follow on to improve the previous 1D steady state model to more consistent 3D full radiative transfer models of the inner accretion disk.

1.5 Thesis Outline

In this thesis, I emphasize on studying in details the dynamical evolution of outflows and inner gaseous disk in combination to the outer dust disk up to 100 AU around young massive stars. An outline of this thesis is presented below :

- In **chapter 2**, I discuss various theoretical concepts that have been applied to the study of inner accretion disks and jets from young massive stars.

- The steady-state analysis of the launching pad of outflows around young massive stars is presented in **chapter 3**. In this chapter, I address the implication of applying standard accretion disk model with proper gas and dust opacity to a central massive star. I also tabulate typical estimates of various dynamically important quantities for the case of rapidly accreting massive disk.

- In **chapter 4**, a physical picture of outflows from young massive stars is given, so as to understand the proposed evolutionary sequence in them. In this chapter, I present results of the axi-symmetric jet launching simulations in context of ideal MHD and line driven radiative processes.

- **Chapter 5** deals with the study of detailed radiation-hydrodynamical numerical simulations of the inner accretion disk around young and luminous massive star. I present the results of 2D and 3D accretion disk simulations that incorporates self gravity of the massive disk and radiative transfer.

- In **chapter 6**, I summarize the final results from this work and further discuss various ideas that could materialize in the future.

God used beautiful mathematics in creating the world

Paul Dirac (1902-1984)

2

Theoretical and Numerical Background

This chapter describes the basic theory of various physical processes studied in this work. It begins by listing relevant equations of fluid dynamics. A synopsis of the basic model of magnetized outflows is given in Sect. 2.2. Further in Sect. 2.3, theory of accretion disk physics is reviewed along with a note on gravitational instability. In addition, theoretical aspects of radiative transfer and line driving processes are summarized. Finally, a brief note on the numerical code used for all the simulations done in this thesis is outlined.

2.1 Magnetic and Non-magnetic Fluid Dynamics

The dynamics of a fluid is governed by conservation laws. The fluid considered for this analysis is a perfect fluid. Such a fluid obeys the *ideal gas* law. This assumption is valid if the fluid has low density and high temperature. Although, we encounter a large variation in density and temperature in astrophysical gas dynamics, apart from the stellar and planetary interiors, the assumption of ideal fluid is very accurate and is always used.

2.1.1 Basic Equations

This thesis will consider perfect fluids for all purposes. The conservation laws that govern the dynamics are : the conservation of matter,

$$\frac{\partial \rho}{\partial \mathrm{t}} + \nabla \cdot (\rho \vec{u}) = 0, \tag{2.1}$$

the conservation of momentum,

$$\rho(\frac{\partial \vec{u}}{\partial t} + (\vec{u} \cdot \nabla)\vec{u}) = -\nabla P - \rho \nabla \Phi, \tag{2.2}$$

and the conservation of energy,

$$\frac{\partial}{\partial t}(\rho E) + \nabla \cdot \left[\rho E + P\right] \vec{u} = -\rho \nabla \Phi \cdot \vec{u}. \tag{2.3}$$

In the above set of conservation laws expressed as Partial Differential Equations (PDEs), Φ is the gravitational potential. The total specific energy E comprises of the internal specific energy ϵ along with the specific kinetic energy which is related to the flow velocity $\vec{u}$.

$$E = \epsilon + \frac{u^2}{2} \tag{2.4}$$

ρ is the mass density which is related to pressure P through an equation of state with an adiabatic index γ,

$$P = (\gamma - 1)\rho\epsilon. \tag{2.5}$$

The above set of equations (2.1-2.5) form a closed set that can be solved analytically (for some special cases) or numerically for the desired problem under study. These equations are frequently referred to as the set of *hydrodynamical (HD) equations*.

The other important quantity that controls the dynamics of astrophysical fluids is *magnetic fields*. Magnetic fields exist around almost all astrophysical bodies and largely play a dominant role in the dynamics of fluids around them. The equations that incorporate the magnetic field contribution on fluid dynamics are called the *magneto-hydrodynamical (MHD) equations*. They are also based on the conservational laws listed above (see equations 2.1-2.5). For our present analysis, we only consider ideal MHD limit which implies to the approximation of infinite conductivity. Ideal MHD equations are very similar to the HD equations. The conservation of matter is exactly same as equation (2.1). The difference arises in the momentum and the energy conservation laws due to the additional terms that incorporate the effect of magnetic field. These equations are listed below: the conservation of momentum,

$$\rho\left(\frac{\partial \vec{u}}{\partial t} + (\vec{u} \cdot \nabla)\vec{u}\right) = -\nabla P - \rho \nabla \Phi + \frac{1}{4\pi}(\nabla \times \vec{B}) \times \vec{B} \tag{2.6}$$

and the conservation of energy,

$$\frac{\partial}{\partial t}(\rho E) + \nabla \cdot \left[\rho E \vec{u} + (P + \frac{B^2}{8\pi})\vec{u}\right] - \vec{B}(\vec{u} \cdot \vec{B}) = -\rho \nabla \Phi \cdot \vec{u}. \tag{2.7}$$

The magnetic field in the above ideal MHD equations is denoted by $\vec{B}$. The total specific energy, E, in addition to contribution from internal specific energy and kinetic energy has a term corresponding to the specific magnetic energy,

$$E = \epsilon + \frac{u^2}{2} + \frac{B^2}{8\pi\rho}. \tag{2.8}$$

The evolution of the magnetic field is governed by the *induction equation*,

$$\frac{\partial \vec{B}}{\partial t} = \nabla \times \left(\vec{u} \times \vec{B}\right). \tag{2.9}$$

The final constraint on the set of MHD equation is the fact that no monopoles should exist and such a condition is called as solenoidal condition which is given by,

$$\nabla \cdot \vec{B} = 0. \tag{2.10}$$

The summary of the HD and MHD equations are given in a tabulated form in Table A.1. The complexity of the above set of equations dictate that their evolution can only be treated with numerical simulations. However, certain important properties of the full solutions can be inferred from a steady state analysis. This is what is addressed in the next section.

2.1.2 Steady State MHD

This section describes some important features of the MHD equations. The equations will be simplified under the assumptions of steady state ($\partial/\partial t = 0$) and axisymmetry ($\partial/\partial\phi = 0$) to obtain these features. In view of this approximation, we will derive physical quantities that remain constant along the magnetic field line. They are derived using cylindrical (R, ϕ, z) coordinates with unit vectors ($\hat{r}$, $\hat{\phi}$, $\hat{z}$) respectively.

In the steady state, the induction equation (equation 2.9) can be written as

$$\nabla \times (\vec{u} \times \vec{B}) = 0. \tag{2.11}$$

The total magnetic field, $\vec{B}$, can be expressed in terms of poloidal component (r, z plane of standard cylindrical coordinate system) $\vec{B}_{\rm p}$ and the azimuthal component B_ϕ

$$\vec{B} = \vec{B}_{\rm p} + B_\phi \hat{\phi}. \tag{2.12}$$

Similarly the velocity field, $\vec{u}$, is given by

$$\vec{u} = \vec{u}_{\rm p} + u_\phi \hat{\phi} = \vec{u}_{\rm p} + \vec{\Omega} \times \vec{R}, \tag{2.13}$$

where $\vec{\Omega} = \Omega\hat{z}$ is the angular velocity of the gas material.

Using the solenoidal condition ($\nabla \cdot \vec{B}$) and for the axisymmetric case, the poloidal magnetic field component can be expressed a gradient of a stream function a,

$$\vec{B}_{\rm p} = \frac{1}{R}\nabla a \times \hat{\phi}. \tag{2.14}$$

Such a stream function a is constant along the field line as $\vec{B}_\mathrm{p} \cdot \nabla a = 0$ (from equation 2.14). Thus a can be read as a unique label associated with a field line and is related to the magnetic vector potential A_ϕ as $a = RA_\phi$. In addition to the stream function a, any scalar '$\mathcal{S}$' that satisfies the condition - $\vec{B}_\mathrm{p} \cdot \nabla \mathcal{S} = 0$ is conserved along the field line. Using the standard steady state MHD equations, we will derive forms of some of these scalars that are conserved along the field line.

Applying the decomposed forms of the velocity and the magnetic field, equation (2.11) can be written as

$$\nabla \times [(\vec{u}_\mathrm{p} + u_\phi \hat{\phi}) \times (\vec{B}_\mathrm{p} + B_\phi \hat{\phi})] = 0. \tag{2.15}$$

The poloidal component of equation (2.15) is expressed as

$$\nabla \times [\vec{u}_\mathrm{p} \times \vec{B}_\mathrm{p}] = 0, \tag{2.16}$$

where the term, $u_\phi \times B_\phi$, vanishes due to the fact that u_ϕ is parallel to B_ϕ. Thus from equation (2.16) and axisymmetric conditions, one can conclude that $\vec{u}_\mathrm{p}$ is parallel to $\vec{B}_\mathrm{p}$. Thus,

$$\vec{u}_\mathrm{p} = \mathcal{K}(R, z)\vec{B}_\mathrm{p}, \tag{2.17}$$

where $\mathcal{K}$ is a scalar function, constant for the surface of constant magnetic flux.

While, the toroidal component of equation (2.15) is expressed as

$$\nabla \times [(\vec{u}_\mathrm{p} \times B_\phi \hat{\phi}) + (u_\phi \hat{\phi} \times \vec{B}_\mathrm{p})] = 0. \tag{2.18}$$

Substituting the expression for poloidal velocity from equation (2.17) and toroidal component of velocity in terms of angular velocity $\vec{\Omega}$ in equation (2.18) and using axisymmetric conditions we get,

$$\vec{B} \cdot \nabla \left(\Omega - \frac{\mathcal{K} B_\phi}{R} \right) = 0. \tag{2.19}$$

Thus, along a particular field line we have

$$\Omega - \frac{\mathcal{K} B_\phi}{R} = \text{const.} \tag{2.20}$$

Further for the steady state axisymmetric setup, the continuity equation (see Table A.1) and the solenoidal condition ($\nabla \cdot \vec{B} = \nabla \cdot \vec{B}_\mathrm{p} = 0$) can be combined as,

$$\nabla \cdot (\rho \vec{u}) = \nabla \cdot (\rho \mathcal{K} \vec{B}_\mathrm{p}) \Rightarrow \rho \mathcal{K} = \zeta(a) = \text{const.} \tag{2.21}$$

$\zeta(a)$ is a constant along a field line and is associated with the mass flux density on that particular field line. Substituting expression for $\zeta(a)$ in equation (2.20) we obtain the Ferraro's iso-rotation law (Ferraro 1937),

$$\frac{1}{R}\left(R\Omega - \frac{\zeta}{\rho}B_\phi\right) = \Omega_{\rm F}(a) = \text{const}, \tag{2.22}$$

where $\Omega_{\rm F}(a)$ is the angular velocity of the field line and it remains constant.

Thus, we have the mass flux density $\zeta(a)$ and the angular velocity of the field line $\Omega_{\rm F}(a)$ constant along the field line. The two other quantities that are conserved along the field line are the total angular momentum and the specific energy. In order to derive the conservation laws for the remaining two quantities, we begin with steady state MHD momentum conservation equation (equation 2.8),

$$\frac{1}{4\pi\rho}(\nabla\times\vec{B})\times\vec{B} - (\nabla\times\vec{u})\times\vec{u} = \nabla\left[\frac{P}{\rho} + \frac{1}{2}|\vec{u}|^2 + \Phi\right]. \tag{2.23}$$

In an axisymmetric case, the toroidal component of the above equation can be expressed as,

$$\left[\frac{1}{4\pi\rho}(\nabla\times\vec{B})\times\vec{B}\right]_\phi = \frac{1}{R}\vec{u}\cdot\nabla(\Omega R^2), \tag{2.24}$$

which can be further simplified to

$$\vec{B}_{\rm p}\cdot\nabla\left(\frac{RB_\phi}{4\pi} - \rho\mathcal{K}\Omega R^2\right) = 0. \tag{2.25}$$

Thus, from the definition of the conserved quantity along a field line we have the expression for the conserved specific angular momentum,

$$l(a) = Ru_\phi - \frac{RB_\phi}{4\pi\zeta}. \tag{2.26}$$

Similarly one can derive the conserved form of specific energy from the poloidal component of equation (2.24),

$$e(a) = \frac{1}{2}u^2 + \frac{P}{\rho} + \Phi - \frac{\Omega_{\rm F}RB_\phi}{4\pi\zeta}. \tag{2.27}$$

In summary we have four conserved quantities along the field line for a steady state axisymmetric MHD jet - (i) the mass flux density - $\zeta(a)$, (ii) the field line angular velocity - $\Omega_{\rm F}(a)$, (iii) the specific angular momentum - $l(a)$ and (iv) the specific total energy - $e(a)$. These quantities are used while setting up consistent launching boundary conditions for the numerical setup on outflows from young massive stars (see Chapter 4).

2.2 Physics of magnetized outflows

Magnetized winds and jets can be produced by rotating objects which have magnetic fields anchored to them. Such a magnetic field was also speculated to be a reason of spindown in stars (Schatzman 1962). Weber & Davis (1967) developed quantitative models for magnetized stellar winds. The main aim of this work was to explain spin down in stars. Later, Michel (1969, 1973) applied the idea of magnetized outflows to the study of relativistic pulsar winds. The notion that the strong outflows are magnetically driven from the accretion disks was proposed by Bisnovatyi-Kogan & Ruzmaikin (1976), Blandford (1976) and Lovelace (1976). Further, Blandford & Payne (1982) devised a self- similar model (Here after BP model) to quantify the physical properties of magnetically driven outflows. While, full numerical solutions for the steady (non-relativistic) problem were obtained by Sakurai (1987).

An initial attempt to model the equatorial magnetized stellar winds was made by Weber & Davis (1967) following along the lines similar to Parker (1958) for the solar wind. The main difference was to include the effects of large scale magnetic field and azimuthal rotation of the star. Weber & Davis (1967) found that the topology of the magnetized solution was similar to the earlier non-magnetized counter part but now it has to pass through three critical points as compared to just one (sonic point in case of Parker's model, see Sect. 2.2.2). In addition, they also found that the gas convects away a substantial amount of angular momentum and the torques produced by magnetic fields play a vital role in spin down of stars.

The interplay between rotation and magnetic fields was further applied to study acceleration and collimation of jets from accretion disks around black holes (Blandford & Payne 1982, Sakurai 1987). The process of launching jets from disks was studied in a self similar manner for an axisymmetric setup by Blandford & Payne 1982 assuming the magnetic field at the disk surface to be $B(r, z = 0) \propto r^{-5/4}$. Self similarity implies expressing all dynamical quantities as a function of a single independent quantity. For the BP model, the spherical radius along a given direction was used as an independent scale. The approximation of self similarity was further relaxed in the model by Sakurai (1987). In this model, steady state axisymmetric MHD equations were solved numerically to confirm the general results obtained from the self similar approach.

The following section gives some basic heuristic arguments explaining the physics of launching, accelerating and collimating MHD outflows in view of the BP model (also see Spruit 1996, 2010).

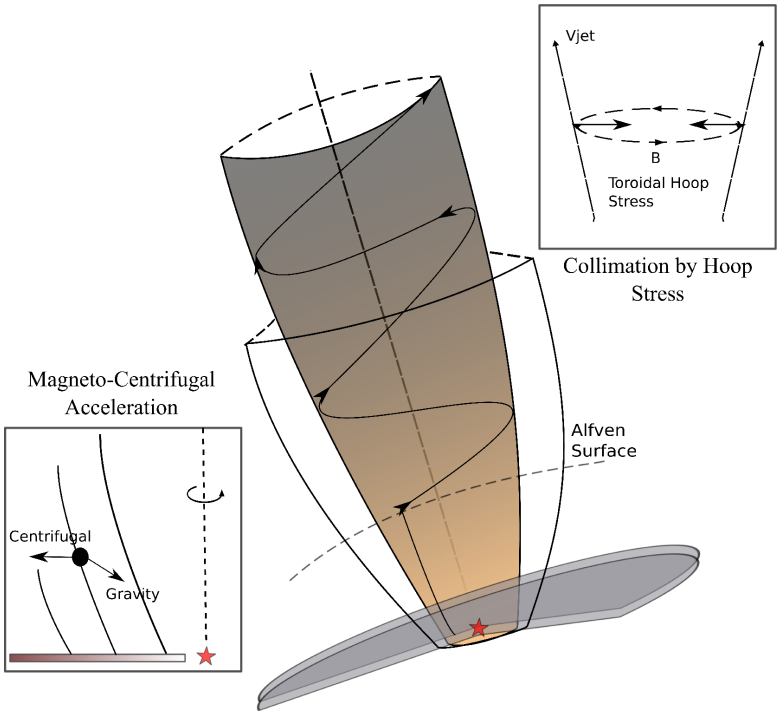

Figure 2.1: Cartoon picture representing the Blandford and Payne model of MHD launching and collimation of jets. *Left inset :* Illustration of a gas particle attached to the magnetic field line as a 'bead on a wire'. *Right inset :* Collimation of magnetic jets due to hoop stress.

2.2.1 Blandford Payne model : Heuristics

The seminal BP model presented self similar solutions for axisymmetric MHD jet flow. This primary picture of MHD jet flow prescribes that the field lines inclined at certain angle ($> 30°$) from the normal to the disk are efficient to launch the matter via centrifugal acceleration and further collimate the flow via generation of toroidal fields.

The magneto-centrifugal acceleration process is illustrated in the left inset of Fig. 2.1. Assume that the underlying disk from which the outflow is launched is cool, implying that the rotation is close to Keplerian and its thickness can be neglected. Also, assume that the gas above the disk is sufficiently ionized so as to apply the ideal MHD limit i.e. the gas is tied to magnetic field lines. Very close to the disk surface the atmosphere of the disk is forced to rotate with the field lines sticking out of the disk. At the fixed foot point of the field line ($r = r_0$), the inward gravity is balanced by centrifugal force (Keplerian rotation). However, as one moves along the field line, centrifugal force increases with distance from the axis and thus at some point it exceeds the inward gravity pull. In such a case, the gaseous material is accelerated along the field lines similar to *beads* moving on a *rigid wire*.

To understand this picture quantitatively, consider the beads start from rest at the disk and are carried with constant angular velocity on the rigid wire. In such a case the bead will experience an effective potential due to the inwards gravity pull and outward centrifugal push. Such a potential is given by,

$$\phi_{\rm BP} = -\frac{GM}{r_0}\left(\frac{1}{2}\left(\frac{r}{r_0}\right)^2 + \frac{r_0}{\sqrt{r^2+z^2}}\right). \tag{2.28}$$

Here r, z are cylindrical co-ordinates, r_0 is the foot point of the field line attached to the disk around the central object of mass M and G is the gravitational constant. To simplify the above equation, let us choose $x = r/r_0$ and $y = z/r_0$. We now plot the equipotential surfaces as a factor of $-(GM/r_0)$ in x-y plane. Such a contour plot is shown in Fig. 2.2. The *solid* black line separates the regions from which winds can be launched. The *dashed* vertical line at $r = \sqrt{3}r_0$ is an asymptote for the surface of marginal stability. In terms of angles, if the poloidal field line makes an angle of less than 60° to the equatorial plane, then the gas near the disk surface is unstable and will flow outwards. Whereas for more vertical field lines, the system is more stable. In such a case no flow is expected. The condition for launching can be further modified due to thermal effects. The critical angle is modified from 60° to 70° on inclusion of the thermal pressure (Pelletier & Pudritz 1992).

At large distances above the disk (i.e. at the Alfvén surface), the centrifugal acceleration stops. At this point the field is not strong enough to enforce co-rotation. Beyond this the inertia of the gas causes it to lag behing the rotation of field lines, thereby winding up the field lines (see Fig. 2.1). The wound field lines generates an azimuthal component of magnetic field which decreases in magnitude with increasing height in the jet (as seen from non-rotating frame). The *pinch force* due to azimuthal fields is directed inwards which causes the flow to be deflected towards the axis (see right inset of Fig. 2.1).

Another important feature of this model apart from producing outflows is that of efficient extraction of angular momentum from the accretion disk. Such a removal of angular momentum would aid viscous disks in the process of accreting matter. Based on conservation of angular momentum, it can be shown that the ratio of the mass outflow rate to the mass inflow rate is related to the Alfvén radius ($r_{\rm A}$) and the foot point radius (r_0) -

$$\frac{\dot{M}_{\rm out}}{\dot{M}_{\rm acc}} = \frac{1}{2}\left(\frac{r_0}{r_{\rm A}}\right)^2. \tag{2.29}$$

In summary, magnetically driven wind can be conveniently broken down into three conceptual stages. Close to the disk surface, the wind is launched and the amount of mass ejected into the flow depends on the details of the disk structure and the magnetic field configuration near this surface. A bit further away from the disk, the flow is accelerated almost entirely by gravitational

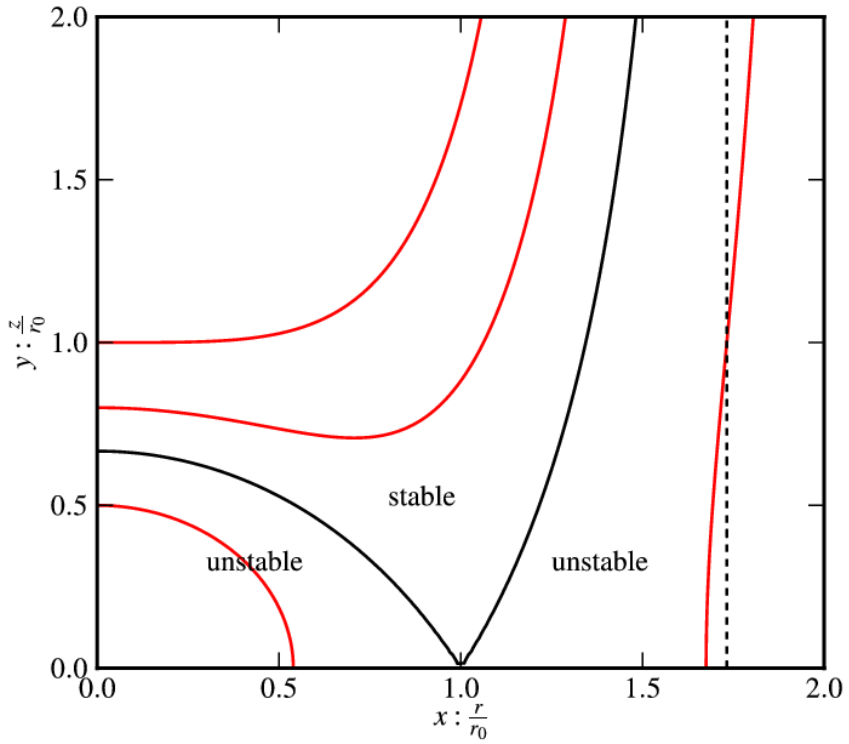

Figure 2.2: Contours (*red*) of effective potential on a bead moving on a rigid wire. The two main forces that act are the central gravity pull and the outward centrifugal force. The *black* line passes through (r_0,0) and corresponds to $\phi_{\rm BP} = -3GM/2r_0$. The angle between this iso-potential line and r-axis is 60°. The effective potential decreases with reaching the central star or radially outward. The unstable region left of $r = r_0$ marks the infall while the region to the right represents the outflow. The *black dashed* line at $r = \sqrt{3}r_0$ is the surface of marginal stability and reaches infinity in z-direction.

and magnetic/centrifugal forces. As the acceleration phase ends roughly at Alfvén surface, the collimation phase starts, in which the flow is deflected towards the axis by the hoop stress.

This physical picture of magnetized outflows has also been studied in a numerical framework. A large number of numerical simulations of jet formation have been performed which all confirm this picture of self-collimated MHD jets for low mass stars (Ouyed & Pudritz 1997, Krasnopolsky et al. 1999, Fendt & Čemeljić 2002, Ouyed et al. 2003, Fendt 2006, Fendt 2009). Its applicability has also been demonstrated for the case of extragalactic jets (e.g. Komissarov et al. 2007, Porth & Fendt 2010).

2.2.2 Critical points and Lorentz force

Astrophysical relevant solutions for magnetized winds start at a very high density near the disk surface and decrease to vanishing density at infinity. A smooth and valid solution should have no discontinuity in the Bernoulli function (equation 2.27) over the entire density range. In order to achieve such a continuos variation of *e(a)*, the wind has to pass through various critical points. In this section, the critical points related to axisymmetric MHD flow are discussed.

One of the most important critical point in a MHD flow is the Alfvén point (see Sect. 2.2.1). The condition for the Alfvén surface can be derived by combining the conservation laws for the angular velocity ($\Omega_{\rm F}(a)$) and the total specific angular momentum (*l(a)*). Substituting the expression for B_ϕ in equation (2.26) from equation (2.20), we obtain

$$u_\phi - \Omega R = \frac{l - \Omega R^2}{R[1 - 1/(4\pi\mathcal{K}^2\rho)]}. \tag{2.30}$$

The denominator on the RHS vanishes when $4\pi\rho u_{\rm p}^2/B_{\rm p}^2 = 1$, or $u_{\rm p} = U_{\rm Ap}$, where $U_{\rm Ap} = B_{\rm p}/\sqrt{4\pi\rho}$ is the poloidal Alfvén speed. The location along the field line where the above condition is satisfied is called the *Alfvén point*.

Along with the Alfvén point, the MHD winds have two more critical points corresponding to the slow magneto-sonic and the fast magneto-sonic surface. The conditions to derive them is simply given by

$$\begin{aligned} \partial e(R,\rho)/\partial R &= 0 \\ \partial e(R,\rho)/\partial \rho &= 0 \end{aligned} \tag{2.31}$$

Using the equations of steady state MHD theory and definition of Alfvén point, the set of equa-

tions (2.31) can be expressed as

$$\rho\frac{\partial e}{\partial \rho} = -\frac{(u_{\rm p}^2 - u_{\rm sp}^2)(u_{\rm p}^2 - u_{\rm fp}^2)}{(u_{\rm p}^2 - u_{\rm Ap}^2)}, \tag{2.32}$$

where the slow mode critical point $u_{\rm sp}$ and the fast mode critical point $u_{\rm fp}$ are the solutions of the equation given by

$$U^4 - U^2(c_{\rm s}^2 + U_{\rm A}^2) + c_{\rm s}^2 U_{\rm A}^2 (B_{\rm p}/B)^2 = 0, \tag{2.33}$$

here U is the wave speed, $c_{\rm s}$ the sound speed and $U_{\rm A}$ is the total Alfvén speed defined by $B^2/\sqrt{4\pi\rho}$.

Thus, a feasible MHD wind solution should satisfy the conditions at these three critical points. These points mark special positions on the field line. We have applied this fact in Chapter 4, to quantify the collimation degree in the flow.

The physical force that is responsible for the dynamics (acceleration and collimation) of the MHD wind is the Lorentz force. The Lorentz force, $\vec{F}_{\rm L} = \frac{1}{4\pi}(\nabla \times \vec{B}) \times \vec{B}$, acts in a direction perpendicular to that of the current density $\vec{J} = \frac{1}{4\pi}(\nabla \times \vec{B})$ and the total magnetic field $\vec{B}$. The form of total current density $\vec{J}$ can be expressed using the Ampere's Law, and in axisymmetric case it is expressed as follows.

$$\vec{J} = \frac{\nabla I \times \hat{\phi}}{2\pi R} \tag{2.34}$$

where $I(R, z) = 2\pi R B_\phi$ is the total current linked by a circle of radius R and with center at z. The Lorentz force, $\vec{F}_{\rm L}$, can be resolved into three components. The Lorentz force parallel to the magnetic flux ($\vec{F}_{\rm L,\parallel}$) surface is responsible for acceleration of the flow, whereas the collimation of outflow is determined by the component perpendicular to the flux surface ($\vec{F}_{\rm L,\perp}$). The azimuthal component of the force $\vec{F}_{\rm L,\phi}$ influences the angular velocity of the matter and thus affects the centrifugal balance in the flow. The magnitude of these various components of the MHD Lorentz force are given below (Ferreira 2002)

$$F_\phi = \frac{B_{\rm p}}{2\pi R}\nabla_\parallel I \tag{2.35}$$

$$F_\parallel = -\frac{B_\phi}{2\pi R}\nabla_\parallel I \tag{2.36}$$

$$F_\perp = B_{\rm p} J_\phi - \frac{B_\phi}{2\pi R}\nabla_\perp I \tag{2.37}$$

where, $\nabla_\parallel = \vec{B}_{\rm p} \cdot \nabla / B_{\rm p}$, $\nabla_\perp = (\nabla a \cdot \nabla)/|\nabla a|$ and J_ϕ is the azimuthal component of current density $\vec{J}$.

2.3 Accretion disk physics

Accretion disks plays a central role in the process of star formation. They are not only responsible to accrete matter on the central star but also form the launching base of large scale jets and outflows. A large number of macroscopic and microscopic processes affect the disk structure. In this section, I will discuss a standard thin disk steady state model which has been widely used to study accretion disks around numerous astrophysical objects (e.g. black holes, Cataclysmic Variables (CVs), low mass stars). Furthermore, I will describe gravitational instability in the disk which is one of the fundamental mechanism for transporting angular momentum. This section is developed in line with the following literature - Frank et al. 1992, Hartmann 1998 and Dullemond & Monnier 2010.

2.3.1 Steady state thin disk model

The steady state thin disk equations are presented in Frank et al. (1992). The vertically averaged surface density Σ is related to the mass density ρ and the scale height H.

$$\Sigma = 2H\rho \tag{2.38}$$

The scale height is estimated using the approximation for a thin disk

$$H = \sqrt{2}\left(\frac{c_s}{\Omega}\right) \tag{2.39}$$

where Ω is the Keplerian angular velocity and c_s, the sound speed is defined in terms of temperature,T. and other physical constants like Boltzmann constant k_B, proton mass m_p and the mean molecular weight μ.

$${c_s}^2 = \left(\frac{k_B}{\mu m_p}\right)T \tag{2.40}$$

The energy balance equation states that the amount of energy radiated from the disk is equal to the amount of energy produced by viscous heating.

$$\left(\frac{16\sigma}{3\Sigma\kappa}\right)T^4 = \left(\frac{9}{4}\right)\vartheta\Sigma\Omega^2 \tag{2.41}$$

The viscosity ϑ is defined by introducing the parameter α_v Shakura & Sunyaev (1973),

$$\vartheta = \alpha_v c_s H. \tag{2.42}$$

The Rosseland mean opacity κ (see equation (2.51) in Sect. 2.4.1), which derived in the diffusion approximation to the radiative transport equation, is related to the mass density and the temperature in form of power law with κ_0 as constant and m, n as power indices

$$\kappa = \kappa_0 \rho^m T^n \tag{2.43}$$

The condition for the conservation of angular momentum in steady state can also be derived.

$$\Sigma\vartheta = \frac{\dot{M}}{3\pi}\left[1 - \left(\frac{R_*}{r}\right)^{\frac{1}{2}}\right] \tag{2.44}$$

The dimensionless viscosity factor $\alpha_{\rm v}$ is introduced to parameterize viscosity by assuming that it is a result of turbulent motions present in the disk. The physical significance of equation (2.42) is that the largest size of turbulent eddy that can be sustained in the disk is of size equal to the disk scale height and maximum speed of the turbulent motion is that of sound speed, this implies values of $\alpha_{\rm v} \lesssim 1$. The above equations can be solved consistently using the formulation for the opacity.

The original standard disk model by Shakura & Syunyaev (1973) relates to solving above equations for the thin disk assuming certain opacity laws for different regions in the disk. The disk is classified to have three regions (A,B, and C) depending upon the opacity and the pressure.

- Region C is the outermost region where the gas pressure is much greater than the radiation pressure in the disk and free-free opacity dominates in this region.
- In Region B, the gas pressure is greater but the Thomson scattering is dominates over Kramer's opacity.
- Region A is closest to the central object and the radiation pressure in the disk is much greater than the gas pressure.

For an opacity in the form of a power law given by equation (2.43), one gets power law solutions of all the dynamical quantities in the disk. For instance, in case of the Kramer opacity law ($\kappa = 6.6 \times 10^{-22}\rho T^{-\frac{7}{2}}$) used by Shakura & Syunyaev (1973), the central temperature in the disk around a typical massive star in the region where $P_{\rm gas} > P_{\rm rad}$ and $\sigma_{\rm ff} > \sigma_{\rm t}$ (region C) is

$$T_{\rm c}(r) = 1.74 \times 10^4\ {\rm K}\ (\alpha_{\rm v})^{-1/5}\left(\frac{\dot{M}}{10^{-4}\ {\rm M_\odot\ yr^{-1}}}\right)^{3/10}\left(\frac{M}{10\ {\rm M_\odot}}\right)^{1/4}\left(\frac{r}{r_{star}}\right)^{-3/4}\left(\frac{r_{star}}{6\ {\rm R_\odot}}\right)^{-3/4} \tag{2.45}$$

where $\sigma_{\rm ff}$ is the free free opacity and $\sigma_{\rm t}$ is the opacity due to electron scattering.

The above derived equations will be referred to in context of accretion disks around young massive stars in Chapter 3. The accretion disks transport material on the central star via transport of angular momentum. Various mechanisms are discussed in the literature that aid in angular momentum transport (e.g. magneto-rotational instability, gravitational instability, jets and outflows). In the next section, I will describe in detail the instability in disks due to gravitational torques.

2.3.2 Gravitational instability

The prevailing paradigm of star formation is via accretion disks. One of the efficient mechanism for transport of angular momentum is through gravitational instability (GI). GI's can occur in any region of the disk that becomes sufficiently cold or have a high surface density. This mechanism also explains the formation of gas giant planet close to the central star. Large number of papers that give emphasis on planet formation via such disk instability are present in the literature (e.g. Boss 1998, Boss 2000, Durisen et al. 2007). The effects of gravitational instability on massive accretion disks are also discussed in literature (e.g. Lodato & Rice 2005).

The physical aspect of GI's were first put forward by Toomre (1964). He found that the parameter, Q, that determines the occurrence of GI's in thin gas disk is given by

$$Q = \frac{c_s \Omega_{epi}}{\pi G \Sigma}. \tag{2.46}$$

Here, c_s is the thermal sound speed and Σ is the disk surface density. The epicyclic frequency Ω_{epi} can be approximated as the angular velocity of a pure Keplerian disk. In case of axi-symmetric (ring-like) disturbances, disks are stable for $Q > 1$ (Toomre 1964). In the linear regime at high Q-values, pressure represented by c_s in equation (2.46) stabilizes short wavelengths, while long wavelengths are stabilized by rotation (Ω_{epi} in equation 2.46). The most unstable wavelength for $Q < 1$ is given by

$$\lambda_m = \frac{2\pi^2 G \Sigma}{\Omega_{epi}^2}. \tag{2.47}$$

In order to study GI's in non-linear regime, large number of simulations have been carried out with various grid and particle based codes (e.g. Pickett et al. 2000, Nelson et al. 2000). These simulations indicate that as GI's emerge from linear regime, they may either saturate at nonlinear amplitude or fragment the disk. The fate of disk is controlled mainly by - disk thermodynamics and non-linear mode coupling.

GI's leads to formation of spiral arms in the disk. These arms are source of spiral density waves that produce strong localized heating in the disk due to shocks. Gas in the disk is also heated by compression and through net mass transport due to gravitational torques. Balance between heating and cooling processes in the disk plays a crucial role in determining the fate of the final disk configuration. In case of slow to moderate cooling, thermal regulation of GI's is achieved. In such a case, Q hovers near the instability limit and the nonlinear amplitude is governed by the cooling rate. Based on a study of large number of simulations with varied disk cooling times, Gammie (2001) derived a criteria for the disk to fragment in presence of GI, given by

$$t_{cool} \leq 3\Omega^{-1}, \tag{2.48}$$

where Ω is the angular velocity of the rotating disk.

2.4 Radiative processes

Radiative processes play a central role in a myriad astrophysical systems. In most of them, radiation is treated as a particle phenomenon. In this picture, light is made up of *quanta* (photons) with energy proportional to the frequency ν. Interaction of these photons with matter results in their creation or destruction. Radiation can affect the surrounding matter either by an exchange of momentum and/or by an exchange of heat. Radiative processes play a vital role in study of star formation. They become even more important in case of young massive stars. These stars begin to radiate while they are accreting mass from the disk/core. Thus, photons emitted during the formation process could have a possible role in governing the dynamics of the surrounding material.

During this thesis, I have studied two different physical systems that include effects due to radiative processes. One of them deals with transfer of momentum from the photon to the matter in magnetically driven jets (Chapter 4). The other deals with flux limited radiative transfer in the surrounding self-gravitating accretion disk (Chapter 5).

2.4.1 Mean opacities

Opacities are fundamental quantities in theory of radiative transfer. It represents the ability of the material to absorb radiation. Detailed analysis of the opacity requires the understanding of various microscopic processes (e.g. bound-bound, bound-free, free-free, electron scattering) that can absorb (or emit) photons at each frequency ν. Macroscopically, opacity is a quantity that takes into account the combined effect of these microscopic processes.

Quantitatively, opacity is related to the mean free path of photon with energy hν :

$$\Lambda = \frac{1}{\kappa_\nu \rho}. \tag{2.49}$$

Here, the subscript ν denotes the implicit dependence of opacity on frequency and ρ is the matter density. The dependence of opacity on the frequency is complicated for many real physical systems. Thus, solving realistic radiative transfer equations in which opacity enters nonlinearly becomes difficult. The approach usually preferred for solving such problems is the *grey approximation*. In this approximation, a frequency weighted mean opacity is defined that could represent correctly the total transport of radiation.

I will discuss three of such mean opacities that are widely used in this work. They are (i) the flux weighted mean, (ii) the Rosseland mean and (ii) the Planck mean. These means are defined while transforming the radiation moments equations (see equations (2.54-2.56) in Sect. 2.4.2) from the

non-grey to the grey formalism. Quantitatively, they differ from each other in the process of averaging.

The flux weighted mean has the simplest form of all and is defined as weighted average with the flux as weights. The formulae is given by,

$$< \kappa_\nu >_{\mathcal{F}} = \frac{\int_0^\infty \kappa_\nu \mathcal{F}_\nu d\nu}{\int_0^\infty \mathcal{F}_\nu d\nu}, \tag{2.50}$$

where, $\mathcal{F} = \int_0^\infty \mathcal{F}_\nu d\nu$, is the flux integrated over the complete frequency spectrum.

The Rosseland mean opacity which is widely used in the optically thick stellar interiors is defined as follows :

$$\frac{1}{< \kappa_\nu >_{\rm R}} = \frac{\int_0^\infty [1/\kappa_\nu] dB_\nu(T)/dT d\nu}{\int_0^\infty [dB_\nu(T)/dT] d\nu}. \tag{2.51}$$

Here $B_\nu(T)$ is the standard Planck function. The assumptions valid for stellar interiors (isotropic radiation field and thermodynamic equilibrium) are applied to derive the above equation.

The Planck mean opacity on the other hand is applicable to stellar atmospheres (optical depth $\tau_\nu << 1$) and quantitatively it has the same form as equation (2.50), but using the Planck function as weights. Thus, the Planck mean opacity is defined as

$$< \kappa_\nu >_{\rm P} = \frac{\int_0^\infty \kappa_\nu B_\nu(T) d\nu}{\int_0^\infty B_\nu(T) d\nu}. \tag{2.52}$$

The major advantage of defining mean opacities is that they can be expressed as functions of matter quantities like the density (ρ) and the temperature. Such a simplification can be used as an advantage to solve the equations of radiation hydrodynamics. The various mean opacities have their regions of validity and utility, but none can fulfill the promise of reducing the non-grey problem to that of a grey problem. However, they greatly reduce the complexity of the problem of radiative transport and thus are of critical importance for all practical purposes.

2.4.2 Radiative transfer

This thesis deals with radiative transfer along with hydrodynamics in the process of understanding dynamical evolution of the inner accretion disk. The radiative transfer equations are solved numerically along with standard set of hydrodynamical equations for this exercise. Details of implementing these equations in numerics are given in Chapter 5. Here, I will mainly draw on the

descriptions of basic radiative transfer theory by Chandrasekhar (1960), Shu (1991) and Castor (2004).

The important quantity to define *a priori* in the study of radiative transfer is the specific intensity I_ν. It is the energy flux per unit time, unit frequency, unit solid angle and unit area normal to the direction of propagation -

$$I_\nu = \frac{dE_\nu}{\cos\theta \mathrm{d}\nu \mathrm{d}\omega \mathrm{dAdt}}. \tag{2.53}$$

The radiation field will generally interact with the medium through which it travels. The medium can absorb, scatter and emit photons, with all three processes modifying I_ν as a function of space, time and incident radiation. Therefore, in general I_ν is a function of seven independent variables (three in space for position, two angle coordinates for direction, and as a function of time and frequency).

Although the radiation field is defined completely by I_ν, it is more intuitive to define moments considering the multivariate nature of the specific intensity. The zeroth moment of the intensity is the energy density of radiation defined as

$$E_\nu = \frac{1}{c}\int_0^{4\pi} I_\nu d\omega. \tag{2.54}$$

The vector flux $\vec{\mathcal{F}_\nu}$ is the first moment and is defined along the unit vector $\hat{n}$ as follows

$$\vec{\mathcal{F}_\nu} = \int_0^{4\pi} \hat{n} I_\nu d\omega. \tag{2.55}$$

The final moment is the radiation pressure tensor prescribed as

$$\mathcal{P}_\nu = \frac{1}{c}\int_0^{4\pi} \hat{n}\hat{n} I_\nu d\omega. \tag{2.56}$$

In order to derive the radiative transport equation, I begin with the definition of the continuity equation of I_ν (Castor 2004) in a perfect vacuum. In this case of zero optical depth ($\tau = 0$), the radiative transfer guarantees that the beam intensity I_ν will remain constant as it moves along the (unit) direction vector $\hat{n}$, in some interval Δt

$$I_\nu(\vec{r} + (c\Delta t)\hat{n}, t + \Delta t) = I_\nu(\vec{r}, t). \tag{2.57}$$

Here $\vec{r}$ is the position vector and c is the speed of light. Taylor expansion about ($\vec{r}$, t) and neglecting higher order terms results in

$$\frac{1}{c}\frac{\partial I_\nu}{\partial t} + \hat{n}\cdot\nabla I_\nu = 0. \tag{2.58}$$

In general, one should also account for radiation sources and sinks. Incorporating them in equation (5.4) gives

$$\frac{1}{c}\frac{\partial I_\nu}{\partial t} + \hat{n}\cdot\nabla I_\nu = j_\nu - \chi_\nu I_\nu, \tag{2.59}$$

where χ_ν and j_ν are the absorption and emission coefficient of the matter respectively. The equation of radiative transfer (equation 2.59) describes the evolution of specific intensity as radiation propagates in a medium with radiation sources and sinks. Solving equation (2.59) with full generality could be quite complex. Thus, certain physical approximations have to be assumed to solve this equation. The most widely used method particularly in optically thick region is the flux limited diffusion (FLD).

The radiation transport equation can be reduced to FLD form by transforming it into evolutionary equations for various moments. We multiply equation (2.59) with 1 and $\hat{n}$ successively and integrate over angles to obtain energy density and radiation flux. Then, using the definitions of various moments of specific intensity (see equations 2.54-2.56) we obtain

$$\frac{\partial E_\nu}{\partial t} + \nabla\cdot\vec{\mathcal{F}_\nu} = 4\pi j_\nu - \chi_\nu c E_\nu, \tag{2.60}$$

and

$$\frac{1}{c}\frac{\partial\vec{\mathcal{F}_\nu}}{\partial t} + c\nabla\cdot\mathcal{P}_\nu = -\chi_\nu\vec{\mathcal{F}_\nu}. \tag{2.61}$$

In the FLD approximation, the radiation is treated as a photon fluid which diffuses out in an optically thick matter distribution. This approximation holds true for cases in which the mean free path of photon (see equation 2.49) is much less than any of the physical scales considered in this problem. Assuming $\chi_\nu >> 1$, equation (2.59) in first approximation can be given by

$$I_\nu \approx \frac{j_\nu}{\chi_\nu} = S_\nu, \tag{2.62}$$

which implies that the radiation is in equilibrium with the medium. Now, assigning temperature T to the medium, the source function S_ν simply is the Planck function $B_\nu(T)$. Also, if the radiation field is treated to be isotropic, the Eddington approximation relates the radiation pressure with energy density as

$$\mathcal{P} = \frac{1}{3}E\mathbf{I}, \tag{2.63}$$

where $\mathbf{I}$ is the identity matrix.

Substituting equation (2.63) in equation (2.61) we get

$$\frac{1}{c}\frac{\partial\vec{\mathcal{F}_\nu}}{\partial t} + \frac{c}{3}\nabla E_\nu = -\chi_\nu\vec{\mathcal{F}_\nu}. \tag{2.64}$$

Thus equations (2.60) and (2.64) form a closed set for the moments E_ν and $\vec{\mathcal{F}}_\nu$ and can be solved in conjunction with hydrodynamic equations (equations 2.1-2.5) for the problems considered here (see Chapter 5).

In the steady state ($\frac{\partial \vec{\mathcal{F}}}{\partial t} = 0$) condition, equation (2.64) becomes,

$$\vec{\mathcal{F}}_\nu = -\frac{c}{3\chi_\nu}\nabla E_\nu. \tag{2.65}$$

The radiation flux is thus represented as a function of the gradient of radiation energy, E_ν. In doing this, we get rid of the radiation momentum density and thus substantially simplify the radiation transport equation. The radiative flux need not be kept as a separate variable and can be eliminated using equations (2.60) and (2.65),

$$\frac{\partial E_\nu}{\partial t} - \nabla \cdot \left(\frac{c}{3\chi_\nu}\nabla E_\nu\right) = 4\pi j_\nu - \chi_\nu c E_\nu. \tag{2.66}$$

This is a parabolic equation, similar to the one describing the diffusion of heat. Now, consider dropping the source and the sink term on the RHS of equation (2.66), then, the equation is a wave equation that spreads according to $x \sim \sqrt{ct/3\chi_\nu}$. In such a case, if a transport is non- diffusive ($\chi_\nu ct < 1$) then the propagation of radiation pulse at t=0 could be faster than speed of light. This is due to the fact that there is no limit on the flux as seen from equation (2.65). *Ad hoc* methods have been developed to ensure that the flux is limited to give a physical result in such cases. They are called the flux limiters (e.g. Levermore & Pomraning 1981). The forms of these flux limiters will be discussed in Chapter 5 along with the numerical implementation.

2.4.3 Line driven winds

Hot massive OB stars are known to have strong mass loss in the form of stellar winds during later stages of their life times. The derived mass loss rates are typically of the order of 10^{-6} $M_\odot\,yr^{-1}$. The stellar winds are primarily radiation driven via a so-called *line driving mechanism* (e.g. Kudritzki & Puls 2000, Owocki 2009). In this process, the gas is accelerated by transferring momentum from the photospheric photons to the stellar atmosphere plasma through absorption of spectral lines. Thus, the wind properties depend on the number of lines being available and also on their ability to absorb these lines (i.e. optical thickness). The velocities measured in these winds are high, ranging from $\sim 500 - 1000\,km\,s^{-1}$ and are usually supersonic.

This theory was first developed by Castor et al. (1975) who solved the radiative transfer equations from spectral lines in moving atmospheres. According to their studies (hereafter the CAK theory), the force due to lines transfer can be expressed as a product of force due to continuum

radiation and a force multiplier,

$$M(\mathcal{T}) = \sum_{\text{lines}} \left(\frac{\Delta\nu_{\rm D}\mathcal{F}_\nu}{\mathcal{F}} \frac{1 - e^{-\eta\mathcal{T}}}{\mathcal{T}} \right), \tag{2.67}$$

where $\Delta\nu_{\rm D}$ the Doppler shift, $\mathcal{F}_\nu$ the radiation flux at frequency ν, and $\mathcal{F}$ the total integrated flux. The optical depth parameter $\mathcal{T}$ is related to the gradient of velocity, the density in the wind and the ion thermal velocity $u_{\rm th}$,

$$\mathcal{T} = \frac{\rho\sigma_e u_{\rm th}}{|\hat{n} \cdot \nabla(\hat{n} \cdot \vec{u})|}. \tag{2.68}$$

The optical depth parameter $\mathcal{T}$ can be related to the optical depth of a particular line $\tau_{\rm L}(\hat{n}) = \eta\mathcal{T}$. The *line strength* η is the ratio of the line opacity $\kappa_{\rm L}$ to the electron scattering opacity $\sigma_{\rm e}$, while $\hat{n}$ is the unit vector along the line of sight (l.o.s.). The classification of lines in optically thin and thick lines is done on the basis of interaction probabilities. Optically thick lines are those which have interaction probability of unity. Lines with optical depths $\tau_{\rm L} < 1$ are optically thin, and their probability of interaction is $\tau_{\rm L}$. Based on this approximation, the force multiplier is separable and can be written differently for very high or very low optical depths. When the gas is optically thick, $\tau_{\rm L} > 1$, the force multiplier depends only on the local dynamical quantities of the flow,

$$M_{\rm thick}(\mathcal{T}) = \sum_{\text{thicklines}} \left(\frac{\Delta\nu_{\rm D}\mathcal{F}_\nu}{\mathcal{F}} \frac{1}{\mathcal{T}} \right), \tag{2.69}$$

while for the optically thin case $\tau_L < 1$ the force multiplier is independent of the local dynamics, but depends on the line strength of individual thin lines,

$$M_{\rm thin}(\mathcal{T}) = \sum_{\text{thinlines}} \left(\frac{\Delta\nu_{\rm D}\mathcal{F}_\nu}{\mathcal{F}} \eta \right). \tag{2.70}$$

In general, for a gas distribution with a mixture of optically thick and thin lines, the empirical form of the total force multiplier integrated over all lines can be expressed as a power law, $M(\mathcal{T}) \sim k\mathcal{T}^{-\alpha}$, where k and α are line force parameters (Castor et al. 1975). Depending on the selection of lines, for massive OB stars typical values obtained for k range from 0.4-0.6, while α ranges between 0.3 and 0.7 (Abbott 1982). Physically, the value of k is proportional to the total number of lines. The quantity α can be considered as a measure for the ratio of acceleration from optically thick lines to the total acceleration (Puls et al. 2000).

A *general* parametrization for the force multiplier which is independent of arbitrary $u_{\rm th}$ has been introduced by Gayley (1995). In his formulation, the constant k initially introduced by Castor et al. (1975) has been replaced by $\bar{Q}$ and the force multiplier can be expressed as follows,

$$M(\mathcal{T}) = \left[\frac{\bar{Q}^{1-\alpha}}{1-\alpha} \left(\frac{|\hat{n} \cdot \nabla(\hat{n} \cdot \vec{u})|}{\sigma_{\rm e} c\rho} \right)^{\alpha} \right]. \tag{2.71}$$

The *strongest form* of this parameterization requires the ansatz $\bar{Q} = Q_0$, where Q_0 being the line strength of the strongest line.

Typically for massive stars, the parameter $\bar{Q}$ lies in the range of 1000-2000 (Gayley 1995). For our present study, we have applied the force multiplier considering this *general* parameterization in its *strongest form*. Thus, we have the two parameters Q_0 and α which define the force multiplier (Eq. 2.71) and hence the line forces. One of the important properties of the force multiplier $M(\mathcal{T})$ is that its value saturates to a maximum value $M_{\max}$ when the medium becomes optically thin and the optical depth parameter approaches a minimum value, $\mathcal{T} \leq \mathcal{T}_{\min}$. The typical value for the maximum force multiplier is relatively constant, $M_{\max} \sim 10^3$, depending only on the metallicity (Gayley 1995).

2.5 Numerical code

The numerical calculations performed in this thesis are done with a modular code PLUTO (Mignone et al. 2007). PLUTO is a versatile code written in C language and is used for solving various astrophysical problems in 1, 2 and 3 spatial dimensions for different system of coordinates. The code provides a multi-physics, multi-algorithm modular environment and is built on a Godunov-type shock capturing schemes. The code is fully parallelized using the Message Passing Interface (MPI) library.

PLUTO is designed to integrate a general system of conservation laws given by

$$\frac{\partial \mathbf{U}}{\partial \mathrm{t}} = -\nabla \cdot \mathbf{T}(\mathbf{U}) + \mathbf{S}(\mathbf{U}). \tag{2.72}$$

Here, $\mathbf{U}$ is a state vector of conservative quantities, $\mathbf{T}(\mathbf{U})$ is a rank-2 tensor with rows as fluxes of each component of $\mathbf{U}$ and $\mathbf{S}(\mathbf{U})$ represents the source terms. In this work, I have used two non-relativistic modules of the code - HydroDynamics(HD) and MagnetoHydroDynamics(MHD). The equations which are solved by the PLUTO code are listed in a tabulated form for both the modules (see Table A.1).

In general, the code follows a standard four step approach in solving equation (2.72) irrespective of the selected module :

I Volume averages $\mathbf{U}$ are mapped into primitive variables $\mathbf{V}$.

II A piecewise polynomial is constructed by interpolating cell centered primitive variables $\mathbf{V}$ at each cell to get the left and right state at the cell edges.

III A Riemann problem is solved to obtain the flux at the interface. The input to the solver are the left and right states obtained from reconstruction as described above.

IV Finally using these fluxes at the interface, the solution is advanced in time.

Such a general scheme to solve conservative equation does not naturally preserve the solenoidal condition, which is very crucial for problems related to MHD. There are number of techniques implemented in the PLUTO code to ensure that no monopoles exists. The problem of jet launching considered in the present thesis (see Chapter 4) applies to the method of Constraint Transport (CT) (Gardiner & Stone 2005). In the CT formulation, the cell centered magnetic field additionally has staggered components and the induction equation is integrated directly using Stoke's theorem.

In almost all of our numerical setup, we use piecewise linear interpolation to construct the left and the right states of the primitive variables. The discretization in space is 2^{nd} order accurate. The time-marching for explicit numerical integration is done using the second-order Runge Kutta method. The time step Δt is limited by Courant, Friedrichs and Lewy (CFL) condition (Courant et al. 1928). The Riemann solver chosen for our setup is HLL (e.g. Toro et al. 1994).

In grid based numerical codes, there are mainly two zones - (i) the active zone (domain), where the equations are solved and (ii) the ghost zone (boundaries), where the boundary conditions are prescribed depending upon the problem. The boundary conditions usually are dependent on the values in the active zone. The PLUTO code comes with many pre-defined boundary conditions as modules to be defined in the initial setup file. For example, the *outflow* boundary condition is in which the values of various quantities in the ghost zone are copied from the first active zone. The PLUTO code also gives the flexibility of prescribing user defined boundary conditions as required by the problem under consideration.

The PLUTO code is developed specially to deal with problems related to jet dynamics. The code has very robust shock capturing schemes which are vital for such problems. The code is well tested for numerous standard test problems for all physical modules and in all geometries. In this work, I have modified the original code to include additional physics for solving numerical problems related to jet and accretion disk dynamics. Details of these modifications are presented in Chapters 4 and 5.

The main purpose of science is simplicity
and as we understand more things,
everything is becoming simpler.

Edward Teller (1908-2003)

3

Analytical study of inner accretion disk around massive YSO

This chapter is based on a paper titled - Accretion Disks Around Massive Stars: Hydrodynamic Structure, Stability, and Dust Sublimation published in the The Astrophysical Journal by Bhargav Vaidya, Christian Fendt & Henrik Beuther (Vaidya et al. 2009).

We investigate the structure of accretion disks around massive protostar applying steady state models of thin disks. The thin disk equations are solved with proper opacities for dust and gas taking into account the huge temperature variation along the disk. We explore a wide parameter range concerning stellar mass, accretion rate, and viscosity parameter $\alpha_{\rm v}$. The most essential finding is a very high temperature of the inner disk. For e.g. a 10 $M_\odot$ protostar and an accretion rate of $\sim 10^{-4}$ $M_\odot\,{\rm yr}^{-1}$, the disk mid-plane temperature may reach almost 10^5 K. The disk luminosity in this case is about 10^4 $L_\odot$ and, thus, potentially higher than that of a massive protostar. We motivate our disk model with similarly hot disks around compact stars. We calculate a dust sublimation radius by turbulent disk self-heating of more than 10 AU, a radius, which is 3 times larger than caused by stellar irradiation. We discuss implications of this result on the flashlight effect and the consequences for the radiation pressure of the central star. In difference to disks around low mass protostars our models suggest rather high values for the disk turbulence parameter $\alpha_{\rm v} \leq 1$. However, disk stability to fragmentation due to thermal effects and gravitational instability would require a lower $\alpha_{\rm v}$ value. For $\alpha_{\rm v} = 0.1$ we find stable disks out to 80 AU. Essentially, our model allows to compare the outer disk to some of the observed massive protostellar disk sources, and from that, extrapolate on the disk structure close to the star which is yet impossible to observe.

3.1 Introduction

Massive stars play a vital role in order to understand the dynamical evolution of clusters in which they are the major source of heavy elements and UV radiation. During their short life time, they impact their surrounding by a number of physical processes such as jet like outflows, strong winds, photo evaporation, expanding HII regions and eventually supernova explosions (Zinnecker & Yorke 2007, Beuther 2007). Collimated molecular outflows and jets from young massive protostars have been observed (Beuther et al. 2002b, Beuther & Shepherd 2005), although the launching mechanism for outflows have been mainly investigated for low mass protostars so far (see e.g. Casse & Keppens 2002, Pudritz et al. 2007, Fendt 2009).

Understanding massive star formation has been a very active field of research for both the observers and the theorists. The basic differences of high and the low mass star formation process are that of timescales, energy scales, mass flow rates and high luminosity of the central star. Low mass stars have well defined phases in their formation process and they only start burning hydrogen after accretion of all matter is done (Stahler & Palla 2005). In contrast, massive stars have very short Kelvin Helmholtz time of $\sim 10^4 - 10^5$ yr, and thus start burning hydrogen even when they are still accreting. One of the problems in the formation of massive stars is that, at some point in time, the strong radiation pressure from the luminous central star may exceed the Eddington limit in spherical symmetry and does not allow the matter to accrete anymore. This seems to limit the mass of the star to be formed via the spherical accretion to about 20 $M_\odot$ (Wolfire & Cassinelli 1987).

However, disk accretion may add dynamical pressure to the accreting matter which may help overcoming the stellar radiation pressure. Thus, the star formation scenario for low and high mass stars could in principle be the same (e.g. Keto 2007), suggesting that high mass star formation as a scaled up version of the low mass star formation process. We aim to construct a *global model* (length scales of $\sim$ 0.1 AU to 100 AU) of the accretion disk around massive young stars. By fitting the outer disk structure to the observations, this will allow us to investigate, the feasibility of certain physical processes in inner disk which could be essential for the pre-stellar evolution as angular momentum transport or processes responsible for launching of outflows.

This chapter relies on one essential assumption - that is the disk accretion rate. Both estimates following the observed *outflow* rates and the time scale of mass aggregation suggest accretion rates in the range of $10^{-3} - 10^{-4}$ $M_\odot\,yr^{-1}$ (Beuther et al. 2002b, Zhang 2005, Grave & Kumar 2009). However, one of the aims of our study is to understand whether such values are compatible with theoretical accretion disk models.

In order to study the *global* disk structure around massive stars, we apply the standard thin disk model (Shakura & Syunyaev 1973, Morfill & Wood 1989, Ruden & Pollack 1991, Frank et al.

1992, Stepinski et al. 1993, Bell & Lin 1994, see Sect. 2.3.1) with appropriate modifications. The essential part of our model is to take into account the proper gas and dust opacities for a huge temperature regime as indicated for high accretion rates on to massive stars. The steady state state hydrodynamical equations (2.38-2.44) were solved including dust opacities that has been applied to disks around low mass stars and solar nebula (Ruden & Pollack 1991, Stepinski et al. 1993, Stepinski 1998, Del Popolo & Ekşi 2002). The application of such a thin disk model to massive stars is a simple approach to understand the dynamics of the disk especially in the inner most region which can not be resolved with the help of present day telescopes.

3.2 Disk opacities

The work done by Shakura & Syunyaev (1973) was mainly focused on hot accretion disks around black holes, the contribution to the opacity in their case was mainly from the electron scattering or free-free emission depending upon the optical depth in the disk. However in disks around massive young stars, contribution to opacity also comes from dust present beyond the sublimation radius, many molecular and atomic lines and other scattering processes. Since massive stars have large radiation fields that heavily affect the huge amount of dust present in the envelope and also the gas that is present in the inner part, one has to take into account a proper contribution of opacities from dust and gas to have a consistent accretion disk model.

In our model the dust opacity does not have any explicit dependence on frequency, so the effective value of the opacity

$$\kappa_{\rm eff} = \frac{\int \kappa_\nu \mathcal{F}_\nu d\nu}{\int \mathcal{F}_\nu d\nu} \tag{3.1}$$

simplifies to $\kappa_{\rm eff} = \kappa_\nu$.

We follow that the matter is accreted via a disk investigating the possible location of the dust sublimation radius. The expectation is that the active disks will be dominating in destroying the dust in the disk at a much further radius then it would have been destroyed by the heating from star. This would result in lowering the radiation pressure on the dust and allowing the infall of matter on the central star.

Apart from some metal silicates all the dust grains that are present sublimates at around 1500 K. Since at this temperature, the gas and the dust opacities vary substantially, it is essential for calculating radiation pressure to consider the proper opacity.

3.2.1 Dust opacities

There are many factors one has to take into account for getting a consistent model for dust opacity such as the size of the grains, distribution of grains in the disk and the coagulation of dust grains. Also the temperature of the disk varies over a large range and this would clearly affect the composition of the dust and alter the gas to dust ratio typically ~ 100 in the disk. This radial variation in the gas to dust ratio will not only modify the gas pressure along the disk but also the other dynamical disk quantities. The usual assumption in many of the dust models is that the dust and gas are well coupled and also the gas to dust ratio is taken to be 100. In general, opacity has a typical dependence on temperature and density. (e.g. Morfill & Wood 1989, Ruden & Pollack 1991, Bell & Lin 1994, Ossenkopf & Henning 1994, Helling et al. 2000, Semenov et al. 2003).

In the regime which is dominated by dust ($r \gg R_*$), the opacity depends very weakly on density. In the present work we apply for the dust dominated region the model proposed by Ruden & Pollack (1991) in which the Rosseland mean opacities have been given in terms of the power laws of the form given in equation (2.43), in different regimes that have been distinguished on the basis of temperature and mass density (see Table 3.1). Using this power law form of opacity, equations (2.38-2.43) can be reduced to a form representing the viscosity as a function depending on surface density and the radial distance as

$$\vartheta = C\Sigma^p r^q \tag{3.2}$$

This form of viscosity can be then substituted in equation (2.44) so that all the dynamical quantities namely the surface density, mass density, central temperature, scale height of the disk can be expressed as power laws of mass, accretion rate, radial distance and the viscosity parameter $\alpha_{\rm v}$. For the parameters of a typical massive star these quantities (Q) can be written

$$Q = C_i \left(\frac{\dot{\rm M}}{10^{-3}\ {\rm M}_\odot\ {\rm yr}^{-1}} \right)^{\beta_i} \left(\frac{M_*}{{\rm M}_\odot} \right)^{\gamma_i} \alpha_{\rm v}^{\delta_i} \left(\frac{r}{R_i} \right)^{\epsilon_i} \tag{3.3}$$

(e.g. Ruden & Pollack 1991, Stepinski et al. 1993, Del Popolo & Ekşi 2002). Here $\dot{\rm M}$ is the mass accretion rate, M_* the mass of the star and r is the radial distance in the disk. The index i denotes the opacity regime as given in the Table 3.1. ($i = 1, 2...6$), C_i are constants and R_i is chosen as a typical radius for that regime. The dust model taken into account does not consider explicit wavelength dependence of opacity.

Table 3.1: Different regimes of the opacity taken from Ruden & Pollack (1991) with the conditions for the change over and description of the main components of dust in each regime

Regime	κ_i	Condition	Description
1	$\left(2\times10^{-4}\right)\rho^0T^2$	$T \leq 150\,\mathrm{K}$	dominated by Water and Ice grains
2	$\left(1.15\times10^{18}\right)\rho^0T^{-8}$	$T \leq 180\,\mathrm{K}$	Sublimation of Ice grains
3	$\left(2.13\times10^{-2}\right)\rho^0T^{0.75}$	$T \leq 1380\,\mathrm{K}\left(\frac{\rho}{10^{-8}}\right)^{1/50}$	mainly consists of Iron and Silicate grains
4	$\left(1.57\times10^{60}\right)\rho^{3/8}T^{-18}$	$T \leq 1890\,\mathrm{K}\left(\frac{\rho}{10^{-8}}\right)^{1/48}$	Sublimation of refractory grains
5	$\left(1.6\times10^{-2}\right)\rho^0T^0$	$T \leq 2620\,\mathrm{K}\left(\frac{\rho}{10^{-8}}\right)^{2/27}$	Molecular and atomic lines contribute
6	$\left(2\times10^{34}\right)\rho^{2/3}T^{-9}$	$T \leq 3200\,\mathrm{K}$	Molecular and atomic lines contribute

3.2.2 Gas opacities

The opacity of gas and dust have been estimated consistently. These opacities are usually listed in form of a table in two parameters space, temperature (T) and parameter (R) which is dependent on density in a following manner

$$R = \frac{\rho}{(T_6)^3} \tag{3.4}$$

(Iglesias & Rogers 1996, Ferguson et al. 2005) where ρ is the density and T_6 is the temperature normalized to 10^6 K. These opacities also show some dependence on metallicity as well.

In a regime where dust begins to sublimate and molecules start to form, there is a sharp decrease in the opacity. In this regime, dependence of opacity on density is strong, unlike the opacity due to dust, and in general it is very difficult to get the true value of the opacity in this region so usually linear interpolation is used (Semenov et al. 2003). Due to steep turn over of the opacity gradient with the temperature, numerical difficulties arise when the dynamical quantities are estimated for this region. In the present work, we take into account the opacity table [a] by Ferguson et al. (2005), which has the temperature range of our relevance (500 K - $10^{4.5}$ K). For the present purpose we choose a table with hydrogen fraction X = 0.94 and metallicity Z = 0.06. In fact, we also in the inner most region obtain higher temperatures and so we apply in continuation the OPAL opacity tables [b] for higher temperatures ($\geq 10^{4.15}$ K) (Iglesias & Rogers 1996). We create an equispaced grid of two parameters log(T) and log(R) as defined above and put the values from the table in the grid and fit a 2D cubic spline on it to get the interpolated values of opacity for any given temperature and density, but as the regime where the gas and dust coexists is difficult to model numerically as the opacity do not converge to a unique value, we make a linear approximation as zeroth order approach and compare with the analytical models

[a] http://webs.wichita.edu/physics/opacity
[b] http://www-phys.llnl.gov/Research/OPAL/opal.html

present. (e.g. Ruden & Pollack 1991, Bell & Lin 1994).

3.3 Outer disk structure

The main contribution of opacity in the outer disk is from dust. The numerical values for the dynamical quantities expressed as given by equation (3.3) in different opacity regimes are listed in Table 3.2. The radial profile of the disk mid-plane temperature, surface density, mass density and scale height for a high mass star is shown in Fig. 3.1 for a 10 $M_\odot$ star with accretion rate of the order of 4.2×10^{-4} $M_\odot\,yr^{-1}$ and the a viscosity parameter $\alpha_v = 1$. With these parameters, the central temperature reaches 1500 K around 12 AU due to viscous heating, which causes the dust to sublimate. Figure 3.1 shows two curves for each quantity. The solid curve is obtained by implementing the opacity power laws as given by Ruden & Pollack (1991), whereas the dashed line is obtained by using the opacities by Stepinski et al. (1993) and extrapolating it to higher mass stars.

There are few kinks seen in the plot, which are due to the fact that the dust opacity model used comprises of different regimes and in each of these regimes have a different form of power law (see Table 3.1). These regimes are connected using the standard procedure (Lin & Papaloizou 1985) of equating the opacity in two consecutive regimes, $\kappa_i = \kappa_{i+1}$.

Since formation of massive stars involves large accretion rates the surface density and the mass density in the disk is higher than the lower mass counterparts, as more matter will be injected in the inner region. We find the scale height ratio obtained from the present model is approximately constant in the outer disk, with a radial dependence $\propto r^{0.28}$ and consistent with the thin disk approximation.

A least square linear fit of dynamical quantities gives for the temperature profile a power for the radial distance as -0.45 and for density as -2.35. The surface density has a rather flat profile as the best fit gives the dependence of the form $\propto r^{-1.1}$. These profiles are similar to those obtained by Ruden & Pollack (1991) but here applied for a high mass star with high accretion rate.

The parameter values discussed above were chosen i) to have most part of the inner 100 AU disk to be gravitationally stable and also ii) to ensure that the dust in the disk sublimates at a distance substantially further than caused by sublimation from stellar irradiation. (see below)

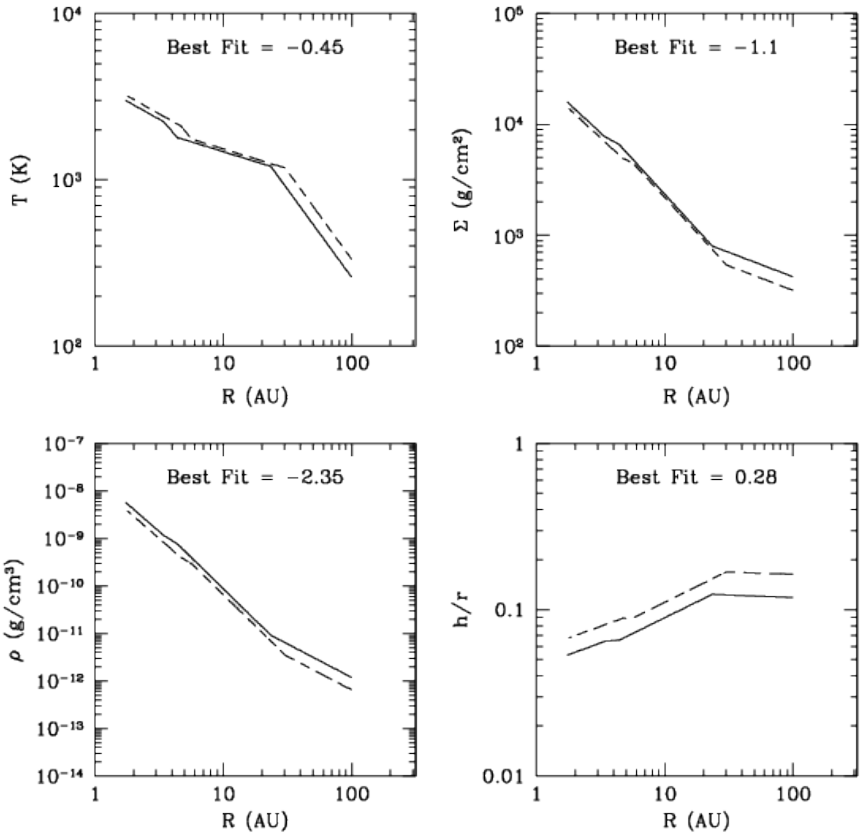

Figure 3.1: Radial profiles of mid-plane temperature (T), mass density (ρ), surface density (Σ) and the scale height ratio (h/r) for the outer dust dominated disk. The *dashed line* represents the tabulated values (see Table 3.2), the *solid line* is obtained by using the Ruden & Pollack (1991) opacity power laws. These plots are for typical $\dot{M} = 4.2 \times 10^{-4}$ $M_\odot\,yr^{-1}$, stellar mass $M = 10$ $M_\odot$ and $\alpha_v \sim 1$. The radial index of the best fitted linear plot are mentioned in each subplot.

Table 3.2: The various dynamical quantities for the massive star using the interpolated Rosseland mean dust opacity model given by Ruden & Pollack (1991).(see equation (3.3) and Table 3.1)

		Regime 1 $R_1 = 400$ AU		
Q	T[K]	Height[cm]	ρ[g cm^{-3}]	Σ[g cm^{-2}]
C_i	126.3	9.9×10^{14}	1.3×10^{-13}	258.8
		Regime 2 $R_2 = 250$ AU		
Q	T[K]	Height[cm]	ρ[g cm^{-3}]	Σ[g cm^{-2}]
C_i	169.8	5.7×10^{14}	3.4×10^{-13}	393.1
		Regime 3 $R_3 = 50$ AU		
Q	T[K]	Height[cm]	ρ[g cm^{-3}]	Σ[g cm^{-2}]
C_i	814.5	1.12×10^{14}	4.1×10^{-12}	907.6
		Regime 4 $R_4 = 10$ AU		
Q	T[K]	Height[cm]	ρ[g cm^{-3}]	Σ[g cm^{-2}]
C_i	1613.2	1.4×10^{13}	1.8×10^{-10}	5126.4
		Regime 5 $R_5 = 6$ AU		
Q	T[K]	Height[cm]	ρ[g cm^{-3}]	Σ[g cm^{-2}]
C_i	1918.3	7.1×10^{12}	6.5×10^{-10}	9282.8
		Regime 6 $R_6 = 3$ AU		
Q	T[K]	Height[cm]	ρ[g cm^{-3}]	Σ[g cm^{-2}]
C_i	2767.9	3.0×10^{12}	3.0×10^{-9}	1.8×10^{4}

3.4 Sublimation of dust

Most of the dust grains sublimate when the temperature in the disk reaches the critical value of 1500 K. The radius of the disk at which this value of critical temperature is reached is the dust sublimation radius. The disk can be heated by various processes such as viscous heating, stellar irradiation, convection, cosmic rays (D'Alessio et al. 1998). However, in the present work we estimate the dust sublimation radius via two main processes namely viscous heating and stellar irradiation (see Table 3.3).

3.4.1 Disk Self-Sublimation of dust

For our massive stellar disk model, we define that radius where the disk temperature reaches 1500 K as disk self-sublimation radius. Essentially, the disk temperature is determined by $\dot{\mathrm{M}}$, while the radial velocity is governed by α_{v}. The higher the accretion rate, more the gravitational potential energy from the accreted mass is converted to thermal energy in the inner region, thus increasing the disk temperature. High mass accretion rates $\sim 10^{-3} - 10^{-4}$ $\mathrm{M_\odot\,yr^{-1}}$ are indirectly related to the formation of massive stars, indicating hotter disks in massive stars.

The dust sublimation radius can be estimated from the temperature profile in regime 4 (see Table 3.2) as the critical value of 1500 K is obtained in this regime,

$$T = 1.6 \times 10^3\,\mathrm{K}\,\alpha_{\mathrm{v}}^{-0.058}\left(\frac{\dot{\mathrm{M}}}{10^{-3}\ \mathrm{M_\odot\,yr^{-1}}}\right)^{0.101}\left(\frac{M}{\mathrm{M_\odot}}\right)^{0.080}\left(\frac{r}{10\,\mathrm{AU}}\right)^{-0.239} \tag{3.5}$$

Thus the dust self-sublimation radius is

$$R_{\mathrm{sub,disk}} = 10\,\mathrm{AU}\,\alpha_{\mathrm{v}}^{-0.242}\left(\frac{\dot{\mathrm{M}}}{5\times10^{-4}\ \mathrm{M_\odot\,yr^{-1}}}\right)^{0.422}\left(\frac{M}{10\ \mathrm{M_\odot}}\right)^{0.3347}\left(\frac{T}{1500\,\mathrm{K}}\right)^{-4.184} \tag{3.6}$$

3.4.2 Dust Sublimation by Stellar radiation

The second process of disk heating is by radiation from the central star. The dust sublimation radius due to the absorption of UV radiation from the star by the disk is dependent on the effective temperature and the radius of the star or equivalently to the luminosity of the star. We can estimate the relation between the temperature of the disk and the temperature of the star just by equating the flux from the star that is absorbed by the disk to the flux emitted by it considering it as black body. The disk is also assumed to be locally isothermal, which is an appropriate assumption for optically thick disks The mid plane temperature of the disk due to heating from

central star can be estimated,

$$T_{\rm d} = \left(\frac{\theta\psi_{\rm s}}{2\psi_{\rm i}}\right)^{1/4} \left(\frac{R_*}{r}\right)^{1/2} T_* \tag{3.7}$$

(e.g. Dullemond et al. 2001) where θ is the angle with which the radiant flux is incident on the flaring disk, $\psi_{\rm s}$ denotes the fraction of flux that is absorbed by the interior and $\psi_{\rm i}$ is correction factor which accounts for the fact that the disk interior is not fully optically thick for its emission. The small correction due to back-warming in the disk is neglected. This correction mainly depends on the underlying dust properties (Monnier & Millan-Gabet 2002). For a dust sublimation temperature of $\sim$ 1500 K, we can estimate the sublimation radius due to absorption of radiation from the above equation (3.7) noted as Measure A whereas Measure B we denote as the sublimation radius calculated using the standard formula given by Monnier & Millan-Gabet (2002). In Table 3.3 we show the typical values of the sublimation radius from these measures. For a typical B2 star of mass = 10 $M_\odot$ and $T_{\rm eff}$ = 22000 K (Lang 1992) with ZAMS value for the stellar radius as 6 $R_\odot$, one gets a dust sublimation radius due to heating from stellar radiation of $R_{\rm sub,*} \sim 4$ AU for measure A and $\sim$ 3 AU for measure B. This value may increase by a factor of 2 considering the bloating star model (Hosokawa & Omukai 2008), where the star bloats up to 100 $R_\odot$ and the effective temperature reduces to 5000 K.
In Table 3.3, we compare for different stellar mass with typical order of mass accretion rate, the sublimation radius due to self heating from the disk and that due to heating from the star. This values are estimated for two different values of $\alpha_{\rm v} = 0.1, 1$. It is evident from Table 3.3 that the dust sublimation radius due to heating from disk is a weak function of $\alpha_{\rm v}$. Table 3.3 further indicates a ratio $R_{\rm sub,disk}/R_{\rm sub,*} \sim 3$ as a good estimate over a wide range of mass accretion rates and stellar mass.

The value of $\alpha_{\rm v}$ is related to the radial transport of matter in the disk, thus the mass accretion rate is a function of $\alpha_{\rm v}$. For Table 3.3, the values of the sublimation radius is estimated using equation (3.5) assuming the same mass accretion rate for different $\alpha_{\rm v}$ values. These are representative values of sublimation radius for typical mass accretion rates found in massive star forming regions. Using these values we optimize the ratio of the self sublimation radius of the disk to that caused by heating from stellar luminosity is around three. With this assumption, we obtain a relation of $\alpha_{\rm v}$ and $\dot{\rm M}$ for a particular stellar mass. This is obtained by setting T = 1500 K in the equation (3.5) and the radial distance as $3 \times R_{\rm sub,*}$.

This relation can be used to have constraints on the mass accretion rates for a particular stellar mass. The plot for mass accretion rates with $\alpha_{\rm v}$ is shown in Fig. 3.2 for typical OB type stars. If one considers the value of $\alpha_{\rm v}$ as fixed to 1, then from the Fig. 3.2 for the 10 $M_\odot$ star one gets the accretion rate of 4.2×10^{-4} $M_\odot\,{\rm yr}^{-1}$, which implies that for this order of mass accretion rate the dust in the disk will sublimate at a distance of $3 \times R_{\rm sub,*}$. This clarifies that for the typical high accretion rates required for formation of high mass stars, the heating in the disk is very efficient

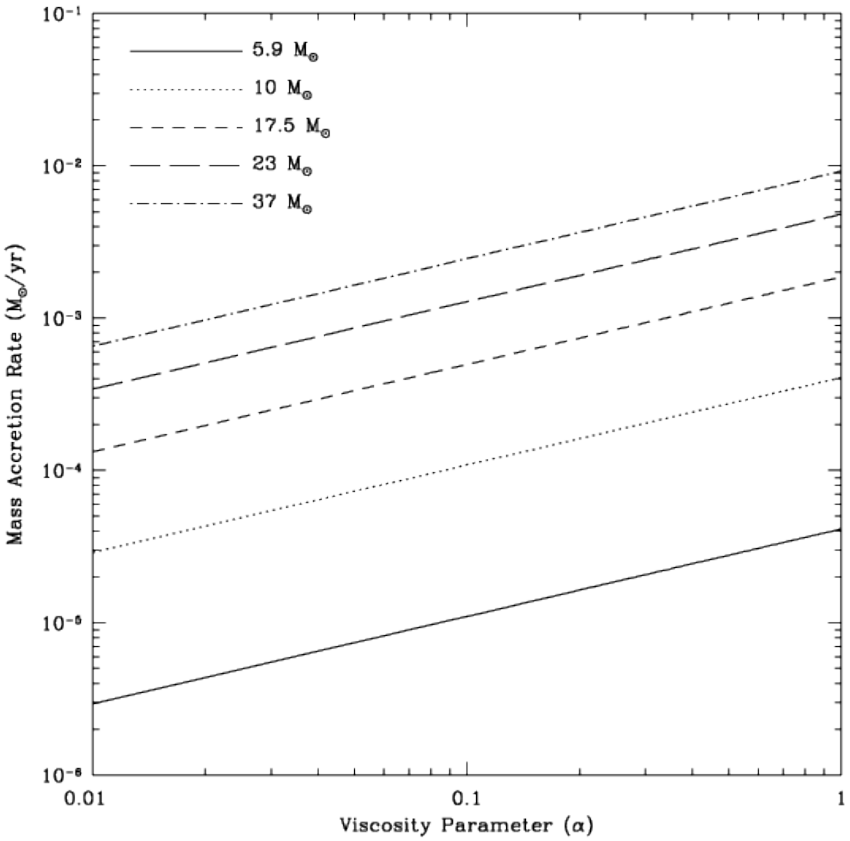

Figure 3.2: This plot shows the variation of mass accretion rate with the viscosity parameter so that the dust sublimation temperature due to viscous heating is around three times that of heating from star. The various lines are for different spectral type of stars (luminosity values obtained from Lang 1992). These plots indicate that mass accretion rate is a weak function of $\alpha_{\rm v}$.

to sublimate most of the dust grains in the mid-plane before the radiation could have any major effect on them.

The implication of this result is profound, as it demonstrates that viscous heating of the disk is the dominant mechanism in the mid-plane for sublimation of the dust. The self-sublimation in the turbulent massive disk sublimates most of the dust grains well before the stellar radiation could affect them. Essentially, this implies that more matter (in form of gas) can reach closer to the central star.

However, stellar radiation can have significant effects on the surface layer of the disk. The radial distance beyond which the stellar irradiation will dominate can be estimated by equating the flux from central star to the flux emitted from the disk. The flux from the disk is dependent on the

Table 3.3: Comparison of the sublimation radius due to heating in disk [equations (3.5) and (3.6)] and due to heating from the star [equation (3.7)]. The temperature of the star and its radius are taken from Lang (1992). (see Sect. 3.4 for details)

Typical $\dot{M}$ [$M_\odot\,yr^{-1}$]	Spectral Type	Stellar Mass ($M_\odot$)	$R_{sub,*}$[AU]		$R_{sub,disk}$ [AU]	
			Measure A	Measure B	$\alpha_v = 0.1$	$\alpha_v = 1$
5×10^{-5}	B5	5.9	1.4	1.0	5.4	3.1
5×10^{-4}	B2	10	4.2	3.0	17.5	10
5×10^{-3}	O6	37	24.5	17.3	72	41

effective surface temperature, which can be substantially lower than the mid-plane temperature depending on the optical depth. (see Sect. 3.5)

3.5 Inner gaseous disk structure

In order to model the inner gaseous region of the disk, we consider the OPAL opacity tables applicable for higher temperatures from Iglesias & Rogers (1996). The various dynamical quantities in the disk obtained using the opacity from the table and their comparison with the various analytical models are shown in Fig. 3.3. The variation of the opacity, used for the present work, from the opacity tables with the mid-plane temperature in the disk is shown in Fig. 3.4.

The midplane temperature reaches very high values of the order of 10^5 K at 20 $R_\odot$ (See Fig. 3.3). The radial profile for the temperature also shows a sudden break around 1 AU. This is related to the sudden rise in opacity around 3000 K as demonstrated in Fig. 3.4. Since the surface density and the mass density are inversely proportional to the temperature (see equations 2.38-2.44), their radial profiles show a sudden fall at that distance. Similar kind of sudden rise and fall can be seen also in the analytical results of Bell & Lin (1994) which are we show alongside in Fig. 3.3.

We also compare with analytical radial profiles obtained using opacities as given by Ruden & Pollack (1991). However these profiles just extent to the temperature range where the dust just sublimates and the opacity drops to a small value. These models fit very well in the outer disk region with the model described in the present work.
The high temperature up to $10^5\,K$ would imply a high ionization fraction in the disk close to the massive star. Thus the ionized gas could well couple to the large scale magnetic fields from ambient medium which is dragged by accretion and may give rise to collimated outflows.

In Fig. 3.3, the variation of the scale height is also shown with the radial distance. Similar to

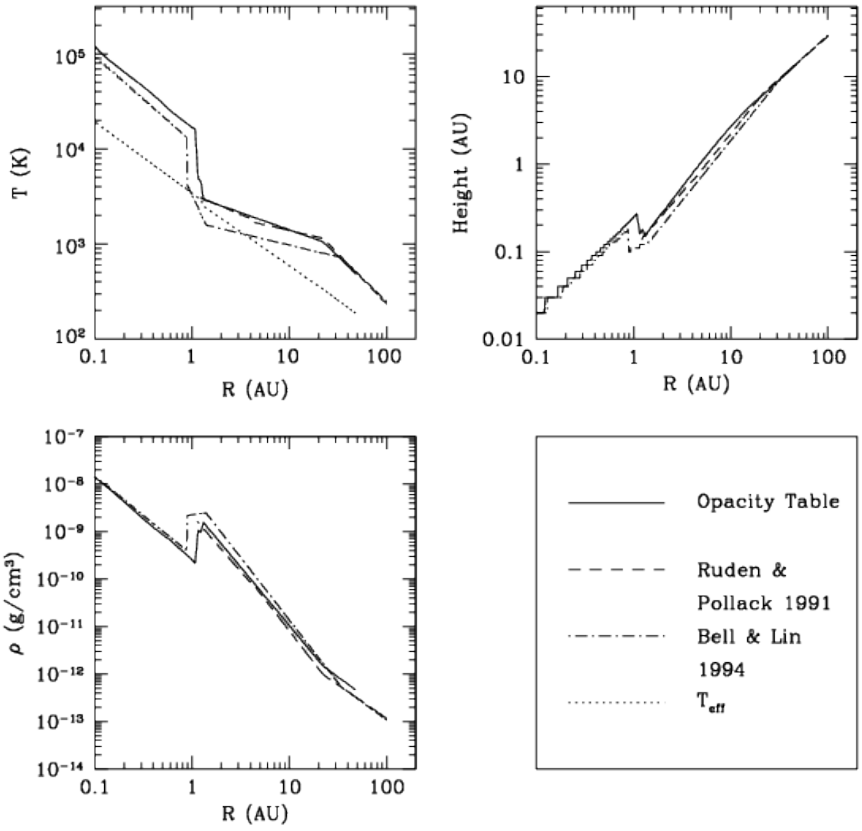

Figure 3.3: Radial profiles of temperature (T), mass density (ρ), scale height of the disk extended to the inner region. The *solid line* represents the values from opacity table (Ferguson et al. 2005) and OPAL (Iglesias & Rogers 1996) , the *dashed line* is using the opacity power laws by Ruden & Pollack (1991) and the *dot-dashed line* are the values for Bell and Lin opacity power laws. The *dotted line* shown in temperature profile represents the $T_{\rm eff}$ profile with radius whereas the other lines are for the mid-plane temperature. These plots are for typical $\dot{\rm M} = 4.2 \times 10^{-4}$ M$_\odot$ yr^{-1}, stellar mass $M = 10$ M$_\odot$ and $\alpha_{\rm v} \sim 1$

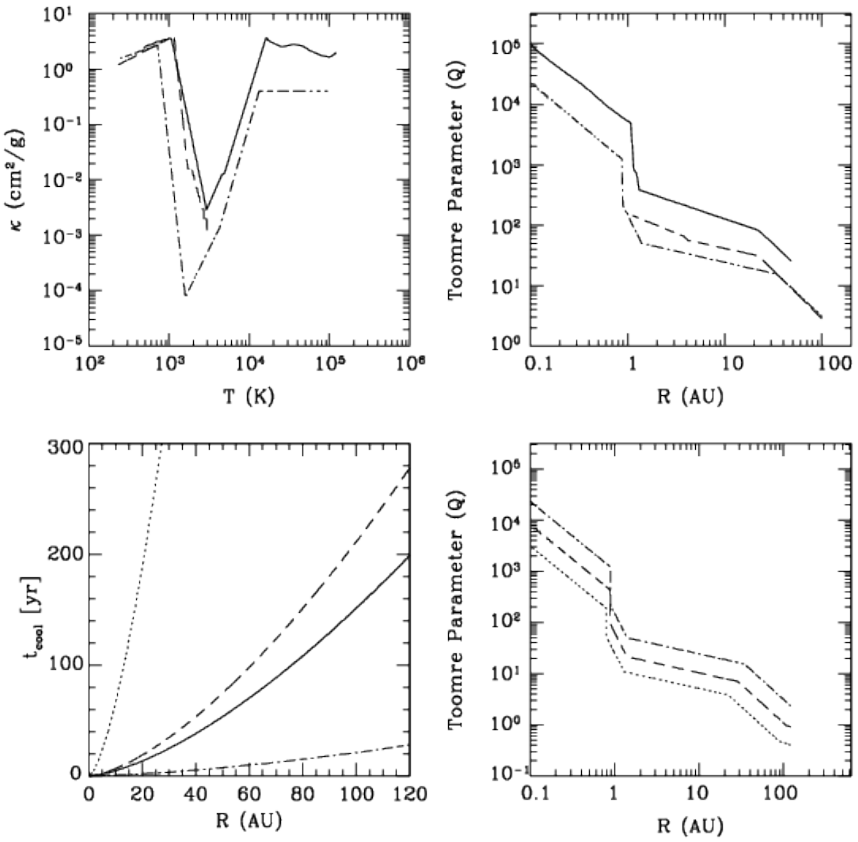

Figure 3.4: The opacity variation with temperature (*top left panel*), and the variation of Toomre parameter Q with the radial distance (*top right panel*). The *solid line* represents the values from opacity table (Ferguson et al. 2005) and OPAL (Iglesias & Rogers 1996), the *dashed line* is using the opacity power laws by Ruden & Pollack (1991) and the *dot-dashed line* are the values for Bell and Lin opacity power laws. The *bottom panels* shows how the variation of α_v values affect the cooling time and Toomre parameter, $\alpha_v = 0.01$ is denoted by *dotted line*, where as $\alpha_v = 0.1$ is *dashed line* and $\alpha_v = 1.0$ is by the *dot-dashed line*. *Solid line* in the curve represents the threshold condition for the fragmentation to set in.

radial profiles of other dynamical quantities, we get jump also in the profile of the scale height. This jump is quite interesting when dealing with disks around massive stars. The sudden rise of disk height around 1 AU would help to shield outer disk regions from the radiation of central source. This affects the direction of radiation and leading to some sort of anisotropy in the radiation field.

We also investigate the radial profiles of the dynamical quantities for higher mass stars. These profiles are shown in Fig. 3.5. The midplane temperature profiles clearly show that as the central mass and accretion rate increase, the midplane temperature also increases and so the self sublimation radius will move further out. For instance, with central mass as 23 $M_\odot$ and accretion rate of 4×10^{-3} $M_\odot\,yr^{-1}$, the dust sublimates at $\sim$ 30 AU whereas the dust sublimation radius is around 41 AU for a 37 $M_\odot$ star with disk accretion rate of 8.5×10^{-3} $M_\odot\,yr^{-1}$. These parameters are also chosen with the same argument as used for 10 $M_\odot$ star. Also, the temperature in the inner most region is much higher for massive young star with higher mass. The mass density and the surface density profiles also show the same trend of increment in the inner region with increase in mass of central object.

On might question the thin disk approach to study the disk around massive young stars. However, with this approach we find that the disk around high mass stars are very similar to that around cataclysmic variables. The spectral signatures of disk around these compact objects were very well explained by this thin disk model. The opacity values from the OPAL opacity table are used to study the boundary layer of the white dwarfs (Collins et al. 1998). They obtain a very high central temperature near to the white dwarf but on applying the optical depth consistently from the table, they get the same order of magnitude of the effective temperature

$$T_{\rm eff}^4 = \frac{8T^4}{3\tau}$$

as it is on the surface of a typical white dwarf.

In our case, the midplane temperature profile shows that the region very near ($\sim 20\,R_\odot$) is very hot gas of 10^5 K, but to compare with the stellar surface effective temperature ($T_{\rm eff} = 22000$ K for $M = 10$ $M_\odot$) one has to take into account the finite optical depth and then the surface temperature of the disk, plotted in the same figure matches the surface temperature of the star at the very innermost regions. Thus the effective temperature of the disk can be considerably lower than the midplane temperature. The flux from the disk and the star are equated in order to compute the radial distance where the stellar irradiation can affect the disk surface,

$$\frac{L_\star}{4\pi r^2} = \sigma T_{\rm eff}^4 \tag{3.8}$$

where $L_\star$ is the luminosity of the star and σ is the Stefan-Boltzmann constant . We find for a 10 $M_\odot$, the stellar irradiation will have a effect on the surface layers around $\sim$ 30 AU for $\alpha_{\rm v} = 1$.

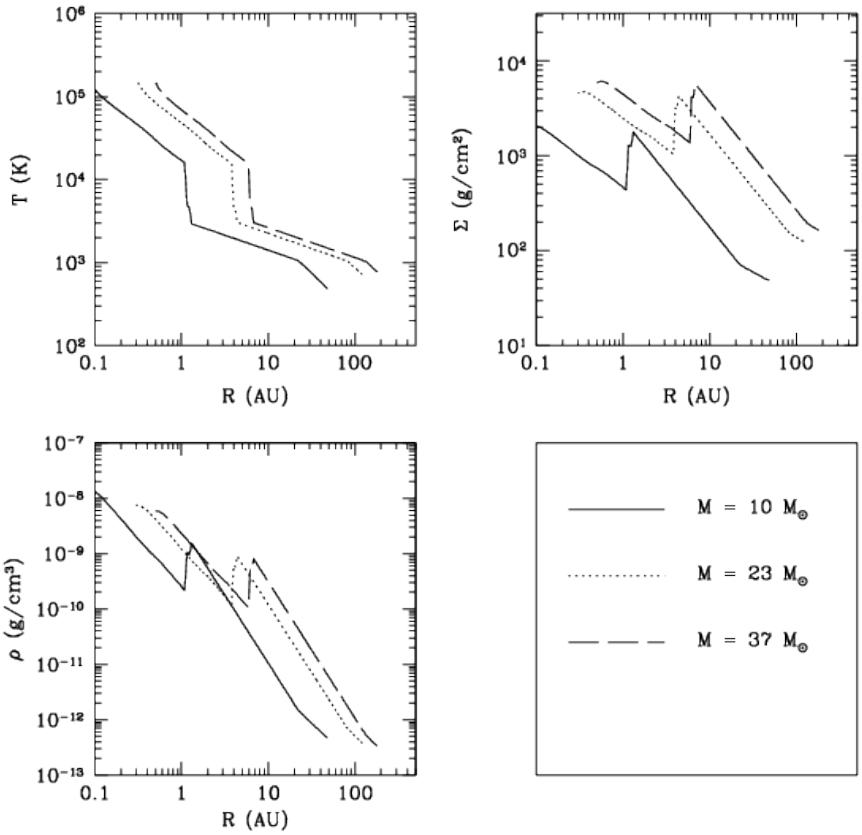

Figure 3.5: Radial profiles of temperature (T), mass density (ρ), surface density (Σ) of the disk extended to the inner region. The *solid line* corresponds to $M = 10\ M_{\odot}$, the *dotted line* for $M = 23\ M_{\odot}$ and the *dashed line* is for central stellar mass $M = 37\ M_{\odot}$.

If the α_v value is lowered, the stellar irradiation can have affect on the surface at even smaller radial distance of around 10 AU. However this effect will not alter the dust sublimation radius in the disk.

3.6 Growth of massive stellar embryo

One of the major problems in the formation of massive stars is the large UV radiation from the protostars that exert pressure on the matter inhibiting the infall on them. This is because as the central mass increases also the central luminosity increases, thus exerting a large radiation pressure which is usually thought to halt the matter falling on the star. In order to get away with the large radiant flux and to form more massive stars, Yorke (2004) lists some of the favorable conditions such as *i*) Reduction of $\kappa_{\rm eff}$ *ii*) Reduction of effective luminosity and *iii*) Increasing the gravitational acceleration.

3.6.1 Reduction of $\kappa_{\rm eff}$ and effective luminosity

In earlier approaches considering the conditions for the formation of massive stars, the matter was thought to be accumulated by spherical accretion (Kahn 1974, Wolfire & Cassinelli 1987). Using detailed dust models and complex grain size distribution, these models were able to put a limit on the maximum stellar mass of 20 $M_\odot$. In general, the dominance of the radiation pressure over gravity of the spherical infall of matter puts a strong constraint on the value of the opacity. In this case, the necessary condition to form a massive star is

$$\frac{\kappa_{\rm eff} L}{4\pi r^2} < \frac{G M_*}{r^2}, \tag{3.9}$$

(e.g. Yorke 2004, Zinnecker & Yorke 2007), which implies an upper limit to the effective opacity,

$$\kappa_{\rm eff} < 130\,{\rm cm^2\,g^{-1}} \left(\frac{M}{10\ M_\odot}\right)\left(\frac{L}{1000\,L_\odot}\right)^{-1} \tag{3.10}$$

In the disk scenario, there would be additional contribution to the forces mentioned in equation (3.9), such as disk gas and ram pressure.

In the present work, we demonstrate that most of dust, due to the self sublimation of accretion disk, is destroyed already at distances larger that $\sim$ 10 AU from the central source which helps to reduce the $\kappa_{\rm eff}$. It is evident that the maximum value of the opacity even in the innermost region of the disk is less than 5 cm^2 g^{-1} (see Fig. 3.4), which is much smaller than the upper limit given by equation (3.10) required for the formation of a typical massive star. This suggests that

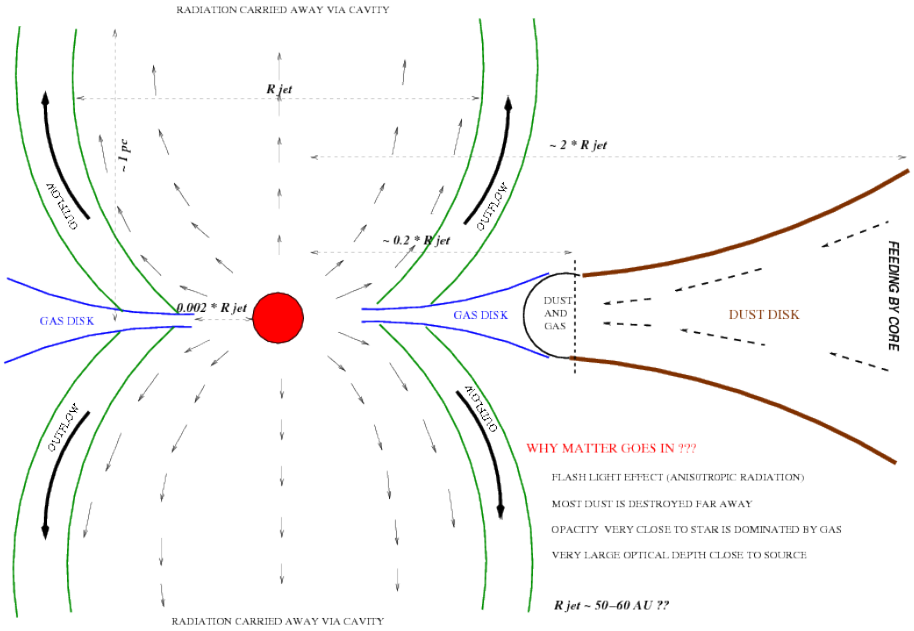

Figure 3.6: Pictorial representation of the inner region of the massive star.

the radiation pressure is no longer inhibiting the accretion process onto to the central star and thus allowing more massive stars to form. This effect is aiding the matter to flow closer to the central object but does not ensure that matter will be accreted on the central star. Thus reduction in opacity is an essential requirement but it does not guarantee growth of mass as the isotropic radiation from the star may still stop the dust by exerting the pressure which is dependent on the luminosity of the central object.

A sketch of our model calculations assuming a 10 $M_{\odot}$ central star is shown in Fig. 3.6. The scaling of the figure is done using a fiducial jet radius. The main components in the figure are the dusty disk which is fed with matter by the core, the inner gaseous disk and the large scale bipolar outflows. The region near to the dust sublimation radius shows the presence of dust and gas and large variation of opacity is seen in this region. Very close to the source there is large flux of UV and visible radiation which is blocked from the midplane of outer dusty disk by the high optical depths ($\tau \gg 1$) of the inner gaseous species. The figure also shows the possibility of radiation flux escaping more in the direction perpendicular to the plane. This *flashlight effect* was introduced by Yorke & Bodenheimer (1999) in order to have anisotropy in the radiation and allow matter to accrete.

3.6.2 Overcoming Radiation Pressure

The reduction of effective opacity and luminosity ensures the matter to come closer to the central star. In the region very near to the star matter is subjected to different pressure sources, all of them play an important role in understanding the dynamics of disk accretion under the influence of stellar radiation pressure. We therefore compare the contribution of different pressure sources, considering typically a 10 $M_\odot$ star.

The *radiation pressure from the star* is a function of the radial distance from the surface of the star,

$$P_{\mathrm{rad},\star}(r) = \frac{L_\star}{4\pi c r^2} = 5.9 \times 10^2 \,\mathrm{erg\,cm^{-2}} \left(\frac{T_{\mathrm{eff}}}{22000\,\mathrm{K}}\right)^4 \left(\frac{r}{\mathrm{R}_\star}\right)^{-2} \tag{3.11}$$

The *ram pressure from the disk* counteracts the radiation force from star and will allow the matter to accrete. We estimate the ram pressure $P_{\mathrm{ram}} = \rho v_{\mathrm{r}}^2$ using our consistent dust and gas opacity model (see Sect. 3.3 and Sect. 3.5),

$$P_{\mathrm{ram}}(r) = 2.08 \times 10^3 \,\mathrm{erg\,cm^{-2}} \left(\frac{\rho}{2.32 \times 10^{-9}\,\mathrm{g\,cm^{-3}}}\right)^{-1} \left(\frac{\dot{\mathrm{M}}}{10^{-4}\ \mathrm{M}_\odot\,\mathrm{yr}^{-1}}\right)^2 \left(\frac{M}{10\ \mathrm{M}_\odot}\right)\left(\frac{T}{5.03 \times 10^4\,\mathrm{K}}\right)^{-1} \left(\frac{\mathrm{R}_\star}{6\,\mathrm{R}_\odot}\right)^{-5} \left(\frac{r}{10\,\mathrm{R}_\star}\right)^{-5} \tag{3.12}$$

Figure 3.7 shows the radial profiles of both pressure sources. The figure clearly depicts that the radiation pressure from the star is much below the ram pressure in the disk which will aid the matter to overcome radiation pressure and accrete on the central star. In the very inner region of the disk, the disk radiation pressure becomes comparable to the gas pressure in the disk which may result in thermal instability (Fig. 3.7).

3.7 Stability of Disks

The disks around massive stars can be unstable due to axisymmetric gravitational instability. They can also be unstable due to fragmentation due to rapid cooling of the disk as compared to the dynamical time scale.(Gammie 2001, Rice et al. 2003, Rafikov 2005). We will also see that these disks can be also unstable thermally in the very inner region, close to the massive star.

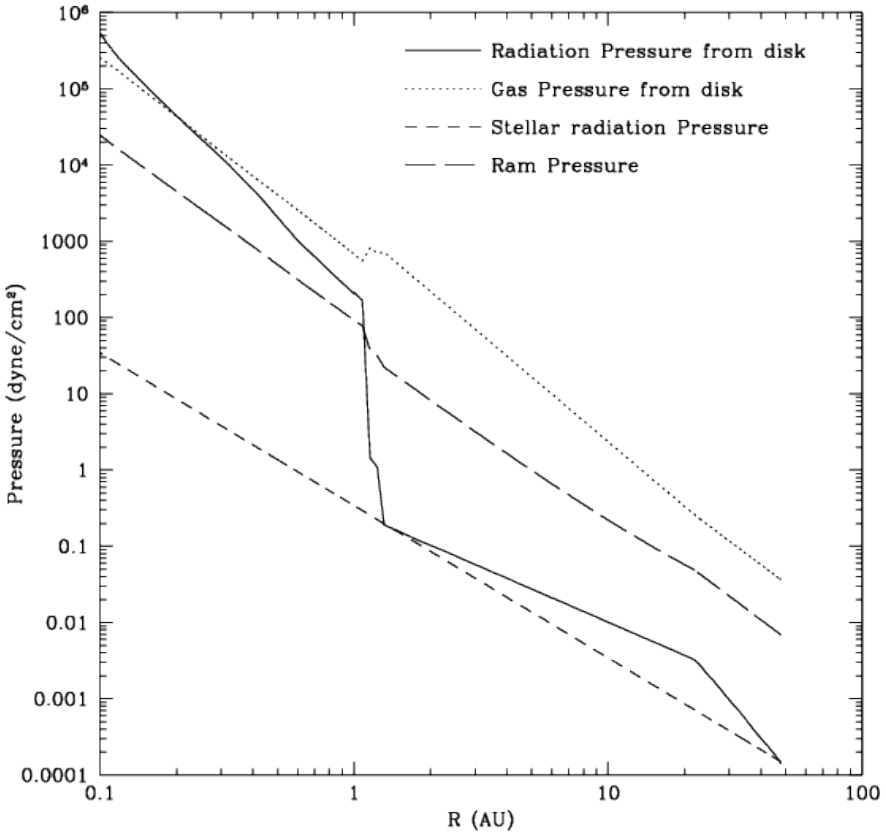

Figure 3.7: The above figure compares the pressure due to different sources in the circumstellar environment for a 10 $M_{\odot}$ star

.

3.7.1 Gravitational Instability

The criterion for the gravitational instability of a disk is given by the Toomre parameter

$$Q = \frac{c_s \Omega}{2\pi G \Sigma}$$

with Ω as the Keplerian angular velocity and Σ as the surface density of the disk (Toomre 1964). For $Q > 1$ the disk is stable (no fragmentation), while $Q < 1$ leads to instability in the disk. Physically, the Toomre parameter can be considered as the ratio of centrifugal force along the radial direction to the gravitational force acting in the direction perpendicular to the radial motion. Thus, if a local accumulation of mass is moving in a certain orbit, then this would lead to slowing down of orbital motion and also more gravitational force acting downward which implies that the value Q will decrease and eventually when $Q < 1$ the downward gravity force wins and leads to instability generating over dense regions. [c]

It has been known from simulations (Krumholz et al. 2007, Krumholz et al. 2009) and observations in case of G 192.16-3.82 (Shepherd et al. 2001, considering large observational errors) that disks in massive stars are unstable as they may have Q value low and sometimes < 1 for some radial extent.

The Toomre parameter decreases with the radial distance, and at some radial distance and the disk becomes gravitational instable. Figure 3.4 shows the radial behavior of the Toomre parameter in case of typical disk parameters ($\dot{M} = 4.2 \times 10^{-4}$ $M_\odot\,yr^{-1}$, stellar mass $M = 10$ $M_\odot$ and $\alpha_v \sim 1$). It is clear that such a disk is unstable as $Q < 1$ after ~ 100 AU.

3.7.2 Fragmentation of Disks

Disks which are stable for axisymmetric gravitational instability may not be necessarily stable for fragmentation which leads to formation of bound objects. Gravitational instability sets an upper limit of the sound speed where as the analysis for fragmentation and cooling time sets a lower limit on the speed of sound in the disk (Rafikov 2005).

Numerical simulations (Gammie 2001, Rice et al. 2003) and analytical solutions (Rafikov 2005) suggest that for a disk to avoid fragmentation, the cooling time scale should be larger than the dynamical timescale ($t_{dyn} \sim \Omega^{-1}$). The threshold relation of the cooling time can be obtained, $\Omega t_{cool} < \zeta$, where the factor $\zeta \approx 3$, as obtained from simulations using constant t_{cool} (Gammie 2001, Rice et al. 2003). For the present purpose, we apply cooling time as given by Rafikov

[c]The Toomre criteria can be written as a product of two ratios - $\frac{E_{thermal}}{E_{grav}} \frac{E_{rot}}{E_{grav}} < 1$. If only one of the ratios is less than unity, that will not guarantee that fragmentation will occur (see Sect. 3.7.2).

(2005),

$$t_{\rm cool} \approx \frac{\Sigma c_s^2}{\gamma - 1} \frac{f(\tau)}{2\sigma T^4} \tag{3.13}$$

where $f(\tau) = \tau + \frac{1}{\tau}$ describes the efficiency of cooling and depends on the optical depth τ. In the above equation (3.13), γ is the adiabatic index and factor $\gamma - 1$ considered to be of the order of unity (Rafikov 2005).

The variation of the cooling time, as given by equation (3.13), with radial distance is shown in Fig. 3.4 for different values of $\alpha_{\rm v}$. These curves are made applying the Bell & Lin opacity power laws. The *solid line* in the figure for cooling time determines the threshold for fragmentation to set in. The relation suggests that a value $\alpha_{\rm v} \sim 1$ would lead to a disk which may fragment completely. However, the lower values of $\alpha_{\rm v} \sim 0.1, 0.01$ would enable a stable disk against fragmentation. The value $\alpha_{\rm v} \sim 0.1$ is consistent with that obtained by observational modeling of ionized disks (King et al. 2007).

3.7.3 Thermal Instability

Thin accretion disks around black holes which are supported by radiation pressure (region A, See Sect. 2.3.1 in Chapter 2) were found to be thermally instable (Shakura & Sunyaev 1976). The physical reason for such kind of instability is inefficient cooling in the disk as compared to the viscous heating. This leads to overheating which causes expansion which in turn overheats the disk eventually leading to a thermal runaway. There were ideas of application of slim disk model to this region, which is a stable branch in the S-shaped $\dot{\rm M} - \Sigma$ curve, because such a model prevents the radiation to escape from the disk and allowing the flux to be advected along with the flow of matter (Abramowicz et al. 1988).

In the modeling of the disk around massive star, we see that the radiation pressure becomes comparable to the gas pressure in the very innermost region of the disk $\leq 4R_\star$ for a 10 $\rm M_\odot$ star. Here the assumption that $P_{\rm gas} > P_{\rm rad}$ no longer holds, and we stop our iterations at this radii. However, the application of concept of slim disk in protostellar disks for efficient cooling is not really probable. This is because of the fact that advected flux should get rid in some manner, it is viable in disks around black holes as the flux can be advected into the black holes, however in case of disks around stars this flux will heat up the star, which may be not physical. Turner et al. (2007) applied the concept of photon bubble instabilities to the young massive stellar environments, which could be an efficient way of cooling the innermost region of massive star forming region as well.

3.7.4 How big is α_v?

The value of α_v parameterizes the viscosity in the disk. In the present case, we see that higher value of $\alpha_v \sim 1$ ensures that the disk within $\sim$ 100 AU is stable to axisymmetric gravitational instability, though for this high value of α_v , the disk completely would fragment.

For $\alpha_v \sim 0.1$ the disk would become stable to fragmentation. In this case, the part of the disk stable to axisymmetric gravitational instability reduces to $\leq 80 - 90$ AU

For $\alpha_v = 0.01$, the disk would again be stable to fragmentation, but now most part of the disk is subjected gravitational instability. The effect of lowering the value α_v on the Toomre parameter can be seen in Fig. 3.4

The value of α_v is usually chosen as a parameter in disk modeling for different purposes. In case of low mass stars, the range of α_v values accepted is around 0.001-0.01, which is believed to be produced by magneto-rotational instability (Balbus & Hawley 1998). In case of massive stars, the value of α_v can be higher by one order of magnitude and the physics involved to generate this high α_v value could be different from that seen in low stellar mass case. (for e.g. Gravitational instability)

A high α_v would imply that matter flows radially with high speed near to local sound speed and there could be a possibility of accretion shocks produced to make the radial speed of matter subsonic. These accretion shocks have been proposed for the close circumstellar environments of high mass protostar such as CRL 2136 with the H_2O maser (Menten & van der Tak 2004).

The other way of treating viscosity in the disk would be by assuming a radial profile, $\alpha_v(r)$, such that its value may be high ($\sim$ 1) in the outer region and lower($\sim$ 0.1) in the inner region of the disk. Such a radial profile would then lead to fragmentation resulting in formation of bound objects influencing the structure in the outer part of the disk around most massive star formed such that each bound object may form itself a low mass or even high mass star (Krumholz et al. 2009). However, the inner ionized disk can be still stable and can launch large scale bipolar outflows.

In Fig. 3.8, variation of the dynamical quantities obtained from the present model for a 10 $M_\odot$ star with two different values of α_v is shown. Apart from changing the α_v value we also change the value of mass accretion rate according to the Fig. 3.2. There is no considerable change in midplane temperature profile, which is due to the fact that by changing two parameters also bring change in the opacity and the cumulative effect cancels the variation in temperature [d]. However, this does not happen for mass density as the dependence on the above variations is different.

[d]Note that Σ is inversely proportional to α_v and decreasing the α_v will increase density and thus opacity

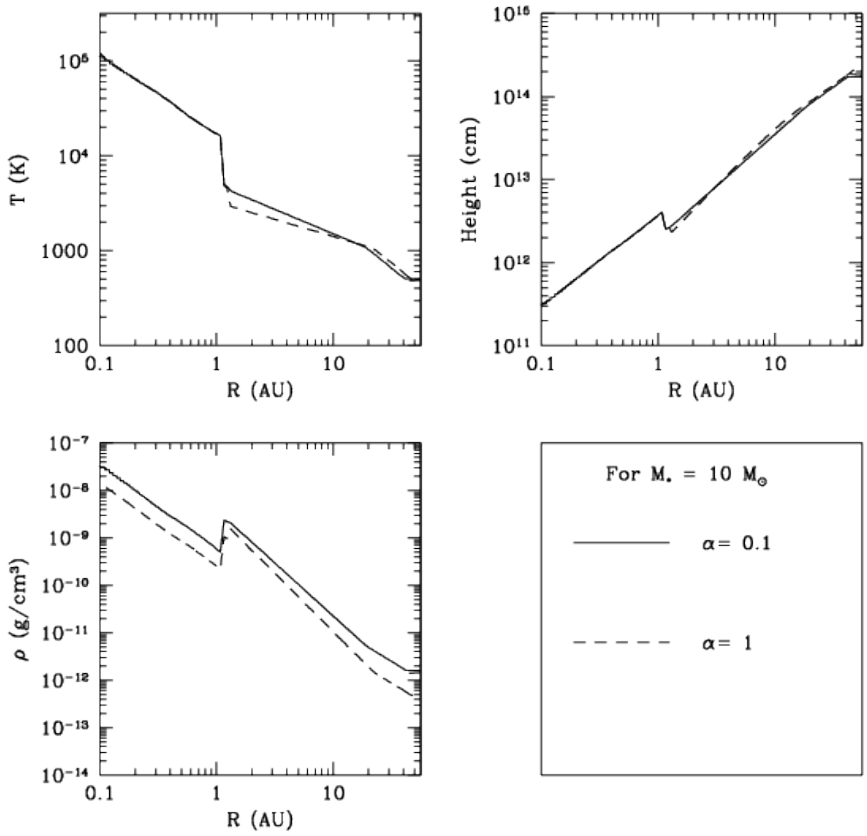

Figure 3.8: Dynamical quantities for two different α_v values. The *solid line* represents plot with $\alpha_v = 0.1$ and $\dot{M} = 10^{-4}$ $M_\odot$ yr^{-1} where as *dashed line* is for $\alpha_v = 1$ and $\dot{M} = 4.2 \times 10^{-4}$ $M_\odot$ yr^{-1}

Since the height depends only on the temperature, the height profile also does not show any variation.

3.8 Implications for Observations

Early stages of massive star formation are difficult to observe, as the whole process is enclosed in an envelope of dust. Also these high mass star forming regions are at a distance of few kilo parsecs which makes the observation more difficult due to limited resolution of the present day telescopes.

One of the essential findings of the present work is the high temperature of the order of $\sim 10^5$ K in the inner disk. At such a high temperature, the opacity is mostly dominated by electron scattering

and there is a pool of highly energetic electrons present close to the massive star. These electrons might be responsible for soft X-ray emissions from massive young stars.

There have been observations of X-rays in some of the massive young sources in the W3 complex (Hofner et al. 2002) and also in GGD 27 (Pravdo et al. 2009). In the case of GGD 27, observed hard X-rays emissions have energies of the order of 2-10 KeV. The temperatures obtained from present work indicate emissions of soft X-rays, however the soft X-rays emissions have a large extinction in massive star forming regions. There might be possibility that these less energetic electrons are accelerated by magnetic fields giving rise to hard X-ray emission and also the hard X-ray emission may come from shocks produced when the accreted matter falls on the surface of star (Montmerle 2007).

Amidst all the difficulties, observers were successful to resolve a fattened structure having length scales of $\sim$ 1000 AU. The best candidate of showing presence of a rotating Keplerian disk is IRAS 21026 + 4104 (Cesaroni et al. 2005) which is predicted to be early B star (Mass = $7 - 12$ $M_{\odot}$). They estimate the radial profile of mean kinetic temperature for the Keplerian disk and mass density profile using different lines. They obtain the best fit for temperature profile as $T(R) \propto R^{-q}$ where q is 0.57-0.75 and that of mass density $\rho(R) = R^{-2.1}$ for HCO^{+} (1-0) line. The values of the powers obtained are very close to the best fit of these profiles from the present model (Fig. 3.1). Schreyer et al. (2006) also were able to resolve a rotating structure in an embedded $8 - 10$ $M_{\odot}$ massive star AFGL 490. They also obtain a Keplerian profile for the rotational velocity and the best fit radial power law for the surface density was $\Sigma \propto R^{-1.5}$, which is close to the value obtained from the present model ($\Sigma \propto R^{-1.1}$). In case of low mass stars, usually the density in the disk is fitted using the gaussian as given by (Whitney et al. 2003,Wolf et al. 2008)

$$\rho_{\rm disk} = \rho_0 \left(\frac{R_*}{r}\right)^a \exp\left\{\frac{-1}{2}\left[\frac{\rm z}{\rm h(r)}\right]^2\right\} \tag{3.14}$$

where the scale height has the radial dependence of the form

$$h(r) = h_0 \left(\frac{r}{R_*}\right)^b \tag{3.15}$$

The best fit obtained for the case of disks in Butterfly star was a=2.35, b=1.28 (Wolf et al. 2008). These results are interesting as similar radial fits to the elongated continuum are obtained even for the recent observational results of young high mass source IRAS 18151-1208 (Fallscheer private communication). Also similar fits are obtained from the present model.

3.9 Conclusion : 1D disk model

We have presented global models for accretion disks around massive young stars.

We have solved the thin disk equations taking into account the proper opacities for dust and gas. In particular we consider Rosseland mean dust opacities given by Ruden & Pollack (1991) and the gas opacities from the OPAL opacity tables (Iglesias & Rogers 1996).

This enables us to provide the dynamical quantities of disk accretion from the very inner part at radii of 0.1 AU to the outer region of the disk at about 100 AU. At the same time this provides a theoretical link between outer disk which is accessible in principle by observations and the inner disk which is not yet possible to resolve observationally.

Our main results can be summarized as follows.

1. For typical stellar masses and accretion rates we find very high midplane temperatures of the order of 10^5 K for radii less than $\sim$ 0.1 AU
2. Due to the high disk temperatures the dust sublimates already at distances which are about a factor three larger than caused by the stellar irradiation. This *disk self-sublimation* lowers the disk opacities considerably and allows for disk accretion in the stellar radiation field.
3. We estimate the stability of these disk by the Toomre criterion and find that our thin disks around e.g. a 10 $M_\odot$ star becomes gravitationally unstable beyond 100 AU. We also see for α_v values close to 1, the disk would fragment completely whereas for $\alpha_v \sim 0.1$ the disk could remain stable to fragmentation. We also discuss the effect on the dynamics and stability of the disk model with the variation of α_v.
4. For the given disk and stellar parameters and disk opacities we find that the stellar radiation pressure is negligible against the disk ram pressure and gas pressure and therefore cannot hinder accretion towards a massive young star.

Considering the high disk temperatures and the rather large disk viscosity parameter, disk around massive young stars seem to be intrinsically different from the low mass equivalents in particular to the different form of disk opacity

We also find that for higher mass stars with high accretion rates the dust sublimates further away and obtain much higher temperature for the same. The presence of the optically thick gaseous component and anisotropy of radiation prevents the matter to be unaffected by the radiation from the star.

Minds are like parachutes.
They only function when they are open

Sir James Dewar (1842-1923)

4

Jet formation around massive YSO : MHD and Radiative modeling

This chapter is based on a paper submitted by Bhargav Vaidya, Christian Fendt, Henrik Beuther & Oliver Porth titled - Jet formation from massive young stars: Magnetohydrodynamics versus radiation pressure (Vaidya et al. 2011). It has been accepted for publication in the Astrophysical Journal.

Massive young stars exhibit large-scale molecular outflows and collimated jets. Observations indicate that these outflows are more collimated during the early stellar evolution than in later stages. This chapter aims to investigate all the physical processes that impact the dynamical evolution of the outflow, i.e. its acceleration and collimation. We perform axisymmetric MHD simulations considering in particular the radiation pressure exerted by the star and the disk. We apply the ideal MHD code PLUTO which we have modified to include radiative forces in the line-driving approximation after Castor, Abbott & Klein. We launch the outflow from the innermost disk region ($r < 50$ AU) by magneto-centrifugal acceleration. In order to disentangle the MHD effects from radiative forces, we start the simulation in pure MHD, and then later switch on the radiation. We perform a parameter study considering different stellar masses (thus luminosity), magnetic flux, and line-force strength. For our reference simulation - assuming a 30 $M_\odot$ star, an initial maximum disk magnetic field of 5.1 G, and a line-force parameter $\alpha = 0.55$ - we find substantial de-collimation of 35% due to radiation forces. The outflow opening angle increases from 20° to 32° for stellar masses from 20 $M_\odot$ to 60 $M_\odot$, respectively. The line-force parameter strongly governs the strength of the radiative force. A small change of α from 0.60 to 0.55 changes the opening angle by $\sim 8°$. Our simulations also show that radiative forces can affect the launching conditions resulting in an increased mass flux by 16%. We find that it is mainly the stellar radiation force which could affect the jet dynamics. Unless the disk extends to radii very close to the stellar surface the disk luminosity is too small to have much impact. On the other hand, the stellar radiation field significantly affects the collimation, and acceleration of the

outflow. Essentially, our parameter runs with different stellar mass can be understood as a proxy for the time evolution of the star-outflow system. Thus, we have shown that when the stellar mass (thus luminosity) increases (with age), the outflows become less collimated.

4.1 Introduction

Outflows and jets are integral processes of star formation. They are believed to be essential for the angular momentum evolution of the cloud core and the protostar - either directly as stellar winds or indirectly by changing the structure and the evolution of the surrounding accretion disk. Also, outflows from young stars provide an important feedback mechanism to return mass and energy into the ambient medium from which the young star is born.

The standard framework for the launching process of jets or outflows from low-mass protostars (and most probably also for extragalactic jets) is the model of a disk wind accelerated and collimated by magneto-centrifugal and magnetohydrodynamic forces (Blandford & Payne 1982, Pudritz et al. 2007). A number of numerical simulations of jet formation have been performed which all confirm this picture of self-collimated MHD jets for low mass stars (Ouyed & Pudritz 1997, Krasnopolsky et al. 1999, Fendt & Čemeljić 2002, Ouyed et al. 2003, Fendt 2006, Fendt 2009). Its applicability has also been demonstrated for the case of extragalactic jets (e.g.Komissarov et al. 2007, Porth & Fendt 2010).

Various multi-wavelength studies suggest that outflows are an ubiquitous phenomenon not only for low-mass stars, but also in massive star forming regions (Beuther et al. 2002a, Stanke et al. 2002, Zhang et al. 2005, López-Sepulcre et al. 2009, López-Sepulcre et al. 2010, Torrelles et al. 2011). An evolutionary picture for high-mass outflows was proposed by Beuther & Shepherd (2005) (see Sect. 1.4). In view of this picture, jet formation starts with similar MHD acceleration processes compared to the low-mass models during the earliest evolutionary stages. Later, other physical processes could play a role, for example, the radiation from central star or more turbulence at the base of the jet. The interaction of these processes is expected to lower the degree of collimation.

How the radiation field affects the formation of a jet is not obvious *a priori*. In order to quantify and to disentangle the physical processes involved, a detailed numerical investigation is required. Essentially, stellar (and disk) radiative forces may affect jet acceleration and collimation directly (neglecting ionization, heating, and probably turbulent stirring for simplicity), but also in-directly by changing the physical conditions of the jet launching area, thus governing the mass loading or the initial entropy of the ejected jet material. For example, numerical MHD simulations have shown that jets with higher (turbulent) magnetic diffusivity are expected to be substantially less

collimated (Fendt & Čemeljić 2002).

Our previous studies (Vaidya et al. 2009) have shown that the inner accretion disk around massive protostars is ionized, has a high temperature and is gravitationally and thermally sufficiently stable in order to provide a suitable launching area for an outflow. Together with the recent observations of magnetic fields around high mass protostars (e.g Vlemmings 2008, Girart et al. 2009, Vlemmings et al. 2010) , this indeed supports the picture of a scaled-up version of low-mass stellar jet formation.

In this chapter we will present a detailed investigation of how a strong radiation field impacts the structure and dynamics of a magneto-hydrodynamical driven jet. The aim of this work is to give physical basis of the empirical sequence of outflow collimation as put forth by Beuther & Shepherd (2005) (see Sect. 1.4). Motivated by the presence of strong jets and outflows in massive star formation, we apply the standard picture of MHD jet formation known for astrophysical jets and put it in the physical environment of a massive young star.

4.2 Model setup: Jet formation from massive young stars

In this section we discuss the model setup applied for our numerical study concerning the formation of jets and outflows from massive young stars. The central point is that we are going to consider the main features of the *standard model* of MHD jet formation which is well established for low-mass young stars or Active Galactic Nuclei also for high-mass young stars. Our model consists of the following essential ingredients (see Fig. 4.1).

- A central massive young star which is rapidly evolving in mass M_*, luminosity L_*, and radius R_*.
- A surrounding accretion disk with high accretion rate, estimated to be of the order of $\dot{M} \simeq 10^{-3}\ \mathrm{M_\odot\,yr^{-1}}$.
- A jet launching inner accretion disk. The extension of this area towards the star is not known and may depend on the existence of a strong stellar magnetic field and stellar radiation pressure. Instead of introducing an inner disk radius $R_{\mathrm{in,disk}}$, we will refer to an inner jet launching radius $R_{\mathrm{in,jet}}$, which we presume to be between 0.1 and 1.0 AU, and to which the length scale of the simulation will be normalized $l_0 = R_{\mathrm{in,jet}}$.
- A magnetic field around the protostellar object. Magnetic fields are essential for generating collimated high-speed outflows. Observational indication for such fields around high-mass protostars exists.

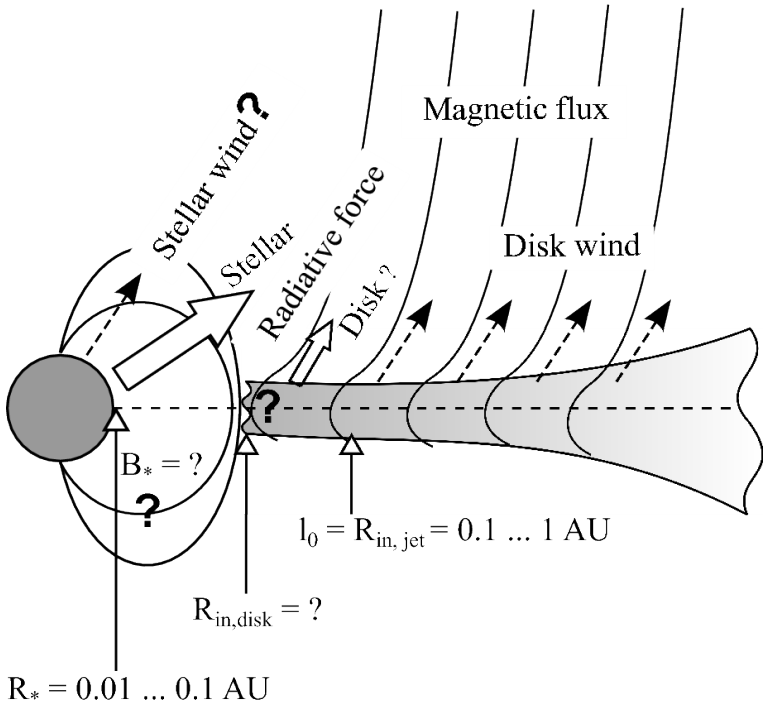

Figure 4.1: Sketch showing our model setup of inner regions around a massive young star. Several constituents are considered: The disk outflow (*dashed arrows*) is launched along the magnetic flux surfaces. The inner most launching point is denoted by $R_{\rm in,jet}$. This outflow is subject to radiation forces (*white arrow*) from the star and (potentially) from an inner hot accretion disk. The stellar radius R_*, could be as large as $\sim$ 100 $R_\odot$, while the stellar magnetic field structure and strength B_* is rather uncertain. The location of an inner disk radius $R_{\rm in,disk}$ (if existent) is also not known.

- A strong radiation field of the high-mass young star which may influence accretion and ejection processes. In case when the accretion disk reaches down to radii close to the stellar surface (no gap as in case of low mass stars), also the high disk luminosity may play a role for the outflow dynamics.

In the following we briefly discuss the observational and theoretical background of these constituents and finally mention the limits of our model and possible model extensions (a more detailed discussion is provided before the summary).

4.2.1 The central massive young star

It has been proposed that outflows from massive young stars may follow an evolutionary sequence such that outflows tend to be more collimated and similar to jets from low-mass stars in the early stages of stellar evolution, whereas at later times the outflows are less collimated

(Beuther & Shepherd 2005). Since this intrinsically corresponds to an evolutionary sequence in stellar mass, we have investigated simulations with different central mass, ranging from 20 $M_\odot$ to 60 $M_\odot$.

A higher stellar mass automatically gives rise to a faster outflow (supposed the relative launching radius is the same), just because the outflow originates deeper in the gravitational well.

4.2.2 The accretion disk and the jet launching area

Jets from low mass stars are thought to be launched from less than 1 AU of the inner accretion disk (e.g. Anderson et al. 2003, Ray et al. 2007). In T Tauri stars, these regions could be well studied via NIR interferometry (e.g. Akeson et al. 2000, Akeson et al. 2005, Dullemond & Monnier 2010). However, to probe regions ≤ 100 AU around a young high-mass star is difficult due to the large extinction. We had therefore studied this region via semi-analytic modeling in a previous paper (Vaidya et al. 2009) to get handle on the physical properties of such disks. We have shown that here the disk may reach high temperatures $\sim 10^5$ K leading to sublimation of most of the dust and ionizing the bulk of the material.

The inner disk radius in case of low mass stars is usually estimated assuming magnetic pressure balance with the accretion ram pressure. Typical values are $\sim 3 - 5\ R_\star$. For young massive stars, such an estimate is not possible due to lack of knowledge on stellar magnetic fields during the formation stage. In addition, radiative force from the bright luminous massive star could also influence dynamics of the inner disk. Although our semi-analytic modeling indicated that the disk could extend right down to the central star, detailed 3 D models with accurate radiative treatment are required to get more insight in these close-by regions (Vaidya et al. *in prep*).

We have chosen the inner launching point at a distance of $l_0 = 1$ AU from the star (i.e. similar to low mass stars). A value of $l_0 < 0.1$ AU would imply a high rotation speed and a deep potential well, resulting in a faster outflow. At the same time the jet launching part of the disk would be much hotter and possibly result in a higher contribution to the radiation force from these hot inner parts. On the other extreme, large jet launching radii $l_0 > 10$ AU will result in slow outflows, barely affected by stellar and disk radiation forces.

The density ρ_0 at the inner launching point is used for a physical scaling. We estimate ρ_0 from the observed mass fluxes, which are typically of the order of $10^{-3} - 10^{-5}\ M_\odot\,yr^{-1}$, providing $\rho_0 \simeq 10^{-13} - 10^{-15}\ g\,cm^{-3}$ (Sect. 4.5.3).

4.2.3 The magnetic field

For many years the role of magnetic fields in massive star formation was not really known. However, recent observations have detected relatively strong magnetic fields in massive star forming regions (Vlemmings 2008). Polarimetric observations of the hot massive molecular core HMC G31.41 have revealed a large-scale hourglass-shaped magnetic field configuration (Girart et al. 2009). Beuther et al. (2010) detected a magnetic field aligned with the molecular outflow via polarimetric CO emission. Further observations have detected synchrotron emission from the proto-stellar jet HH 80-81, indicating a ~ 0.2 mG magnetic field in the jet knots while the stellar mass of ~ 10 $M_\odot$ is in the range of massive stars (Carrasco-González et al. 2010).

Vlemmings et al. (2010) have measured magnetic field strengths using polarization by 6.7 GHz methanol masers around the massive protostar Cepheus A HW2 and derive a line of sight (l.o.s) magnetic field strength ~ 23 mG at a distance of 300-500 AU from the central star. The magnetic field strength is parametrized by the plasma beta, β_0, which is the ratio of the thermal gas pressure to the magnetic pressure at the inner launching point l_0. Our simulations are so far limited to $1 < \beta_0 < 10$ by numerical and physical reasons. This translates into field strengths at 1 AU of $\sim$ 100 times weaker than estimated by conserving magnetic flux using observed values at 300 AU.

Note that it is not only the field strength but also the field *distribution* which affects the jet formation process, as it was shown by (Fendt 2006) by MHD jet formation considering a wide parameter set of magnetic field and mass flux distribution along the jet launching area. As a result, simulations applying a concentrated magnetic flux profile tend to be less collimated. We apply as initial field distribution the standard potential field suggested by Ouyed & Pudritz (1997) (Sect. 4.4.2). A central stellar dipolar field (see Fig. 4.1) is not (yet) supported by observations.

4.2.4 The stellar and disk luminosity

The massive young star produces a substantial luminosity, which is supposed to dynamically change the outflow structure. The dependence of the radiation force on the stellar luminosity is parametrized by the Eddington ratio Γ_e, defined as the ratio of the radiation force due to electron scattering to the central gravity (see Table 4.1). The characteristic values of this dimensionless parameter are obtained from the stellar evolution model of Hosokawa & Omukai (2009). In order to study the impact of radiation forces on the dynamics of outflows, we first launch a collimated jet from a disk wind via MHD forces. Then, after the pure MHD jet has achieved a steady state, we initiate the radiation forces, and then compare their impact on the MHD jet. Also, simulations in which the radiation forces are considered from the beginning (which are computationally much more expensive) end up with a final structure of the outflow similar to the one obtained from the

step-by-step method.

We prescribe the radiation force by the line-driving mechanism introduced by Castor, Abbott, & Klein (CAK). Such a force is parameterized by two physical parameters k and α. The value of k is proportional to the total number of lines. The quantity α can be considered as a measure for the ratio of acceleration from optically thick lines to the total acceleration (Puls et al. 2000). Depending on the selection of lines, for massive OB stars typical values obtained for k range from 0.4-0.6, while α ranges between 0.3 and 0.7 (Abbott 1982). The process of line driving has also been applied to cataclysmic variables (CVs) (Feldmeier & Shlosman 1999), as well as to hot and luminous disks around Active Galactic Nuclei (AGN) (Proga et al. 2000, Proga & Kallman 2004).

Proga (2003) carried out numerical simulations driving winds from hot luminous magnetized accretion disks of AGNs, assuming spherical geometry, an isothermal equation of state, and an initially vertical magnetic field structure. Here we consider a potential field which is hour-glass shaped, and an adiabatic equation of state.

4.2.5 Limitations of our model setup

This chapter provides a quantitative study of the interplay between radiative and MHD forces on outflows launched from the vicinity of young massive stars, applying high-resolution axisymmetric numerical simulations. However, a few critical points can be raised which may limit the applicability of our model and which should probably be considered in forthcoming investigations.

From the general point of view there is the lack of true knowledge concerning a number of important parameters as discussed above. One important question is the location of the inner jet launching radius. If it is identical with an inner disk radius - where is that inner disk radius located, if it exists at all? Is there a strong stellar magnetic field which could open up a gap between the stellar surface and the disk as it is known for low-mass young stars?

Further, our disk model is taken as a boundary condition steady in time. As the star evolves, also the disk structure and accretion rate may evolve in time. This question could only be answered by simulations solving also for the disk structure.

Another question is the existence of a stellar wind. We know that OB stars have strong mass loss in form of stellar winds during *later stages* of their life times. The derived mass loss rates are typically of the order of 10^{-6} $M_\odot\,yr^{-1}$. These winds are primarily radiation driven via the line-driving mechanism (e.g. Kudritzki & Puls 2000, Owocki 2009). The velocities derived are high, ranging from $\sim 500 - 1000\,km\,s^{-1}$ and are usually supersonic. However, in case of high-mass

young stars, no indication for such winds has been found so far possibly due to high obscuration. Nevertheless, a future study should implement the physical effect of a central stellar wind.

4.3 Basic equations

For our study, we carry out axisymmetric numerical ideal MHD simulations using the PLUTO code (Mignone et al. 2007). We have modified the original code to incorporate source terms treating the line-driven forces from central star and disk, taking into account self-consistently the density and velocity distribution of the outflow.

The MHD code considers the following set of equations. That is the conservation of the mass, momentum, and energy,

$$\frac{\partial \rho}{\partial t} + (\vec{u} \cdot \nabla)\rho + \rho \nabla \cdot \vec{u} = 0, \tag{4.1}$$

$$\rho(\frac{\partial \vec{u}}{\partial t} + (\vec{u} \cdot \nabla)\vec{u}) = -\nabla P + \frac{1}{4\pi}(\nabla \times \vec{B}) \times \vec{B} - \rho \nabla \Phi + \rho \vec{F}^{\rm rad}, \tag{4.2}$$

$$\frac{\partial}{\partial t}(\rho E) + \nabla \cdot \left[\rho E \vec{u} + (P + \frac{B^2}{8\pi})\vec{u}\right] - \vec{B}(\vec{u} \cdot \vec{B}) = \rho \left[-\nabla \Phi + \vec{F}^{\rm rad}\right] \cdot \vec{u}, \tag{4.3}$$

where ρ is the gas density, $\vec{u}$ the velocity vector, P the gas pressure, and $\vec{B}$ the magnetic field vector with the poloidal and toroidal components $\vec{B}_{\rm p}, B_\phi \hat{\phi}$. In order to include the radiative forces $\vec{F}^{\rm rad}$, the relevant source terms have been added in the momentum and energy conservation equation. The total energy density of the flow E comprises contributions from the internal energy ϵ, the mechanical energy, and the magnetic energy,

$$E = \epsilon + \frac{u^2}{2} + \frac{B^2}{8\pi\rho}. \tag{4.4}$$

The gas pressure in the flow is related to the density assuming an adiabatic equation of state with the adiabatic index γ,

$$P = (\gamma - 1)\rho\epsilon. \tag{4.5}$$

The evolution of the magnetic field is governed by the induction equation,

$$\frac{\partial \vec{B}}{\partial t} = \nabla \times \left(\vec{u} \times \vec{B}\right). \tag{4.6}$$

We treat the ideal MHD equations without considering resistive terms.

In addition to the above set of equations the code obeys the condition of divergence-free magnetic fields, $\nabla \cdot \vec{B} = 0$, using the constraint transport method.

4.3.1 Prescription of radiation forces

We do not explicitly consider radiative transfer, however, we study the effects of momentum transfer by radiative forces on the outflow matter which is launched by MHD processes from the underlying disk. The total radiative force $\vec{F}^{\rm rad}$ comprises of four contributions - the acceleration due to continuum radiation from star $\vec{f}_{\rm cont,*}$ and disk $\vec{f}_{\rm cont,disk}$, respectively, and, similarly, due to spectral lines from star $\vec{f}_{\rm line,*}$ and disk $\vec{f}_{\rm line,disk}$, respectively,

$$\vec{F}^{\rm rad} = \vec{f}_{\rm cont,*} + \vec{f}_{\rm cont,disk} + \vec{f}_{\rm line,*} + \vec{f}_{\rm line,disk}. \tag{4.7}$$

In case of young massive stars, the stellar radiation is sub-Eddington. This immediately implies that the continuum force do not contribute in modifying the dynamics of the MHD outflow as its strength is much below the gravitational pull of the central star. However, line forces could prove to be efficient in substantially enhancing the continuum force by a so-called force multiplier, which is subject to complex theoretical studies of radiative transfer. This theory was developed first by Castor et al. (1975) who solved the radiative transfer equations from spectral lines in moving atmospheres (see Sect. 2.4.3).

The line force due to the central star is a product of the force due to continuum from the star and the force multiplier $M(\mathcal{T})$ (see equation 2.71),

$$\vec{f}_{\rm line,*} = \vec{f}_{\rm cont,*} M(\mathcal{T}). \tag{4.8}$$

The most difficult part for the numerical realization of the line forces is to calculate the proper l.o.s velocity gradients $|\hat{n} \cdot \nabla(\hat{n} \cdot \vec{u})|$ that appears in the formulation of force multiplier (equation 2.71). Following the definition of this term by Rybicki & Hummer (1978), we express this gradient in terms of the rate-of-strain tensor e_{ij},

$$\hat{n} \cdot \nabla(\hat{n} \cdot \vec{u}) = \sum_{i,j} e_{\rm ij} n_{\rm i} n_{\rm j} = \sum_{i,j} \frac{1}{2} \left(\frac{\partial u_{\rm i}}{\partial r_{\rm j}} + \frac{\partial u_{\rm j}}{\partial r_{\rm i}} \right) n_{\rm i} n_{\rm j}, \tag{4.9}$$

where in general $u_{\rm i}$, $r_{\rm i}$, and $n_{\rm i}$ are the components of velocity $\vec{u}$, distance $\vec{r}$, and the unit vector $\hat{n}$, respectively. The different components of this tensor in cylindrical coordinates were calculated from Batchelor (1967). Proga et al. (1998) approximated the above sum to be equal to the most dominant term, corresponding to the radial gradient of flow velocity along the spherical radius. Simulations with a more accurate algorithm of including all the other terms to determine the l.o.s. velocity gradient using the above equation have also been carried out (Proga et al. 1999). These simulations show that the qualitative features of winds are not changed as compared to the approximate calculation of the gradients. Further, they are numerically very expensive. We can approximate that the region of consideration is far away from the star as the central object is a point source. Therefore, the gradient can simply set to be equivalent to dV_R/dR, where R is the

spherical radius and V_R is the gas velocity along the radius R. However, when using cylindrical coordinates instead of spherical coordinates we have to re-write equation (4.9) by transforming R to r, and thereby adding further terms,

$$\hat{n} \cdot \nabla(\hat{n} \cdot \vec{u}) = \frac{1}{1+x^2}\left(\frac{\partial u_r}{\partial r} + x\left(\frac{\partial u_\mathrm{r}}{\partial z} + \frac{\partial u_\mathrm{z}}{\partial r}\right) + x^2\frac{\partial u_\mathrm{z}}{\partial z}\right), \tag{4.10}$$

where $x = z/r$.

We have applied two of the line force components individually as source terms in order to disentangle their effects on the dynamics of a (pure) MHD jet launched from the underlying disk. These two components are from the central star alone and other due to underlying hot accretion disk. Disks around massive young stars accrete very rapidly with rates of 10^{-5} $\mathrm{M_\odot\,yr^{-1}}$ to 10^{-3} $\mathrm{M_\odot\,yr^{-1}}$. Such high accretion rates imply very high accretion luminosities, in particular in their very inner regions. In order to calculate the line forces due to the disk luminosity, proper geometric factors have to be taken into account. We apply a formulation similar to Pereyra et al. (2000). The underlying disk cannot be considered as a point source but rather is an extended cylindrical source of radiation. Further, the disk luminosity varies with the radial distance from the central star. In the present simulations, we consider that the underlying disk as a steady-state standard thin disk with a temperature profile given by Shakura & Sunyaev (1973). Thus, the energy radiated per unit area $D(r)$ at cylindrical radius r is

$$D(r) = \frac{3\dot{M}_\mathrm{acc}GM_*}{8\pi r^3}\left[1 - \left(\frac{l_0}{r}\right)^{1/2}\right], \tag{4.11}$$

where $\dot{M}_\mathrm{acc}$ is the steady-state accretion rate onto a central star of mass M_*. The inner launching radius is l_0. In case of line forces from the accretion disk, we calculate the radial and vertical radiation flux from the standard disk, S_r and S_z (see equations 4.17 and 4.18), similar to Pereyra et al. (2000). Further, the l.o.s. velocity gradient in the force multiplier applied in case of disks is for simplicity reduced to $\partial u_\mathrm{z}/\partial z$, since the bulk of the radiation flux from the disk is in vertical direction,

$$\vec{f}_\mathrm{line,disk} = \frac{\sigma_\mathrm{e}}{c}\left[S_\mathrm{r}\vec{r} + S_\mathrm{z}\vec{z}\right]M(\mathcal{T}). \tag{4.12}$$

Here, S_r and S_z are the radial and vertical flux components. Both depend on the disk luminosity and are implemented in the code in their dimensionless form. (see Sect. 4.4.1).

4.4 Numerical setup

4.4.1 Grid setup & physical scaling

We perform axisymmetric ideal MHD simulations of jet formation in the presence of radiative forces. Our simulations are carried out on a grid of physical size $(r \times z) = (52\, l_0 \times 152\, l_0)$, where l_0 denotes the physical length scale. The grid is divided into (512×1024) cells in radial and vertical direction, respectively. Within $r < l_0$ and $z < l_0$ the grid is uniform with a resolution of $\delta r = \delta z = 0.05$, while for $l_0 < r < 50\, l_0$ or $l_0 < z < 150\, l_0$ the grid is stretched with a ratio of 1.002739 and 1.001915 in radial or vertical direction, respectively. The remaining, very outer part of the grid is again uniform with cell size $\delta r = 0.125$ and $\delta z = 0.20$, respectively.

Figure 4.2 displays the numerical setup used for our simulations. We also show the dynamically important forces that a fluid parcel experiences in an outflow from a young massive star - the gravitational force $\vec{F}_{\rm gravity}$ by the central star, the Lorentz force components parallel $\vec{F}_{\rm Lorentz,\parallel}$ (accelerating) and perpendicular $\vec{F}_{\rm Lorentz,\perp}$ (collimating), the thermal pressure gradient $\vec{F}_{\rm pressure}$, and the centrifugal force $\vec{F}_{\rm centrifugal}$, which plays a vital role in particular for accelerating the flow from the disk surface. The essential point of this chapter is that we also consider radiation forces from the star and the disk ($\vec{F}_{\rm radiation}$, equation 4.7). We consider the most dominant radiative source terms which are those due to the line driving mechanism from the central massive star and the underlying (hot) disk (see Fig. 4.1).

Pure MHD simulations would be scale-free. However, when radiation is considered a physical scaling of the dynamical variables becomes essential. Three scaling parameters in physical units are used – the length scale l_0, the base flow density ρ_0 and the Keplerian velocity u_0, at the inner launching point (see Sect. 4.2 for physical values used for scaling parameters.)

All other quantities can be derived using the following definitions,

$$r_{\rm c} = \frac{r_{\rm cgs}}{l_0}, z_{\rm c} = \frac{z_{\rm cgs}}{l_0}, \rho_{\rm c} = \frac{\rho_{\rm cgs}}{\rho_0}, u_{\rm c} = \frac{u_{\rm cgs}}{u_0}, p_{\rm c} = \frac{p_{\rm cgs}}{\rho_0 u_0^2}, B_{\rm c} = \frac{B_{\rm cgs}}{B_0} = \frac{B_{\rm cgs}}{\sqrt{4\pi\rho_0 u_0^2}}. \tag{4.13}$$

The force multiplier defined in equation (2.71) can be expressed in code units as follows

$$M_{\rm c}(\mathcal{T}_{\rm c}) = \left[\frac{Q_0^{1-\alpha}}{1-\alpha}\left(\frac{u_0}{\sigma_{\rm e} c \rho_0 l_0 \rho_{\rm c}}\left|\frac{du_1}{dl}\right|\right)^{\alpha}\right]. \tag{4.14}$$

Quantities with subscript *'c'* are obtained from simulations in the dimensionless form where as the quantities with subscript *'cgs'* are the ones required in the physical units. We measure the

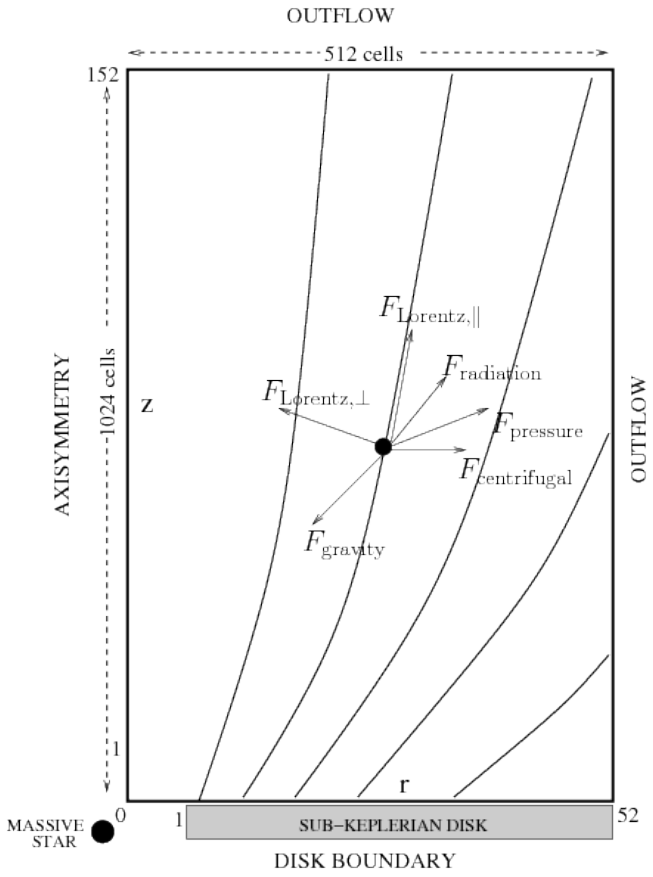

Figure 4.2: Schematic view of the numerical setup along with definition of the boundaries conditions applied for most of the simulation runs. The *lines* indicate poloidal magnetic field lines anchored in the underlying accretion disk which is in slightly sub-Keplerian rotation. The dark *black spot* represents a fluid element frozen onto that field line. Vectors indicate and denote the various forces acting on the fluid element. See text for a detailed description of the different dynamically important forces.

time t_c in units of l_0/u_0. We denote the number of rotations at the inner launching point l_0 as $N_{rot} = l_0/2\pi u_0 = t_c/2\pi$

Using these normalizations the conservation of momentum (equation 4.2) can be written in dimensionless code units,

$$\rho_c\left(\frac{\partial \vec{u}_c}{\partial t_c} + (\vec{u}_c \cdot \nabla_c)\vec{u}_c\right) = \frac{2}{\beta_0}((\nabla_c \times \vec{B}_c) \times \vec{B}_c) - \nabla_c \vec{P}_c - \rho_c \nabla_c \Phi_c + \rho_c(\vec{F}_c^{rad}), \tag{4.15}$$

where the plasma beta, $\beta_0 = (8\pi\rho_0 u_0^2)/B_0^2$, specifies the initial strength of the (poloidal) magnetic field at l_0 and the radiation force

$$\vec{F}_c^{rad} = \frac{\vec{F}_{cgs}^{rad}}{u_0^2/l_0}. \tag{4.16}$$

In case for line driving force due to underlying accretion disk we have S_r and S_z as the radial and vertical components of the flux emitted from the disk surface.(Hachiya et al. 1998, Pereyra et al. 2000) -

$$S_r = \int_0^{2\pi}\int_{l_o}^{end} \frac{D(r')}{\pi} \frac{z^{\alpha+1}(r - r\cos(\phi))}{\left[(r^2 + r'^2 + z^2 - 2rr'\cos(\phi))^{1/2}\right]^{4+\alpha}} r' dr' d\phi, \tag{4.17}$$

$$S_z = \int_0^{2\pi}\int_{l_o}^{end} \frac{D(r')}{\pi} \frac{z^{\alpha+2}}{\left[(r^2 + r'^2 + z^2 - 2rr'\cos(\phi))^{1/2}\right]^{4+\alpha}} r' dr' d\phi, \tag{4.18}$$

where D(r′) is the amount of energy radiated per unit area from the standard thin disk (equation 4.11). In the present simulations, the accretion disk is treated as a boundary and the accretion of matter in the disk is not considered. Thus, the mass accretion rate that appears in the above flux radiative components of the disk has to be prescribed on basis of dimensionless parameters.

$$\dot{M}_{acc} = \frac{4\pi c l_0}{\sigma_e}\Gamma_e \Lambda \mu. \tag{4.19}$$

The radiation flux given above has to be written in dimensionless form to be incorporated in the simulations. These flux components in the code units are given as follows -

$$\begin{pmatrix} S_{r,code} \\ S_{z,code} \end{pmatrix} = \frac{3cGM_*}{2\pi\sigma_e l_0^2}\Gamma_e\Lambda\mu \int_0^{2\pi}\int_{l_0}^{end} \frac{1}{(r'_c)^3}\left(1 - \frac{1}{\sqrt{r'_c}}\right)\begin{pmatrix} \frac{z_c^{\alpha+1}(r_c - r'_c\cos(\phi))}{\left[((r_c)^2+(r'_c)^2+(z_c)^2-2r_c r'_c\cos(\phi))^{1/2}\right]^{4+\alpha}} r'_c dr'_c d\phi \\ \frac{z_c^{\alpha+2}}{\left[((r_c)^2+(r'_c)^2+(z_c)^2-2r_c r'_c\cos(\phi))^{1/2}\right]^{4+\alpha}} r'_c dr'_c d\phi \end{pmatrix} \tag{4.20}$$

Using the above formulations, the dimensionless radial and vertical component of the line force from the disk can then be obtained. Their respective contours are shown in Fig. 4.14.

$$f^{\rm r,code}_{\rm line,disk}(r_{\rm c}, z_{\rm c}) = f^{\rm r}_{\rm line,disk}/(GM_*/l_0^2) = M_{\rm c}(\mathcal{T})S_{\rm r,code}, \tag{4.21}$$

$$f^{\rm z,code}_{\rm line,disk}(r_{\rm c}, z_{\rm c}) = f^{\rm z}_{\rm line,disk}/(GM_*/l_0^2) = M_{\rm c}(\mathcal{T})S_{\rm z,code}. \tag{4.22}$$

The force multiplier for the case of disk force in code units is similar to that used for stellar line force (equation 4.14). However, since we assume that bulk of the photons from the disk move along the vertical z axis, the line of sight velocity gradient is approximated to be just due to vertical velocity,

$$\left|\frac{du_l}{dl}\right| \sim \left|\frac{du_z}{dz}\right|.$$

4.4.2 Initial conditions

We model the launching of the wind from an accretion disk representing the base of the outflow. The gravitational potential Φ is that of point star located at a slight offset $(-r_{\rm g}, -z_{\rm g})$ from the origin to avoid singularity at r=z=0,

$$\Phi(r, z) \propto \left((r + r_{\rm g})^2 + (z + z_{\rm g})^2\right)^{-0.5}, \tag{4.23}$$

where $r_{\rm g} = z_{\rm g} = 0.21$ in all our simulations.

Initially we prescribe a hydrostatic equilibrium with a density distribution

$$\rho(r, z) \propto \left((r + r_{\rm g})^2 + (z + z_{\rm g})^2\right)^{-0.75} \tag{4.24}$$

(Ouyed & Pudritz 1997). The thermal pressure follows an polytropic equation of state $P = K\rho^\gamma$, with $\gamma = 5/3$. The magnitude of $K = (\gamma-1)/\gamma$ is determined by the initial hydrostatic balance between gravity and pressure gradient. To begin with, all velocity components are vanishing. Such an initial setup is typical for jet launching simulations (e.g. Ouyed & Pudritz 1997, Krasnopolsky et al. 1999, Fendt 2006). The initial *hot* hydrostatic distribution of density and temperature does not play a significant role in determining the flow structure as it is eventually washed out by the *cold* [i.e. thermal pressure unimportant] MHD flow that is launched from the base.

The initial magnetic field is purely poloidal (in the (r, z)-plane) with a distribution derived from the potential field $\vec{B}_{\rm p} = \nabla \times A_\phi$ with

$$A_\phi = \frac{\sqrt{r^2 + (z + z_{\rm d})^2} - (z_{\rm d} + z)}{r} \tag{4.25}$$

(Ouyed & Pudritz 1997), where $z_{\rm d}$ is considered as the dimensionless disk thickness. Such a magnetic field configuration is force free. Together with the hydrostatic density distribution this implies an initial setup in force equilibrium. The initial magnetic field strength is prescribed by choice of the plasma-beta β_0 at the inner launching point.

4.4.3 Boundary conditions

To choose the correct physical boundary conditions is of utmost importance for numerical simulations as they describe the astrophysical system under consideration. In the present setup, we have to deal with four boundary regions (see Fig. 4.2).

Axial boundary

Along the jet axis an axisymmetric boundary condition is applied. The normal and the toroidal components of vector fields (i.e. $B_{\rm n}, B_\phi, u_{\rm n}, u_\phi$) change sign across the boundary, whereas the axial components are continuous. The density and the pressure are copied into the ghost zones from the domain.

Equatorial Plane boundary

The disk boundary is divided in two regions - the inner gap region extending from the axis to the inner launching radius, $r < l_0$, and further out the disk region, $r \geq l_0$, from where the outflow is launched.

The setup of this boundary is the most crucial for the outflow simulation. This is an inflow boundary with the boundary values determining the inflow of gas and magnetic flux from the disk surface into the outflow. Special care has to be taken to consider the causal interaction between the gas flow in the domain and in the ghost cells.

In order to have a causally consistent boundary condition (Bogovalov 1997, Krasnopolsky et al. 1999, Porth & Fendt 2010), we impose the four physical quantities $\rho, \Omega^{\rm F}, P, E_\phi$. The toroidal electric field vanishes, $E_\phi = (\vec{u} \times \vec{B})_\phi = 0$, as result of the ideal MHD approximation. Thus, poloidal velocity and the poloidal magnetic field are parallel at the boundary, $\vec{u}_{\rm p} || \vec{B}_{\rm p}$. The angular velocity of the field line (Ferraro's iso-rotation parameter) $\Omega^{\rm F}$, which is one of the conserved quantities along the field line is fixed in time along the boundary. We have chosen a Keplerian profile along the disk $\Omega^{\rm F}(r) \propto r^{-1.5}$. The poloidal velocity at the boundary is *floating*, i.e. copied from the first grid cell into the ghost cell each time step. Thus, the mass flux at the disk boundary

is not fixed but consistently derived by causal interaction between the outflowing gas and the boundary value.

The inner gap region is prescribed as hydrostatic pressure distribution. However, gas pressure gradient, gravity, and centrifugal acceleration is considered for the radial force-balance in the disk, leading to a sub-Keplerian rotation

$$\frac{u_\phi(l_0, 0)}{u_{\rm kep}} = \sqrt{\chi}$$

with $\chi < 1$. Solving for the radial balance delivers the density profile along the boundary

$$\rho_{\rm disk}(r, z) = \left(\frac{1}{1-\chi}\right)\rho(r, z).$$

Therefore, there is a density contrast between disk and initial corona (the domain). In order to avoid numerical problems at the interface of between gap and inner disk (ie. the inner jet launching radius), we smoothen this transition using the Fermi function, considering

$$\chi = \left(\frac{\chi_0}{1 + \exp(-10(r-1))}\right).$$

The Fermi function is resolved by 16 grid cells. We have the launching base to be three times denser than the initial corona so as to have the underlying disk to be cooler.

The magnetic field in the boundary is allowed to evolve in time to avoid any current sheets along the interface. When the simulation starts, the rotating disk winds-up the poloidal field and induces a toroidal field component. Constraining the field line angular velocity $\Omega^{\rm F}$ to be constant in time, we need to adjust the rotational velocity of the gas in the boundary,

$$u_\phi = r\Omega^{\rm F} + \frac{\eta}{\rho}B_\phi, \tag{4.26}$$

where the mass load of a field line $\eta = (\rho u_{\rm p})/B_{\rm p}$ is again a conserved quantity in stationary MHD.

Outflow boundaries

The right and top boundaries (see Fig. 4.2) are defined as outflow boundaries. The canonical outflow conditions (zero gradient across the boundary) are imposed to all scalar quantities and vector components, except for the magnetic field. The toroidal magnetic field component B_ϕ in the boundary is obtained by requiring the gradient of the total electric current I to vanish, whereas the poloidal field components are estimated by setting the toroidal current density j_ϕ to zero (Porth & Fendt 2010). Having this new outflow condition implemented in the standard PLUTO code, we ensure that there is no artificial collimation due to boundary effects.

Table 4.1: Summary of the dimensionless parameters to study the impact of radiation forces on the outflow dynamics

Parameter	Definition
Eddington ratio (proxy for stellar luminosity)	$\Gamma_e \equiv \frac{\sigma_e L_*}{4\pi c G M_*}$
Luminosity ratio (proxy for disk luminosity)	$\mu \equiv \frac{L_{\rm acc}}{L_*} = \frac{G M_* \dot{M}_{\rm acc}}{R_* L_*}$
Radius ratio (proxy for stellar radius)	$\Lambda \equiv \frac{R_*}{l_0}$
Initial plasma beta (proxy for magnetic field strength)	$\beta_0 \equiv \frac{8\pi P_0}{B_0^2}$
Line-force parameters Q_0 and α	prescribes $M(\mathcal{T})$ using equation (2.71)

4.5 Parameter survey

4.5.1 Choice of governing parameters

The three main parameters we apply for a comprehensive study are the (i) central stellar mass M_*, (ii) plasma-beta β_0, and (iii) the line force parameter α (see Table 4.1). We also find that the magnitude of the density at the launching base of the flow ρ_0, which is a free parameter in our simulations, strongly affects the flow characteristics (see discussion in Sect. 4.5.3).

We have performed a large parameter study with respect to the central star. The stellar mass considered in our model ranges from 20 $M_\odot$ to 60 $M_\odot$. The size and the luminosity of these stars are obtained from the literature stellar evolution models (Hosokawa & Omukai 2009). The dimensionless parameter that controls the luminosity of the central star is Γ_e (see Table 4.1).

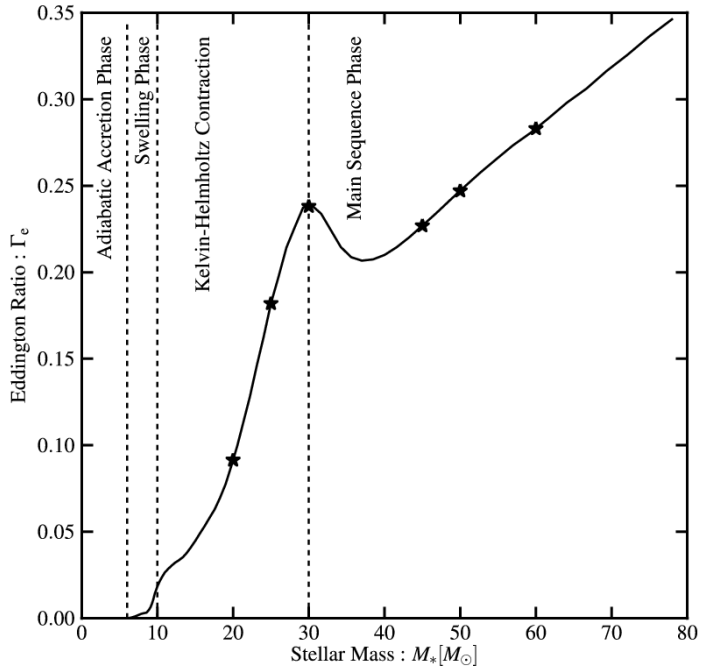

Figure 4.3: Variation of the dimensionless parameter Γ_e with stellar mass M_* from Hosokawa & Omukai (2009). The *solid black line* indicates the stellar mass evolution in the Hosokawa model. *Stars* represent the Eddington ratio Γ_e for different stellar masses in our parameter survey Sect. 4.6.1. The *vertical dashed* lines mark different evolutionary stages for massive young star accreting rapidly at the rate of 10^{-3} $M_\odot\,yr^{-1}$. The curve is obtained using tabulated evolutionary parameters kindly provided by Takashi Hosokawa (private communication).

Its variation with the stellar masses considered in our model is shown in Fig. 4.3. (Also see Sect. 4.6.1)

We have carried out simulations for three different values ($\beta_0 = 1.0, 3.0, 5.0$) of magnetic field strength. We fix the density at the base of the flow to the same value as for the simulations for different stellar mass. Thus, for 30 $M_\odot$ star and an inner jet launching radius of 1 AU, the different β_0 values correspond to a poloidal magnetic field of 11.5 G, 6.6 G, or 5.1 G at the inner launching point, respectively. The detailed description of the different simulations is shown in Table 4.2. The jet is launched by pure MHD processes. As it achieves a steady state after say $N_{\rm MHD}$ inner rotations, we switch on the radiative line forces by the central star and run the simulation for another $N_{\rm RAD}$ inner rotations.

The stellar line force in our model is quantified by the parameters Q_0 and α. In principle, these parameters depend on the degree of ionization in the flow, however, for simplicity, we neglect

this dependence and assume that their values remain the same for a particular simulation run. The line force is independent of Q_0, however, the its dependence on α is strong Gayley (1995). We fix the line strength parameter $Q_0 = 1400$ for all runs. We carry out simulations with three values of $\alpha = 0.55, 0.60, 0.65$. Although the differences in α seems to be small, they lead to considerable variation in the magnitude of the line forces (Gayley 1995). These values of α and Q_0 are consistent with the empirical values obtained for evolved massive stars (Abbott 1982, Gayley 1995). Since, we have no empirical values for these parameters during the formation stage, the present model uses similar values of line force parameters as obtained from evolved massive stars.

4.5.2 Quantifying the degree of collimation

There are in principal several options to quantify the collimation degree of jets. Fendt & Čemeljić (2002) suggested to compare the mass fluxes in radial and vertical direction of the jet as a measure of the jet collimation. However, in general the choice of a *floating* inflow boundary condition and the subsequent time-dependent change of mass fluxes makes it difficult to use them as a measure for the degree of collimation. Therefore, in this work, we quantify the jet collimation by the opening angle ϕ of the field lines (which are equivalent to velocity streamlines in a steady state). For comparison, we measure the opening angle along a certain field line at two critical points along that field line viz. the Alfvén point $\phi_{\rm A}$ and the fast magneto-sonic point $\phi_{\rm F}$. Note that this is not the asymptotic jet opening angle.

In order to estimate the amount of de-collimation $\Delta\zeta[\%]$ by radiation forces, we measure the angular separation of field lines resulting from $N_{\rm MHD}$ disk rotations from those with after $N_{\rm RAD}$ disk rotations,

$$\Delta\zeta[\%](s) = 100\left(\frac{\phi(s, N_{\rm RAD}) - \phi(s, N_{\rm MHD})}{\phi(s, N_{\rm MHD})}\right), \tag{4.27}$$

where s measures of path along the field line. A positive value of $\Delta\zeta[\%]$ implies de-collimation whereas negative values would imply collimation of the jet by radiative forces.

4.5.3 The outflow density at the disk surface - ρ_0

The radiative force term $F_{\rm c}^{\rm rad}$ is a product of the force multiplier and the continuum force. The force multiplier (equation 2.71) depends on the physical scalings u_0, l_0 and ρ_0 (see equation 4.14). This does imply that each simulation run is unique to the chosen set of scaling parameters for a particular type of star.

Table 4.2: Parameter study of stellar radiation line-force effects on MHD disk jets for different field strength and different stellar mass.

Run ID [a]	$M_*[\,\mathrm{M}_\odot]$	β_0	α	ϕ_A [b]	ϕ_F	max[$\Delta\zeta$[%]] [c]	$\dot{M}_\mathrm{vert}[\,\mathrm{M}_\odot\,\mathrm{yr}^{-1}]$ [d]
M30a055b1	30	1.0	0.55	21.98	16.45	5.0	3.1×10^{-5}
M30a055b3	30	3.0	0.55	25.63	20.68	17.0	2.9×10^{-5}
M30a055b5	30	5.0	0.55	26.05	23.40	34.5	2.5×10^{-5}
M30a055b5-c	30	5.0	0.55	25.55	23.01	33.9	2.4×10^{-5}
M20a055b5	20	5.0	0.55	20.44	15.57	5.8	1.6×10^{-5}
M25a055b5	25	5.0	0.55	23.27	19.94	21.9	2.4×10^{-5}
M45a055b5	45	5.0	0.55	26.84	24.35	37.7	3.0×10^{-5}
M50a055b5	50	5.0	0.55	28.86	26.03	42.0	3.3×10^{-5}
M60a055b5	60	5.0	0.55	31.45	29.25	56.0	3.7×10^{-5}
M60a060b5	60	5.0	0.60	23.73	21.48	28.7	3.2×10^{-5}
M60a065b5	60	5.0	0.65	20.93	17.28	11.7	2.9×10^{-5}
M25a055b3inj	25	3.0	0.55	45.84	33.87	30.2	1.3×10^{-5}
M30a055b3inj	30	3.0	0.55	47.71	36.97	37.2	1.4×10^{-5}
M50a055b3inj	50	3.0	0.55	48.76	39.22	42.1	1.8×10^{-5}

[a] We apply the same physical density at the jet base $\rho_0 = 5.0\times10^{-14}\,\mathrm{g\,cm^{-3}}$, the same inner launching radius $l_0 = 1$ AU, and the same line-force parameter $Q_0 = 1400$ for all runs. The simulations are performed for $N_\mathrm{MHD} = 319$ inner rotations in pure MHD, followed by and $N_\mathrm{RAD} = 319$ rotations, with switched-on radiative forces.

[b] A measure for the jet opening angle is given at the MHD critical points, ϕ_A, ϕ_F and along the field line rooted at $r = 5.0\,AU$.

[c] $\Delta\zeta$[%] denotes the percentage difference of the opening angles between the steady-state flows for pure MHD and including radiation force along the field line rooted at the same radius.

[d] The vertical mass flux $\dot{M}_\mathrm{vert}[\,\mathrm{M}_\odot\,\mathrm{yr}^{-1}]$ is measured along the top cells in the domain. The first ten simulation runs in the table apply a "floating" boundary condition for the injection velocity, while for last three runs a fixed-mass-flux boundary condition is applied (see Sect. 4.6.2).

Table 4.3: Parameter study of stellar radiation line-force effects on MHD disk jets for different jet density at the base of the flow with a stellar mass of 30 $M_\odot$.

Run ID [e]	ρ_0[g cm^{-3}]	ϕ_A	ϕ_F	max[$\Delta\zeta$[%]]	$\dot{M}_{vert}$[$M_\odot$ yr^{-1}]
M30a055b5d1	3.0×10^{-14}	30.30	27.79	47.7	1.5×10^{-5}
M30a055b5	5.0×10^{-14}	26.02	23.36	34.5	2.4×10^{-5}
M30a055b5d2	1.0×10^{-13}	22.91	19.47	19.6	4.3×10^{-5}
M30a055b5d3	5.0×10^{-13}	20.42	15.03	4.0	1.9×10^{-4}

[e]For all runs, plasma-$\beta_0 = 5$, $l_0 = 1$ AU and line-force parameters $Q_0 = 1400$ and $\alpha = 0.55$.

In case of massive stars these values are currently difficult to measure very close to the star (see Sect. 4.2). However, observationally derived values of mass flow rates in molecular outflows and jets around massive stars (Beuther et al. 2002b, Zhang et al. 2005, López-Sepulcre et al. 2009) can be used to constrain the densities with prior assumption of inner jet velocity. Typically measured values of the mass outflow rate are of the order of 10^{-3} to 10^{-5} $M_\odot$ yr^{-1}.

The density ρ_0 at the base of the flow ($z \sim 0$) can be estimated by the mass flux launched from the base per unit time,

$$\dot{M}_{out} = 2\pi\rho_0 u_0 l_0^2 \int_{r_{c,min}}^{r_{c,max}} r_c^{1/2-q} dr_c, \tag{4.28}$$

where the density at the base of the flow is $\rho(r_c, z_c = 0) = \rho_0 r_c^{-q}$. From equation (4.24), q = 3/2. We assume the matter is launched from the disk surface with Keplerian speed (i.e. $u_z(r_c, z_c = 0) = u_0 r_c^{-1/2}$). The physical scaling for the density, velocity and lengths are ρ_0, u_0 and l_0 respectively, while r_c is the non-dimensional length unit. Thus, the density scaling ρ_0 can be expressed as

$$\rho_0 = \frac{\dot{M}_{out}}{2\pi u_0 l_0^2} \left[\ln\left(\frac{r_{c,max}}{r_{c,min}}\right) \right]^{-1}. \tag{4.29}$$

Using typical observed mass outflow rates for young massive stellar jets, we calculate $\rho_0 \sim 10^{-13} - 10^{-15}$ g cm^{-3}.

The physical value of the density at the base of the flow is in the denominator of equation (4.14), and therefore affects the magnitude of the line-driving force significantly. Increasing the density by, say, a factor of 10, decreases the line force at least by a factor of 10^α. For the values of α considered her, this magnification could be as large as 3. Such a change in the radiative force has clearly a notable impact on the outflow dynamics, in particular on its degree of collimation. The description of our simulations with different base density is given in Table 4.3.

Table 4.4: Parameter study of disk radiation line-force effects on MHD disk jets.

Run ID [f]	ρ_0[g cm^{-3}]	max[$\Delta\zeta$[%]]	$\dot{M}_{\rm vert}$[M$_\odot$ yr^{-1}]	Comments
Disk1	5.0×10^{-14}	-1.8	6.1×10^{-7}	reaches a steady state
Disk2	5.0×10^{-15}	3.1	7.9×10^{-8}	remains unsteady

[f]All simulation runs apply the same stellar parameters and line-force parameters as M30a055b5, however a different inner launching radius of only 0.1 AU. Additionally, two more dimensionless parameters for the disk radiation force $\mu = 0.4644$ and $\Lambda = 0.4969$ are prescribed (see Table 4.1).

4.6 Results and discussion

The radiation field in massive star forming regions may play a crucial role in modifying the dynamics of outflows and jets. In order to disentangle the effects of radiative forces from the pure MHD jet formation, we decided to follow a two-step approach. We first i) launch a pure MHD disk jet and wait until it has reach a steady state (after about $N_{\rm MHD} = 320$ rotations). We then ii) switch on the radiation line-forces and allow the jet flow to further develop into a new dynamic state. In some cases a new steady-state can be reached, in other cases an unsteady solution develops.

For the radiation forces we consider line-forces exerted by i) the luminous massive young star, and those by ii) the surrounding accretion disk.

4.6.1 Jet de-collimation by the stellar radiation field

The radiation line-force from the central point star is determined by applying equation (4.8). For a detailed physical analysis of the effects of line-forces from the star alone, we have chosen simulation M30a055b5 as reference simulation run (Table 4.2). The reference run is parametrized for a stellar mass of 30 M$_\odot$, surrounded by an accretion disk with an inner jet launching radius of 1 AU, and a density of 5.0×10^{-14} g cm^{-3} at this radius. The initial poloidal magnetic field strength is fixed by a plasma-$\beta_0 = 5.0$. The radiative forces from the star are defined by the line force parameters $Q_0 = 1400.0$ and $\alpha = 0.55$.

The spatial distribution of the force multiplier $M(\mathcal{T})$ as well as the specific stellar line force for the reference simulation are both shown in Fig. 4.4. The magnitude of the force multiplier peaks in the top-right low-density regions of the flow. This is expected as the force multiplier increases with decreasing density as shown in equation (4.8). In order to calculate the true radiation force,

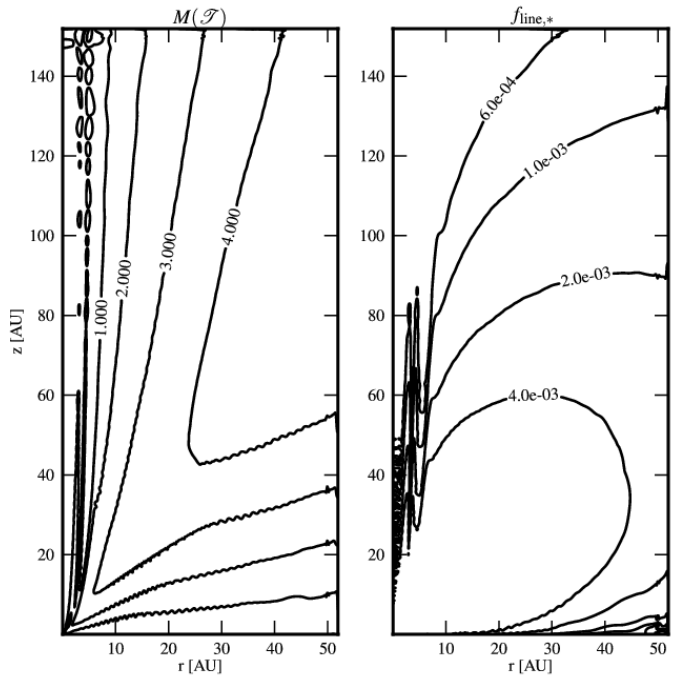

Figure 4.4: Contours of force multiplier M($\mathcal{T}$) and the specific line radiation force of a central star [in physical units] for the reference simulation M30a055b5 after $N_{\rm rot}$ = 638 inner rotations.

the force multiplier must be convolved with the continuum radiation from the star, resulting in a line-force distribution with a maximum close to the central star (see Fig. 4.4).

The time evolution of the emerging jet [g] is shown in Fig. 4.5, where we display the vertical jet velocity $u_z(r, z)$ and the poloidal magnetic field structure for reference simulation M30a055b5. We clearly see the change from the pure MHD flow (*top* panels) to the situation when stellar radiation forces are considered (*bottom* panels).

Material which is injected from the disk surface (*bottom boundary*) is *frozen* on these field lines (ideal MHD). Initially, the plasma is accelerated magneto-centrifugally and gains substantial speed, producing a bow shock as it propagates. The bow shock leaves the domain after $\sim$ 60 rotations. Inertial forces of the outflowing mass flux induce a strong toroidal magnetic field component resulting in magnetic hoop stresses which self-collimate the magnetic field structure together with the hydrodynamic mass flux. Eventually, when all the dynamical forces along the field line are balanced again, the flow achieves a steady-state. The steady state magnetic field configuration obtained after the pure MHD flow is shown as *white dashed* lines in Fig. 4.5.

[g]Full movies are available for download at http://www.mpia.de/homes/vaidya/Bhargav_Vaidya/Simulations.html

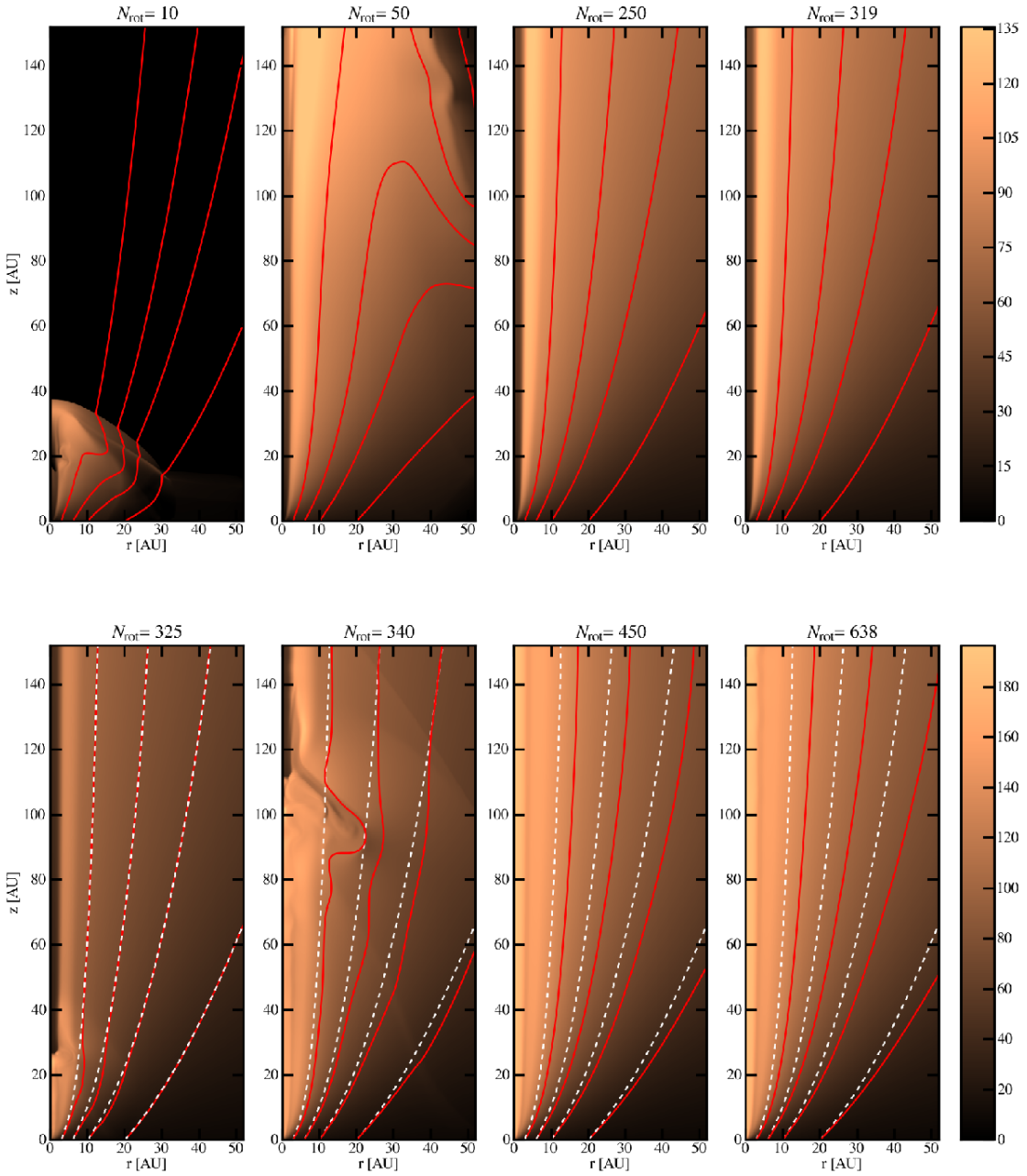

Figure 4.5: Evolutionary sequence of the reference simulation M30a055b5. Shown is the jet vertical velocity distribution (color coding) and the poloidal magnetic field lines. The color bar represents the velocity scale in km s^{-1} for each row of panels. The series of images are taken at subsequent inner rotations as mentioned on the top of each image. The *solid red lines* are the poloidal magnetic field lines. To illustrate the impact of radiation forces, we also show the field lines obtained after the steady-state MHD flow for comparison as *white dashed lines* in the lower four panels.

At this stage we *switch on* the line-forces of the central star. Immediately, the emergence of a fast axial flow is visible. This flow is unsteady, first forming a knotty structure, and then, when approaching the upper boundary, stabilizes to a steady axial flow. Jet de-collimation by stellar radiation forces is indicated by the fact that the *red solid* field lines in the *bottom* panels of Fig. 4.5 do open-up significantly as compared to field lines in steady-state pure MHD simulation.

When the radiative force is switched on, a shock front begins to propagate into the steady MHD jet (Fig. 4.5). This happens, because the additional radiation forces lead to an initial disturbance at the base of the flow, which is then propagated outwards. The effect of line-forces resulting in a series of propagating shocks is best seen in the poloidal velocity profile along a magnetic field line (see Fig. 4.6). The series of shocks eventually propagate out of the domain, and the flow attains a steady state again. However, the asymptotic outflow velocity which is then achieved is enhanced by a factor 1.5 - 2 compared to the pure MHD flow.

We have also carried out a run, M30a055b5-c, that includes the radiation force right from the beginning along with the MHD flow. This flow evolves into the same configuration as our reference run where radiation force is "switched on" later. This proves that the initial conditions do not affect the final state of the flow. In our study, we prefer to use the step-by-step approach as it is computationally less expensive.

In summary, we find that radiation forces modify the MHD disk jet essentially in terms of collimation, but also in terms of acceleration and terminal speed.

Analysis of the force-balance in the outflow

Here we investigate the main forces affecting the outflow dynamics, comparing the magnitude of various force terms calculated at each grid point along the field line rooted at r = 5.0 AU for simulation run M60a055b5. Figure 4.7 shows such a comparison of specific forces projected *parallel* and *perpendicular* to the field line before and after considering line-forces due to stellar radiation. With respect to acceleration, the most striking feature is the enhanced specific pressure gradient force. When radiative forces are considered, the steady MHD flow material at higher altitudes is adiabatically compressed from the underlying accelerated material leading into a shock that propagates out of the domain. The resultant flow has higher temperature or an increase in thermal pressure. We also find that the gradient of the thermal pressure higher above in the flow may increase substantially, such that thermal pressure force and Lorentz force may become comparable. In terms of collimation, it is evident from Fig. 4.7 that the profile of the perpendicular component of the pressure gradient force along the field line becomes flatter than in the pure MHD flow case. Thus, the pressure force which was not important for pure MHD flows, now becomes a significant factor in governing the dynamics of the initial flow acceleration

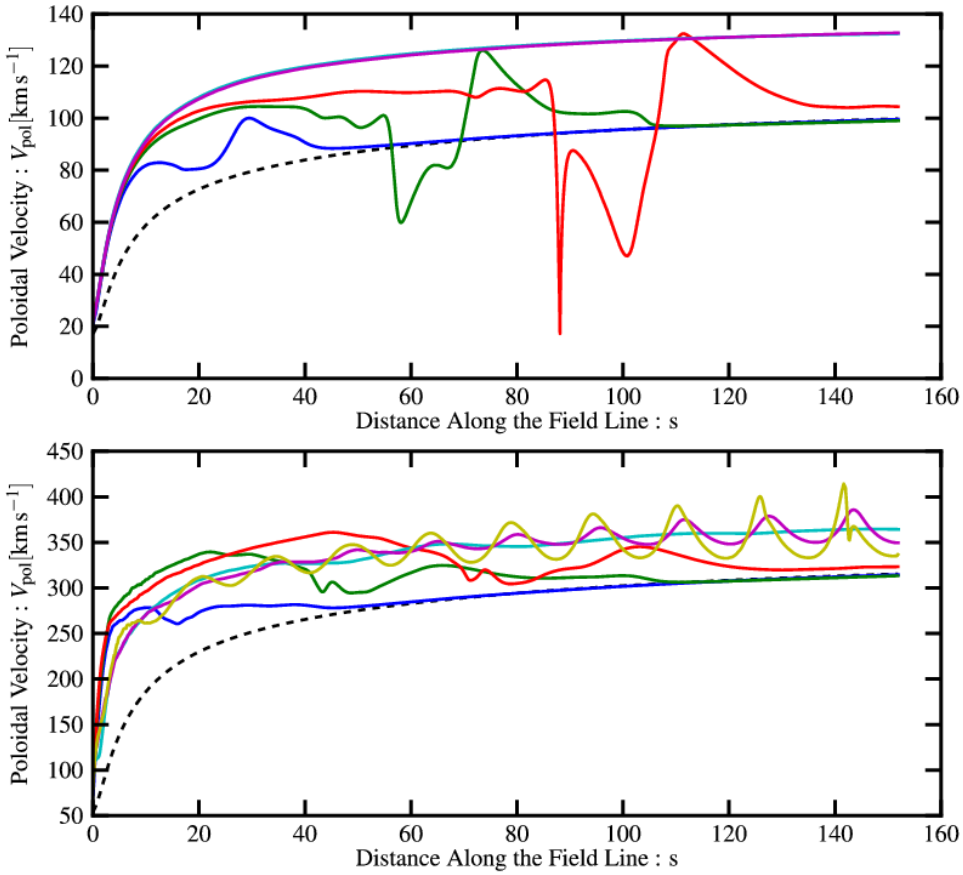

Figure 4.6: Poloidal velocity along the field line rooted at r = 3 AU for the two simulations M30a055b5 *top panel* and Disk2 *bottom panel*. The distance along the field line *s* is measured in AU. The various colored *solid* curves indicate the velocity profile at different inner disk rotations $N_{\rm rot}$ (*blue* for $N_{\rm rot}$= 325, *green* for $N_{\rm rot}$= 333, *red* for $N_{\rm rot}$=340, *cyan* for $N_{\rm rot}$= 510, and *magenta* for $N_{\rm rot}$ = 638). The *black dotted* line in both panels correspond to the last time step for the pure MHD flow. The *solid yellow* line shown in the bottom panel indicates the poloidal velocity profile after 1500 inner rotations.

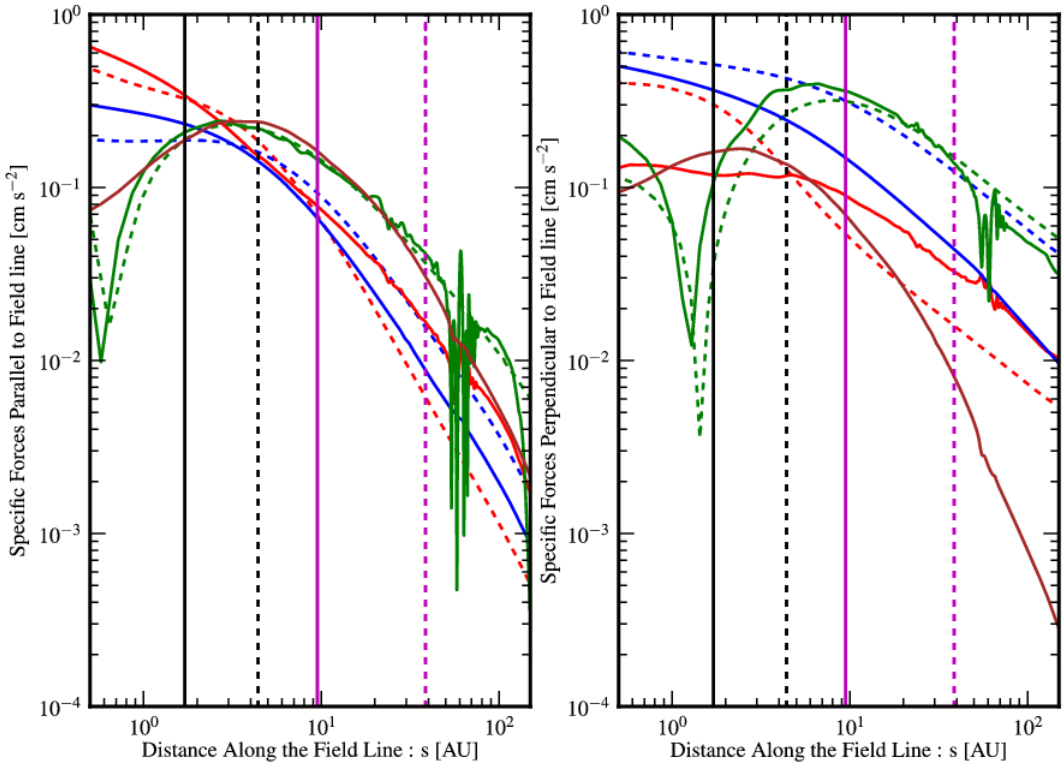

Figure 4.7: Comparison of all specific force terms projected *parallel*[left] and *perpendicular*[right] to the field line rooted at r=5.0 AU for the run M60a055b5. Colors specify different specific force terms in dyne cm^3 g^{-1} - the Lorentz force (*green*), the gas pressure gradient (*red*), and the centrifugal force (*blue*). The *dashed lines* corresponds to the respective force terms for the pure MHD run M60a055b5 (at steady-state), while the *solid lines* represents the forces for the final time step of the simulation including radiative forces. The *brown solid line* represents stellar radiation force term for the final time step. The *black* and *magenta* vertical *solid lines* mark the position of the Alfvén and the fast magneto-sonic surface for the steady state flow including radiative forces, whereas the corresponding *dashed lines* are for the pure MHD flow.

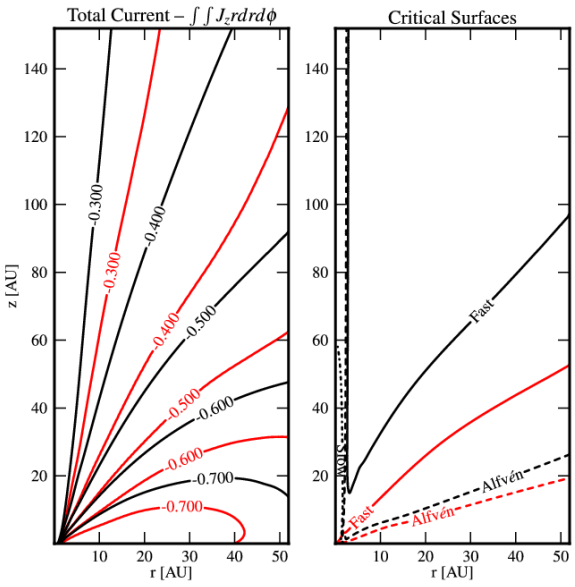

Figure 4.8: Contours of the total poloidal electric current distribution (*left*), and the location of the MHD critical surfaces (*right*). In both panels, the pure MHD flow is represented by *black solid lines*, while the radiative MHD flow is shown with *red solid lines*.

(disk wind).

Contrary, when the line-driving force is switched-on in the MHD jet, the centrifugal force becomes reduced by an order of magnitude particularly at high altitudes in the flow. In order to comprehend this variation of centrifugal force, it is useful to compare the conserved quantities of MHD, in particular the angular velocity of the field line $\Omega_{\rm F}$. In the pure MHD simulation $\Omega_{\rm F}$ is conserved throughout the simulation. This remains true also with radiative forces included, simply because $\Omega_{\rm F}$ is fixed as boundary value (see Sect. 4.4.3). Therefore, the azimuthal velocity at the base of the flow is given by equation (4.26). At the same time, the additional line forces accelerate the flow (close to the base) to higher poloidal velocities. The magnetic flux at the base is fixed as a boundary condition. Hence, the ratio of mass load to density η/ρ in equation (4.26) increases, and since the toroidal magnetic field B_ϕ is negative, also the azimuthal velocity decreases. This eventually leads to a decrease of the specific centrifugal force when line-forces are considered. The decrease in centrifugal force further implies that the outflow rotates slower, and that the acceleration close to the base is not only controlled by magneto-centrifugal forces, but also by the thermal pressure force and the radiation force (see Fig. 4.7).

Close to the base of the flow, Lorentz forces are dynamically not important. However, they peak at the Alfvén point of that particular field line. Beyond the Alfvén point, the Lorentz force becomes important and competes with other forces to govern the dynamics of the flow. When

radiative force are considered, the Lorentz force close to the base of the flow and also at higher altitudes do not show significant deviations from its values in the pure MHD case.

Line-driven radiative forces have considerable impact on the poloidal electric current distribution and also on the critical MHD surfaces in the jet. The contour plots shown in Fig. 4.8 compare the total poloidal current $I = rB_\phi = \int \vec{j}_p d\vec{A}$ and position of critical surfaces before and after considering line-driven forces in the reference simulation M30a055b5. The figure shows that by adding radiative forces (stellar luminosity), the corresponding poloidal electric current density contours are shifted closer to the base of the flow, implying a lower toroidal field strength B_ϕ in these jets. We understand this results as a consequence of lack of jet rotation, thus less effective induction of toroidal magnetic field.

Jet collimation in the conventional Blandford-Payne picture is caused by magnetic hoop stresses ($-B_\phi^2/r$) of the azimutal magnetic field. Whereas, the larger toroidal magnetic pressure gradient aids in de-collimating the outflow. A lower B_ϕ would not only weaken the hoop stress but also reduce the magnetic pressure ($\sim B_\phi^2$). The decrease of toroidal magnetic pressure would lead to a lower magnetic pressure gradient force. So, a balance arises between the hoop stress that collimates the flow and the toroidal pressure gradient that de-collimates it. We observe that the field lines de-collimate to a wider configuration on addition of radiative forces, implying that the decrease of toroidal magnetic field has more impact on reducing of hoop stresses than reducing the magnetic pressure gradient, thus eventually de-collimating the flow.

Considering radiative forces also results in lowering the location of MHD critical surfaces (viz. slow magneto-sonic, fast magneto-sonic and Alfvén surface) (see Fig. 4.8). The pure MHD flow is launched marginally super-slow and sub-Alfvénic. The flow near the axis is, however, sub-slow, due to the boundary condition of conserving the initial hydrostatic density and pressure distribution in the gap region between axis and disk. The flow speed at the critical points depends on the magnetic flux and mass density in the flow. These quantities remain approximately unaltered when radiative forces are considered, thus the magneto-sonic wave speed remains similar as well. Since now the radiative line-forces accelerate the wind further to higher velocities, the critical surfaces shift to lower altitudes in the flow (i.e. close to the base of the flow).

We finally note that radiative forces have both a direct as well as an indirect effect in modifying the collimation properties of the flow. The radiation force from the star *directly* affects the flow dynamics at its base and close to the star simply by transfer of momentum (equation 4.2), eventually leading to a flow de-collimation. *Indirectly*, the radiation field also enhances the thermal pressure in the flow (equation 4.3) such that the specific pressure force becomes comparable to the Lorentz force - further de-collimating the flow. The resulting opening angles as measured from our reference run at various critical points along the field lines are listed in Table 4.2. For M30a055b5, the final state of the jet has a steady mass outflow rate of 2.5×10^{-5} $M_\odot\,yr^{-1}$. The

opening angles are 26° and 23° at Alfvén and fast point respectively for the field line which has a foot point r = 5 AU. The maximum percentage separation $\Delta\zeta[\%]$ between the opening angles of this field line in pure MHD flow and that for the flow with radiative forces is 34.5%. A significantly positive value of $\Delta\zeta[\%]$ indicates flow de-collimation. In the following sections, we describe the effects of various physical parameters that could affect the dynamics of the outflow.

Radiation field and magnetic field strength

Here we discuss the interrelation between radiative forces and a variation of magnetic flux and their combined effect on outflow collimation. We compare simulation runs M30a055b1, M30a055b3, and M30a055b5, all assuming the same stellar mass 30 $M_\odot$, an inner jet launching radius of 1 AU, and a density at the base of the flow of $5.0 \times 10^{-14}\,\mathrm{g\,cm^{-3}}$, while the initial magnetic field strength parametrized by β_0 ranges from 5.1 G to 11.5 G.

The (initial) pure MHD runs exhibit characteristic differences. A lower β_0 provides faster jets which are more collimated, simply because the larger field strength provides larger Lorentz forces to collimate and also accelerate the flow more efficiently. A lower field strength implies a lower magneto-sonic wave speed, resulting in magneto-sonic surfaces located closer to the disk surface. Thus, we cannot simply compare the opening angles at the critical surfaces as their positions vary in the pure MHD runs with different field strengths. Instead, we quantify the actual *change of opening angle* with and without considering radiative force $\Delta\zeta[\%]$ (i.e. in percentage), as profile along the field line.

This measure is shown in Fig. 4.9 for a field line rooted at r = 5 AU. We see that $\Delta\zeta[\%]$ is significantly positive, indicating that radiative forces do considerably de-collimate the flow. However, the effect of de-collimation is enhanced when the magnetic field strength is reduced (i.e. an increase of β_0). The asymptotic value of $\Delta\zeta[\%]$ along a field line changes from 35% to 5% when the initial magnetic field strength is increased by a factor of two.

The above analysis for different magnetic field strength suggests that in the strong field case ($\beta_0 = 1$) jet collimation is controlled by the magnetic forces alone. However, when we decrease the field strength (from 11.5 G to 5.1 G as normalized at 1 AU) the stellar radiation line-force begins to compete with the magnetic forces. The resulting jet has a much wider field structure and outflow opening angle as it is de-collimated as compared to its pure MHD counterpart (see Fig. 4.5). We conclude that radiative forces from the central star (for the chosen parameters) will dominate the magnetic effects in controlling the flow collimation for field strengths $\lesssim 5$ G (at 1 AU). In addition to the field strength the field profile is also important in dynamical evolution of the jet flow (see Sect. 4.2.3). Observational estimates of the field strength in these close by regions of massive young stars will further help to narrow the results.

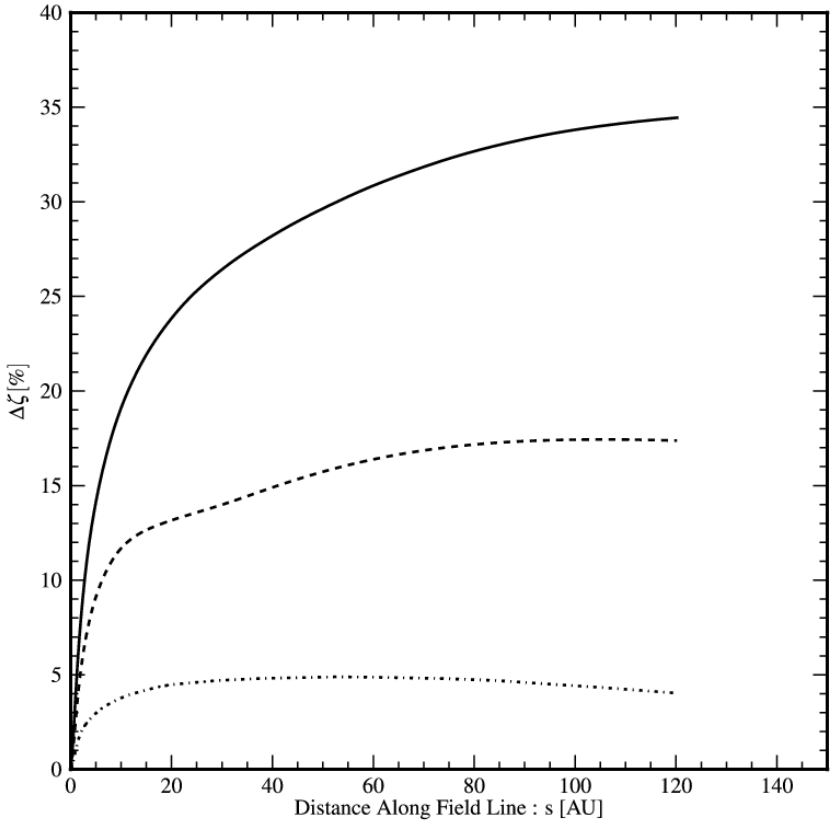

Figure 4.9: Flow collimation along the field line rooted at r=5 AU. Shown is the profile of the percentage separation of field lines between the pure MHD flow and the radiative MHD flow [$\Delta\zeta[\%]$] as measure of flow collimation. The *solid*, *dashed* and *dot dashed* lines are for three different plasma-β_0 = 5.0, 3.0, 1.0, respectively.

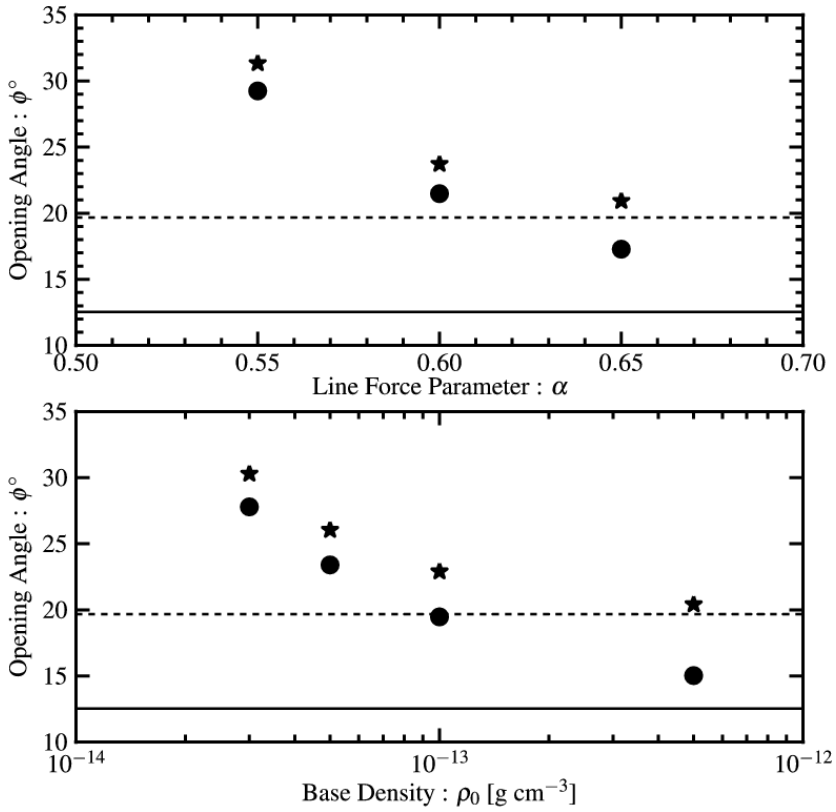

Figure 4.10: Jet collimation, jet density and radiation force. Shown is the opening angle (i.e. the field inclination) at the Alfvén point (*stars*) and the fast point (*dots*) of the field line rooted at r=5 AU for runs with different α (*top panel*), and different jet base density ρ_0 (*bottom panel*). The *dotted* and *solid* lines corresponds to the opening angle at the Alfvén point, and the fast point of the same field line after the pure MHD flow with an initial plasma-β_0 = 5.0.

Impact of the line-force parameter α

The stellar line-force is a non-linear function of α. Gayley (1995) showed that a significant change in the mass flux can be obtained with very slight change in α, indicating that this parameter is very sensitive for calculation of radiative line-forces.

Simulation runs M60a055b5, M60a060b5, and M60a065b5 apply the same magnetic field strength ($\beta_0 = 5.0$), but differ in the line-force parameter from $\alpha = 0.55 - 0.65$. A first result is that the increase of α from 0.55 to 0.60 decreases the mass outflow rate significantly by $\sim 16\%$. We will discuss this interrelation in Sect. 4.6.2. However, also the outflow opening angles are affected as indicated by the top panel of Fig. 4.10. The outflows with lower α become more de-collimated than the others with higher α.

The above trend indicates that the efficiency of the line driving mechanism is increased with lower α. Physically a lower α implies a higher contribution of optically thin lines in accelerating the flow. Thus, the dominance of less saturated (i.e. less self-shadowed) lines in accelerating the flow results in an efficient line driving.

In summary, we find that the runs with lower α have higher mass flux and are less collimated. Our results from studying different α are in qualitative agreement with the analytical results from Gayley (1995).

Impact of the density ρ_0

In this section, we describe how collimation and acceleration in the outflow are altered with the density at the base of the flow. As mentioned in Sect. 4.5.3, the physical mass density applied to scale the numerical simulation is a free parameter in our setup, were we estimate its value from the observations using equation (4.29).

Simulation run M30a055b5d1 has the lowest density among all four runs, $\rho_0 = 3 \times 10^{-14}\,\mathrm{g\,cm^{-3}}$ For this run, the opening angles measured at critical MHD surfaces are larger compared to our reference run. Quantitatively, the opening angles at the Alfvén and the fast surface are 30° and 28°, respectively. Also, the maximum percentage change in field line opening angle $\Delta\zeta[\%]$ increases from 35% for the reference run to a staggering high value of 48% for field line rooted at r = 5 AU. In case of a high jet base density ρ_0, the change in field line opening angle $\Delta\zeta[\%]$ reduces to 4%, with the opening angles at the Alfvén and fast surface being 20° and 15°, respectively (Fig. 4.10).

These results correspond to an inverse correlation of the density at the base of the flow with the force multiplier $M(\mathcal{T})$ (see equation 4.14). Higher densities result in an optically thick environ-

ment, thus increasing the the optical depth parameter $\mathcal{T}$, and reducing the force multiplier. Thus, the radiative *line-driving* force approaches the limit corresponding to the *continuum* radiation force. Essentially, the continuum force for typical massive young stars is weak compared to other dynamically important forces (for e.g. gravity).

In summary, we observe the outflow density as one of the leading parameters to govern the dynamics of the outflow by radiation forces. However, observationally this density is very difficult, even impossible to determine. We thus have to rely on certain assumptions, or may apply estimates of the outflow flux to calculate this density. Our parameter survey considers density values which are consistent with the observed mass fluxes. From our studies, we observe in general that for densities $\rho_0 < 10^{-13}\,\mathrm{g\,cm^{-3}}$ the line-driving force from the central star is very efficient in accelerating and de-collimating the outflow. However, a denser environment will dilute the influence of the line-driving mechanism.

Stellar mass evolution and outflow collimation

Motivated by the hypothesis of Beuther & Shepherd (2005) we have studied the outflow dynamics and collimation for a sequence of different stellar masses (viz. from 20 $M_\odot$ to 60 $M_\odot$). The change in stellar mass implies a change in the central luminosity. Fig. 4.11 shows the variation of the opening angle at the MHD critical points in simulation runs with central stellar mass. It can be seen that the opening angle varies from 20° to 32° for stellar masses from 20 $M_\odot$ to 60 $M_\odot$. The curve rises linearly up 30 $M_\odot$, but then the opening angle does not change considerably for increasing mass.

For the physical parameters of the stellar evolution such as stellar luminosity and radius, we have applied the *bloating star* model of Hosokawa & Omukai (2009) assuming an accretion rate of 1.0×10^{-3} $M_\odot\,\mathrm{yr}^{-1}$ (see Fig. 4.3). In this model for massive young stars, the stellar luminosity increases rapidly from 6 $M_\odot$ to 30 $M_\odot$. A star with high accretion rate undergoes swelling and is considered to bloat up to 100 $R_\odot$. It is the entropy distribution in these stars which causes them to expand in size that much. For stars < 10 $M_\odot$, a thin outer layer absorbs most of the entropy from its deep interiors, thereby increasing the entropy in this layers. The rapid increase of entropy in the outer layer of the star causes the star to increase in size (Hosokawa & Omukai 2009). When the stellar mass reaches ∼ 10 $M_\odot$, the star then begins to shrink (Kelvin-Helmholtz contraction) until its mass reaches ∼ 30 $M_\odot$. After that, the star approaches the main sequence and then follows the typical main sequence evolution. The stellar luminosity does not change considerably from $M_* = 30$ $M_\odot$ to 40 $M_\odot$ - in fact there is a slight decrease. Contrary, for stars with mass > 40 $M_\odot$ the stellar luminosity increases with mass. This is reflected as a slight dip in the variation of Γ_e with mass between 30 $M_\odot$ and 45 $M_\odot$. Thus, the values of Γ_e derived for these two masses do not show considerable difference (0.2381 and 0.2269 respectively). We conclude

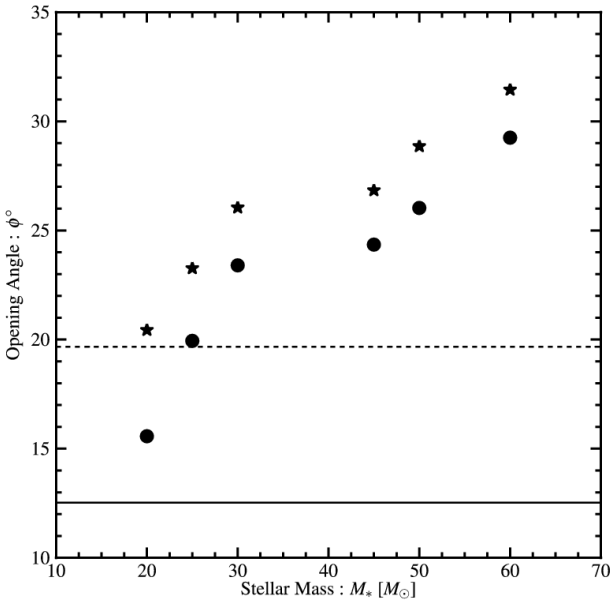

Figure 4.11: Same as Fig. 4.10, but for simulation runs for different stellar mass.

that the radiation force and, hence, also the dynamics of the outflow do not change to a great extent for these masses.

For simplicity we keep the inner jet launching radius and the density at the base of the flow fixed for all mass runs. The radiation force is not only altered by changes in Γ_e, but also due to the physical scaling that appears in the prescription of the force multiplier. In particular, this is the Keplerian velocity at the inner launching radius l_0, which is naturally different for different masses and scales with $\sqrt{M_*}$. One would then expect that the radiative force changes by a factor equivalent to $\sqrt{M_*}$. The effect of such a change with increasing central mass not only enhances the mass flux launched from the disk boundary but also imparts the resulting outflow a wider morphology (see Table 4.2).

In summary, with the above parameter study of different central stellar masses, we observe that as the luminosity (or mass) of the central star increases, the stellar radiation force becomes relatively stronger. This leads to a higher degree of outflow de-collimation confirming the above mentioned observational picture of outflow evolution in massive young stars.

4.6.2 Radiation field and jet mass flux

The simulations presented so far have been performed with *floating* boundary conditions at the base of the flow (see Sect. 4.4.3). While guaranteeing a causally correct boundary condition *ab initio*, the disadvantage is that the mass flux emerging from the underlying disk boundary cannot be prescribed *a priori*. In fact, the mass flux is self-consistently calculated each time step by ensuring continuity of outgoing waves between the domain and the ghost cells. Thus, in our approach applied so far we fix the initial flow density and float the vertical outflow velocity at the boundary.

The total mass outflow rate ($\dot{M}_{\rm rad}$ + $\dot{M}_{\rm vert}$) in physical units is shown in Fig. 4.12 for runs with different stellar mass and applying a floating boundary condition. The total mass flux has a $\sqrt{\rm M_*}$ dependence for pure MHD runs on converting it to physical units. While for a steady-state radiative MHD flow, the physical mass flux also depends on the Eddington parameter $\Gamma_{\rm e}$, which is related to the stellar luminosity.

The percentage change between these mass outflow rates is shown in the bottom panel of Fig. 4.12. Interestingly, the profile of this curves is similar to the variation of the opening angles (see Fig. 4.11), indicating that the increased mass flux could in fact play a role for de-collimation. Thus, the combination of both the *floating* boundary conditions and the disturbance of the gas physics at the base of the flow by radiative source terms leads to the enhanced mass flux, which modifies the collimation of the flow.

However, also the direct effect of radiative force on the flow can physically deflect the flow and eventually lead to de-collimation. Thus, the problem becomes quite complex as the direct influence of radiative force on the flow is mingled with its second order effects for e.g. increase in the mass flux. In order to single out the influence of direct de-collimation effects by radiative forces, we have performed simulations where we have fixed the outflow mass flux as a boundary condition.

It is essential to inject the outflow with a velocity which is supersonic to begin with. We fix the mass flux at the boundary by setting the inflow velocity to $u_{\rm z} = 0.24 \times u_{\rm Kep}$, resulting in a flow with slow magneto-sonic Mach number close to unity and indicating a slightly supersonic flow. In Fig. 4.13 we show the mass outflow flow rates derived along the top ($z = z_{\rm m}$) and right ($r = r_{\rm m}$) boundaries (in red and blue, respectively). We have calculated the radial and vertical mass outflow rates using following expressions,

$$\dot{M}_{\rm rad} = r_{\rm m} \int_0^{z_{\rm m}} \rho u_r|_{r_{\rm m}} dz, \tag{4.30}$$

$$\dot{M}_{\rm vert} = \int_0^{r_m} r \rho u_{\rm z}|_{z_{\rm m}} dr. \tag{4.31}$$

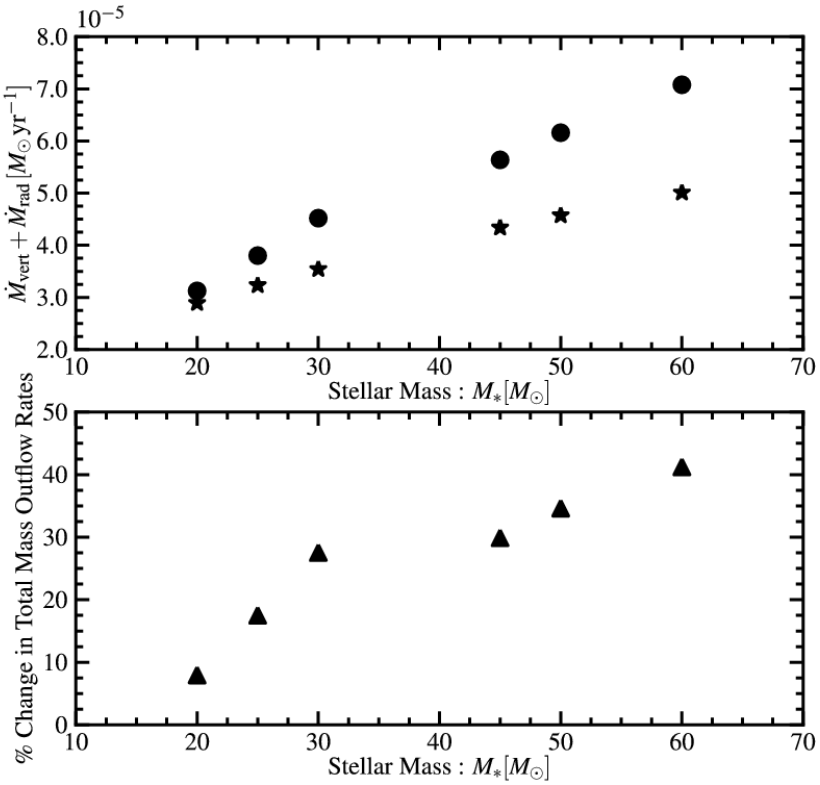

Figure 4.12: Outflow mass flux for simulations applying a different stellar mass. The *top panel* shows the total mass outflow rates for each star in case of a pure MHD flow (*stars*), and for the same outflows including radiative forces (*dots*). The percentage difference between these mass fluxes is shown in the *bottom panel*.

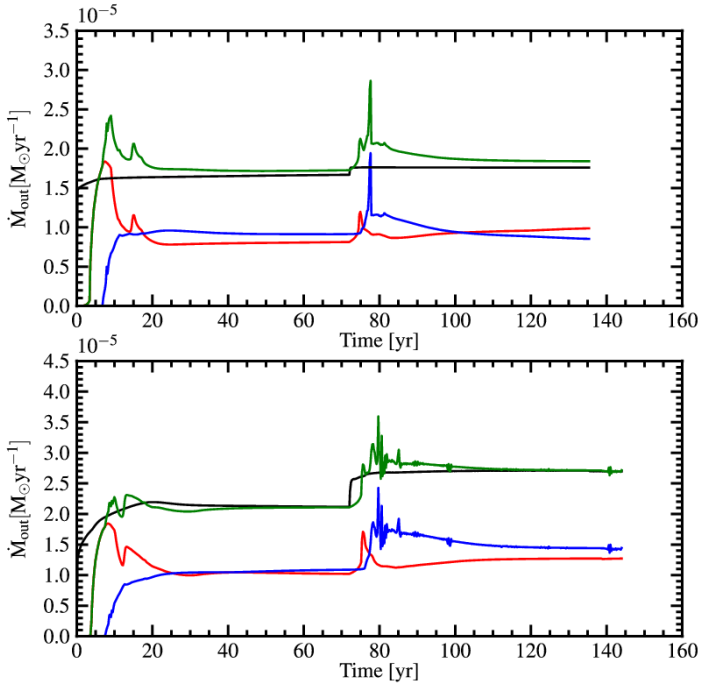

Figure 4.13: The variation of the outflow mass flux with time in simulation runs M30a055b3inj (*top panel*) and M30a055b5 (*bottom panel*). The *red* and *blue lines* show the variation of the vertical and radial mass fluxes, respectively (see equation 4.30 and 4.31). The *black line* corresponds to the mass flux injected from the underlying disk. The *green line* is the total mass flux leaving the computational domain. Coinciding green and black lines proves conservation of the mass flux.

In the simulations with floating boundary conditions, we observe that the mass flow rate reaches a steady-state, first derived self-consistently in the pure MHD flow, and then suddenly increased on adding the radiative source term. Essentially, this rise is not seen when we apply fixed-mass-flux boundary conditions. However, the fact that the curves of radial and vertical mass flux intersect after $\sim$ 60 disk rotations after switching-on the radiation force, is a clear signature of de-collimation. Thus, the modification in terms of collimation due to the *direct* impact of radiative forces on a flow injected with constant mass flux can be now understood with our simulation runs with *a priori* fixed-mass-flux boundary conditions.

We have thus performed three simulation runs with different stellar mass applying the above-mentioned mass-injection boundary condition (see Table 4.2). The most evident measure of de-collimation that can be observed is the ratio of vertical to radial mass flow rate. A higher ratio indicates a higher degree of jet collimation. This mass flux ratio for the chosen stellar masses of 25, 30, and 50 $M_\odot$ changes from 1.12 after the steady-state pure MHD flow to 0.92, 0.85, and 0.80 respectively, when radiative force is considered. Note that the radiative forces also

accelerate the flow, increasing the maximum velocity for M30a055b3inj in steady-state radiative MHD by a factor of ~ 1.5 compared to pure MHD flow.

We also find, that de-collimation is mainly due to the *direct* influence of the stellar line-driven force on the outflow, as the amount of mass flux launched into the domain is fixed for these runs (it is thus not a 2nd-order effect resulting from a higher mass flux due triggered by the radiation force).

In summary, we conclude here that the line-driving radiation force from the star plays a significant role in directly modifying the dynamics of previously launched MHD flow. This force not only aids in acceleration of the flow, but also pushes the outflow material away from the axis resulting in a substantially wider opening angle.

4.6.3 Acceleration by the disk radiation field

We have also carried out a number of simulations that involve only radiation forces caused by a (hot) accretion disk. In principle, in addition to the intrinsic accretion luminosity, the disk radiative force can be enhanced by considering irradiation from the central star (Proga et al. 1998, Drew et al. 1998). For the present model, however, we do not consider irradiation.

Here we present results of two of our simulations, denoted as Disk1 and Disk2 (see Table 4.4). We have applied the parameter set as for the reference simulation M30a055b5, however, two more parameters governing the dimensionless accretion rate that appears in the accretion luminosity (equation 4.19) have to be prescribed. That is the ratio μ of disk to stellar luminosity, and the ratio Λ of stellar radius to inner launching radius (see Table 4.1). Naturally, a disk extending to radii closer to the center of gravity would have much higher temperatures thus luminosity (see Vaidya et al. 2009 for an application to massive young stars) and the resulting radiation forces would be able to affect the outflow more.

For the number values applied for these additional parameters we again follow the *bloating star* model (Hosokawa & Omukai 2009) assuming an accretion rate of 10^{-3} $M_\odot\,yr^{-1}$, and an inner jet launching radius of $l_0 = 0.1$ AU, thus, obtaining $\mu = 0.4644$ and $\Lambda = 0.4969$. Note that the smaller inner jet launching radius also implies a inner disk radius closer to the star, compared to our models discussed above.

For simulation run Disk2, we have increased the magnitude of the disk radiative force by decreasing the density at the inner jet launching radius by a factor of 10, thus assuming $\rho_0 = 5 \times 10^{-15}\,g\,cm^{-3}$. The contours of line force due to disk in run Disk2 is shown in Fig. 4.14 (see Sect. 4.4.1). As the radiation force is very sensitive to the density, the lower density at the jet base does increase the radiation force from the disk by a factor of three. Note that, physically,

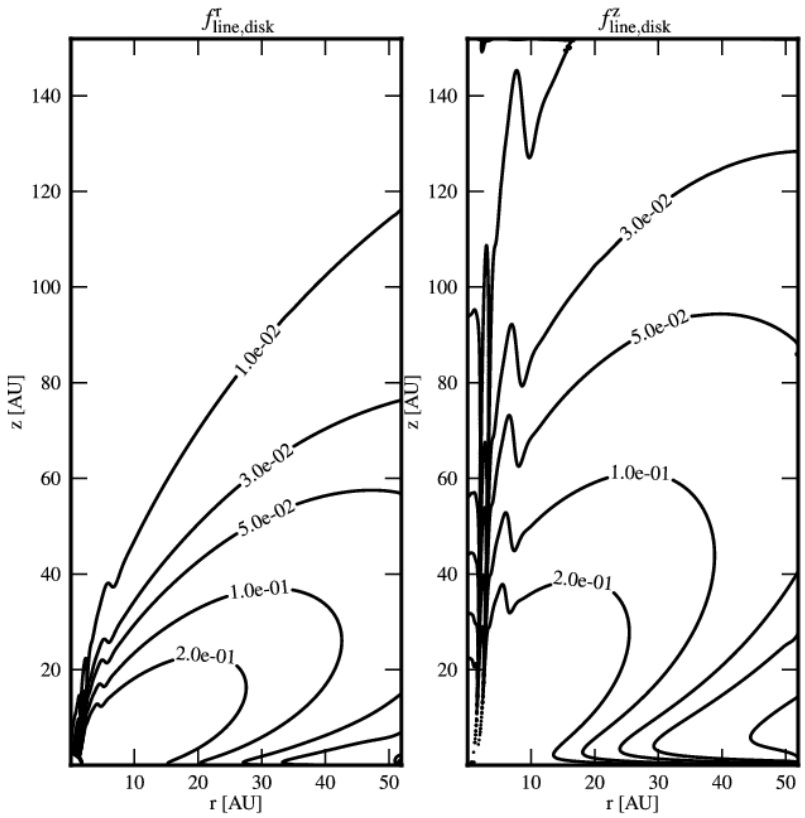

Figure 4.14: Contours of the line force from disk radiation in the radial (*left panel*) and vertical (*right panel*) direction. The contour levels are given in physical units. The parameters used are : $Q_0 = 1400.0$, $\alpha = 0.55$, $M_* = 30\ \mathrm{M}_\odot$, $l_0 = 0.1\,AU$, $\rho_0 = 5.0 \times 10^{-14}\,\mathrm{g\,cm^{-3}}$, $\Gamma_\mathrm{e} = 0.2369$, $\Lambda = 0.4969$, $\mu = 0.4644$, $\beta_0 = 5.0$

this increase of the disk radiation force could mimic the effects of stellar irradiation.

We quantify the change in collimation degree in runs Disk1 and Disk2 again with the parameter $\Delta\zeta[\%]$ (see equation 4.27). Simulation run Disk1 has a maximum of $\Delta\zeta[\%] = -1.8$, while run Disk2 has $\Delta\zeta[\%] = 3.1\%$. These number values are rather low compared to our simulations with a stellar radiation force indicating that the *disk radiation force alone is not strong enough to de-collimate the flow*.

Interestingly, simulation run Disk2 shows some unsteady behavior close to the axis - a feature which is absent when only stellar radiation forces were considered. The vertical velocity map along with the magnetic field lines for simulation run Disk2 is shown in Fig. 4.15. We show the magnetic field line distribution when the pure MHD flow has reached steady-state (*white dotted*) and the field line configuration when disk radiation forces are included (*red solid*). This is consistent with the findings of Proga et al. (1999), who detect a similarly unsteady behavior in their simulations for the case when the radiative force is dominated by the underlying disk. The fact that we do not see this feature in simulation Disk1 suggests that the radiative force in run Disk1 is not comparable to the other forces that control the flow dynamics, and that this outflow does more correspond to a pure MHD flow.

The unsteady flow behavior in run Disk2 is also reflected in the poloidal velocity evolution as steadily propagating 'wiggles' in the velocity profile along the field line (or streamline) $u_{\rm p}(s)$ (Fig. 4.6).

As maximum outflow velocity for the simulations Disk1 and Disk2 we obtain relatively high velocities of ~ 350 kms^{-1}. This is mainly due to the above mentioned fact that the outflow is launched deeper in the potential well and as close as $l_0 = 0.1$ AU from the central star. Compared to the pure MHD run, we see, however, that the jet which is affected by disk radiation forces (only) achieves slightly higher asymptotic velocities, as the MHD reaches only ~ 300 km s^{-1}. Thus, the disk radiation force affects the outflow primarily by slightly accelerating it. We do not see indication that the outflow collimation is affected, which is understandable since the disk radiation force acts mainly in vertical direction.

In summary, jet acceleration and collimation is rather weakly affected by the disk radiative forces as their magnitude is orders of magnitude smaller compared to radiation forces from the central star. However, for other astrophysical jet sources such as AGNs, the radiative force from the disk could play a significant role (e.g. Proga 2003).

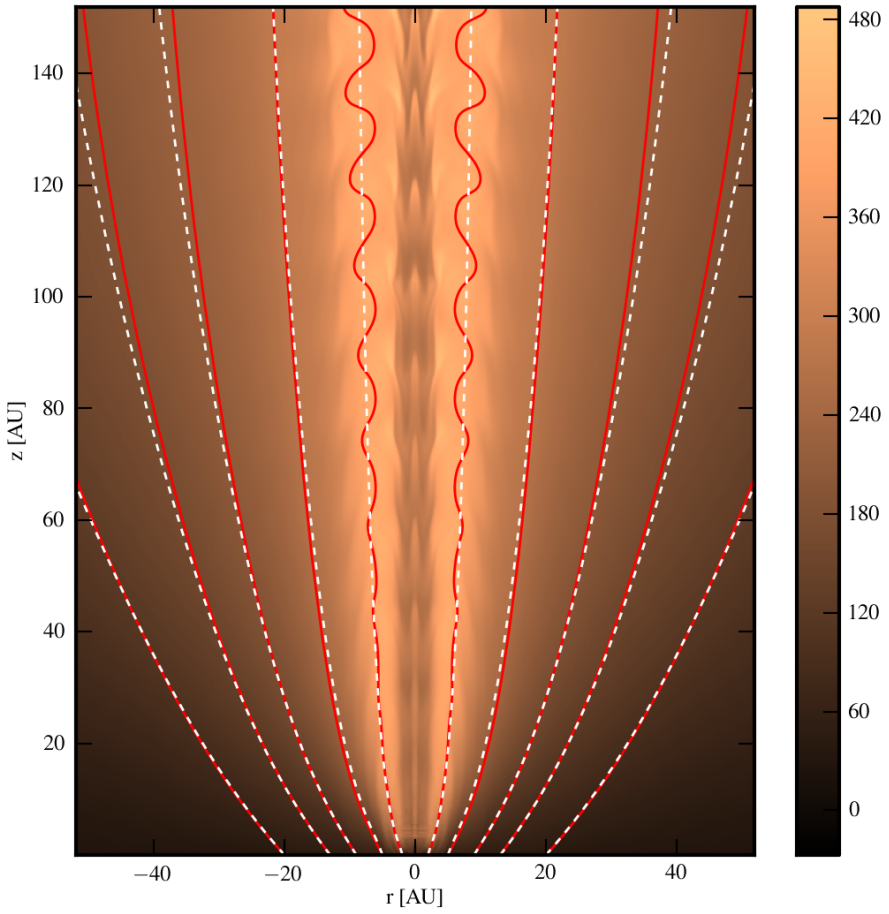

Figure 4.15: Poloidal jet velocity (mirrored at the jet axis) in $\mathrm{km\,s^{-1}}$ for the simulation run Disk2. The *white dotted lines* show the magnetic field line distribution for the pure MHD flow and for the MHD flow including the disk radiation forces *red solid lines*. The color bar represents the jet vertical velocity u_z in code units. The unsteady evolution of the axial flow is discussed in the text.

4.6.4 Limitations of our model approach

The main goal of our study was to disentangle the effects of radiative forces from the young star-disk system on a pure MHD outflow launched within the standard picture of magneto-centrifugal, magnetohydrodynamic jet formation. In this section we discuss the limitations of our model approach to the subject of jet formation from massive young stars.

Prescription of radiation force

The prescription of radiation force used for the present model does not explicitly consider the radiation transfer. Instead it implements the radiative force due to lines as a source term in the momentum and the energy equations (see Sect. 4.3). This greatly simplifies the numerical task and modeling becomes computationally inexpensive.

Possible existence of a stellar wind

Our model does not consider a stellar wind from the massive young star. Observed outflows around young massive stars are usually thought to have velocities of about 200 - 500 $\mathrm{km\,s^{-1}}$, a value much smaller than the speed of stellar winds in the evolved stages of OB stars (of about $\sim 1000\ \mathrm{km\,s^{-1}}$). This difference in velocity scale could give a clue to difference in environment around the star. During the formation stage, the star is surrounded by dense gas and dust as compared to more evolved stage where it has cleared all surrounding matter. A rarer environment in a more evolved stage could lead to an efficient acceleration of winds via line driving to 1000 $\mathrm{km\,s^{-1}}$. Hence, for more massive and hotter young stars, impact due stellar winds could play a vital role on the dynamical evolution of disk winds.

Lack of knowledge of system parameters

The inner regions around massive young stars are not accesible with present day telescopes. Thus, many physical parameters for these inner regions are not observationally constraint (for e.g the inner disk radius, mass density, magnetic field strength) In the present model, we follow the notion that high-mass stars form as a scaled-up low-mass stars. Thus most of the parameters used for the present modeling are derived from estimates for low-mass stars.

Ideal MHD approach

Simulations presented here are done using ideal MHD approximation. This is in principle fine as ionizations fractions are usually high enough to provide a good coupling between matter and field. However, for simplicity we have assumed a constant ionization fraction throughout the wind. Since the radiative force parameters do have an explicit dependence on the ionization fraction, the idealized assumption of a constant ionization fraction throughout the wind allows us to fix the radiative force parameters for all simulation runs.

Prescription of the disk dynamics

A self-consistent modeling would need to incorporate the time-evolution of the disk structure in the simulation, and to treat accretion and ejection processes simultaneously. Such simulations are currently performed in general applications of jet launching (e.g Casse & Keppens 2002, Zanni et al. 2007, Murphy et al. 2010), however, it is too early to be applicable to massive young stars - one reason being the lack of knowledge of the accretion disk parameters (e.g. the question whether there is a thin or thick disk), another one that also radiative effects would have to be implemented in these simulations.

4.7 Conclusion : Jet formation

We have studied the impact of a line-driven radiation forces on the acceleration and collimation of a MHD jets,around young massive stellar object. Our main motivation was to give a solid theoretical understanding for the outflow evolution hypothesis presented by Beuther & Shepherd (2005). For the radiation forces we have considered stellar and disk luminosity. Our basic approach was to initially launch a MHD jet from the underlying disk surface, and then, after the pure MHD outflow has achieved a steady state, to switch on the radiative forces and study their effect on the existing MHD outflow.

We performed a number of simulations with the line driving force exerted by stellar radiation. These simulations were performed for a wide range of physical parameters, as i) the central stellar mass, ii) the magnetic flux, and iii) the line-force parameter α. In order to apply our method of calculating the line driving force (CAK approach), we have modified the numerical code PLUTO to incorporate appropriate projections of gradients of the 2 D velocity field along the light path. Additionally, we have consistently implemented these projections for different radiation sources properly considering the geometry of the radiation field. All these simulations

have 'floating' and casually consistent inflow boundary in which the mass flux is not fixed and is derived by the numerical solution.

Our main conclusions from this analysis are as follows.

The line driven force from the central star for the parameters considered does play a significant role in modifying the dynamics in terms of collimation and acceleration of the outflow. We find that the outflow velocity is increased by a factor of 1.5 - 2 by radiation forces as compared to the pure MHD flow. Also, the degree of collimation is lowered, visible e.g. in a 30%-change in the magnetic flux profile, or the wider opening angle of the magnetic field lines.

Investigating different stellar masses we determine the amount of de-collimation by measuring the opening angles of a typical field lines (that with the highest mass flux) at the Aflvén and fast magneto-sonic point. We find that for a stellar mass of 20 $M_\odot$, the opening angles are 20° and 16°, respectively. For a 60 $M_\odot$ star these values increase to 32° and 29°, indicating substantial amount of de-collimation due to the increased stellar luminosity. This findings confirm the observed evolutionary picture for massive outflows in which more massive stars tend to have outflows of lower collimation degree. Note that for massive young stars, our results do not only constitute a relation of different stellar masses, but correspond also to a time-evolution of outflow systems, as the central mass can be substantially increased during massive star formation.

We have also performed simulations with injection of fixed mass flux from the disk boundary for various stellar masses. We find that the ratio of vertical to radial mass flux in these runs decreases from 0.92 to 0.80 with increase in stellar mass from 25 $M_\odot$ to 50 $M_\odot$. This clearly indicates the fact that the line driving force from central star plays an influential role in the physical understanding of observed evolutionary picture pertaining to outflows from young massive stars.

So far, the magnetic field strength in the jet formation region close-by a massive young star forming is an unknown quantity. We therefore have carried out simulations with different field strength (plasma-$\beta_0 \sim 1.0, 3.0, 5.0$). We find that for the flow with high magnetic flux the radiative forces do not really affect the collimation degree. However, for the flow with low magnetic flux, the dynamical effect of radiative forces is greatly increased.

We further find that the line force parameter α is very critical in determining the magnitude of the line-driven forces. Lower values of α leads to an efficient radiative force from the central star and thus decollimate the flow to a larger extent as compared to higher α values. Since the radiation forces also affect the mass outflow rates for simulations, even small change in α may lead to significant changes in mass flux up to $\sim 28\%$.

Line forces due to the hot accretion disk do not play a significant role in controlling the dynamics of the MHD outflow, simply because they are orders of magnitude smaller then all other forces

that affect the flow dynamically. Implementing high disk radiation forces has (by taking into account the inner hotter part of the disk), however, shown us that the disk radiation forces will affect primarily the flow acceleration, and not the flow collimation.

The source terms for the line-driven forces from the star and the disk implemented in our simulations depends on certain scaling parameters. We find that the physical scaling of the jet density is a leading parameter that affects the flow dynamics. Large densities make it difficult for the line-driving to act efficiently, resulting in a flow which is mostly dominated by MHD forces. However, less dense inner regions around massive young stars would allow efficient radiative line-driving, and thus accelerate and de-collimate the flow with great effect.

This chapter has addressed a complex problem of jet launching from young massive stars. In doing so, we have applied a simplified prescription of the radiative force rather than a complete radiative transfer calculation. One limitation of our model is the lack of observational knowledge about various parameters particularly very close to the central star. In addition, we have not included effects from stellar winds which might exist during the *later stages* of young massive star evolution. In spite of these limitations, we find clear evidence of acceleration and de-collimation of jets launched from massive young stars.

In summary, among all the radiative sources considered to study the dynamics of outflow launched from the young massive star, we see that the line force from the central luminous star is very efficient in de-collimating and accelerating the flow. The line force from the underlying disk is not as significant as compared to the stellar force. Also, dynamical effects on the outflow due to the optically thin electron scattering continuum force from the central star and the disk is not significant. Furthermore, we confirm the observed trend of de-collimation seen in outflows from massive stars at different evolutionary stages.

The optimist thinks that this is the best of all possible worlds, and the pessimist knows it.

J Robert Oppenheimer (1904-1967)

5

Dynamics of Inner Accretion disks: Radiative Transfer and Self-Gravity

The chapter is based on the work currently being done in collaboration with Prof. Mark Krumholz (University of California Santa Cruz) and Rolf Kuiper (University of Bonn).

In this chapter, we present results from an ongoing numerical study of the dynamical evolution of inner accretion disks around massive stars. We perform full three-dimensional numerical simulations of a self-gravitating massive accretion disk. These disks are perturbed via rapid inflow of material from the core. We aim to understand the transport of such material onto the central star. We find locally isothermal disks to be an ideal case for gravo-turbulent fragmentation due to very low cooling times. The spiral arms developed in these disks produce gravitational torques that transport angular momentum. In this simulation, we observe that 10% of the matter accreted by the disk is accreted on the central star. Inner disks around massive stars could also be influenced by strong radiation pressure. We carry out radiative transfer calculations using frequency average (mean) and frequency dependent opacities. The impact of radiation on fragmentation and accretion of material is the final goal of this study.

5.1 Introduction

Major advancements in sub-mm interferometric techniques have revealed existence of the flattened rotating structures around stars with mass $\geq$ 10 $M_{\odot}$ (e.g. Cesaroni et al. 2005, Patel et al. 2005, Fallscheer et al. 2011). Such rotating structures are spanned across a large scale in lengths (1000 - 10,000 AU) around the central star. They are termed as *pseudo disks* due to the fact that they are not in Keplerian balance with the central star. The evidence of these *pseudo disks* around young massive stars provide essential clues for their formation process. The natural outcome

from this observational fact is that high-mass stars form via disk accretion *aka* their low-mass counterparts. The main difference in their formation scenarios lies in the time scales involved. Massive stars are believed to evolve rapidly on the main sequence and end up into a supernova in about 1-10 Myr. This swift evolutionary process requires high mass accretion rates in disks around massive stars. Indirect measures from outflow rates give an order of magnitude estimates of $10^{-5} - 10^{-3}$ $M_{\odot}\,yr^{-1}$(e.g Beuther et al. 2002a). Observational properties of disks around O-B stars are reviewed by Zhang (2005) and Cesaroni et al. (2007).

In the view of formation of massive stars via disk accretion, matter is accreted from the outer mass reservoir onto the rotating disk. Matter in-falling from the massive core on the disk structure have to be processed quickly onto the central star. This has to be achieved by efficient transport of angular momentum. Various observations have shown that the massive *pseudo disks* are gravitationally unstable (see Cesaroni et al. 2007 and references therein). In such a state, matter can be efficiently accreted via gravitational torques. However, these observations could only access outer colder parts of the flattened structure. This leads to an interesting problem regarding the processing of such rapid flows of matter by the inner *hot* disk.

We begin with a detailed description of physical and numerical model considered for our study. Further, we discuss the effects of physical self-gravity with varying disk thermodynamics. Finally, we provide an outlook about future simulations planned for this work.

5.2 Physical Model

In the last decade, massive star formation has been vastly studied using numerical simulations (Yorke & Sonnhalter 2002, Krumholz et al. 2007, 2009, Kuiper et al. 2010a, 2011, Peters et al. 2010). These simulations either start with a rotating or a turbulent molecular core in either two or three dimensions. The massive core is then allowed to gravitationally collapse and evolve until it forms a central massive star or a binary system. Such an evolution of the core was studied with radiative transfer and self-gravity. The formation of flattened rotating structures are also seen in these simulations. Krumholz et al. (2009), using a core of mass 100 $M_{\odot}$, have shown evidences of large spiral arms and fragmentation in the rotating structure. These flattened rotating structures eventually collapse to a system of massive binaries with masses of 40 $M_{\odot}$ and 29 $M_{\odot}$. The strong radiation pressure drives a bipolar outflow, which forms a low density cavity/bubble. The gas in spite of seemingly strong hinderance from central radiation pressure continue to infall along the walls of the bubble. Kuiper et al. (2011) also obtained a similar qualitative result using a more accurate treatment of radiative transfer. However, no evidence of fragmentation were seen in their simulations.

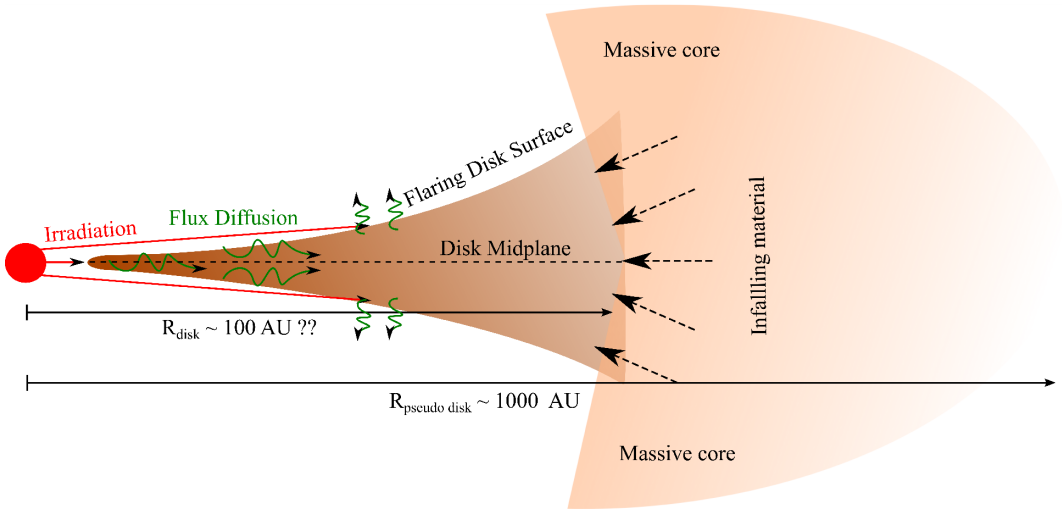

Figure 5.1: Physical model setup for inner accretion disk around young massive star. The inner edge of the disk is irradiated by the central star. The stellar light diffuse in the disk via flux limited diffusion on interaction with optically thick dust and gas. The outer edge ($\sim$ 100 AU) of the disk is being fed with matter at a very rapid rate $\sim 10^{-3} - 10^{-5}$ $M_\odot$ yr^{-1} from the massive core (or outer flattened rotating structure)

Simulations that study the collapse of a massive core are limited by resolution particularly in the innermost regions. Mostly, these simulations have an inner sink cell of 10-100 AU. This implies that the dynamics of gas is not followed inside the inner 10-100 AU. This inner region is of critical importance as it reveals the final fate of accretion of the gas on to the central star. Also, regions very close to the central star play a critical role in dynamics of outflows (see Chapter 4). In the present model, we would concentrate onto the dynamics of such an inner region of massive accretion disk. We do not aim to follow the complete evolution of a massive core, but focus on the inner disk. The main questions we would like to answer are as follows -

- How does the inner accretion disk react on being fed rapidly with large amounts of matter from the massive core.
- What role does the radiation from the central luminous star play in controlling the flow of matter through the disk.

Our model consists of two components : (i) the central massive star and (ii) an accretion disk extending to 120 AU which is being fed by matter from the outer massive core.

The central massive star of mass M_*, luminosity L_* and radius R_* does not evolve throughout the simulation. It is placed inside the inner spherical boundary and simply a source of central gravity and radiation. The region between the stellar surface and the inner boundary is assumed to be

optically thin ($\tau << 1$) for the stellar irradiation. A hybrid scheme for the radiation field (Murray et al. 1994, Edgar & Clarke 2003) has been expanded for the multi-dimensional radiation transport module. The radiation transport is split into two components. The ray tracing method is used to calculate the first absorption of the photon from the stellar surface and then the flux is evolved using the FLD approximation. In other words, the rays from the central star would travel freely until the medium becomes optically thick and is absorbed. Beyond the optically thick region the flux from the stellar irradiation is diffused into the disk.

The disk dynamics are studied in presence of a multi-physical setup. The relevant physical modules included in our model are listed below -

- Hydrodynamical evolution of the disk.
- Self-gravity of the massive disk.
- Irradiation from the central star (streaming from the inner optically thin sink boundary).
- Radiative transfer through the disk material via flux-limited diffusion.

The aim of the present study is to dynamically evolve a three-dimensional (3 D) accretion disk in presence of the above physical modules. In order to reach the final goal, we proceed in steps and include each module one-by-one and comprehend its influence.

To begin with, we study the interplay of self-gravity and thermodynamics of the disk. The criteria for gravitational instability and fragmentation largely depends on the thermal structure of the accretion disk (see Sect. 2.3.2). This notion is currently under investigation for forming giant planets around low-mass stars (see review by Durisen et al. 2007). In case of young massive stars, this could be important from the point of view of multiplicity. Usually, massive stars are found as a close multiple system in a cluster. The fragmentation in the disk of the most massive star could explain such a phenomenon.

The fragmentation in the disk could be avoided (or delayed) if it is efficiently heated. In our previous work (Vaidya et al. 2009), we have shown that the viscous heating is a dominant process and could avoid fragmentation in the disk inside of 100 AU. The heating process due to central stellar radiation was treated in a very simplified manner. Here we would like to consider the heating consistently via full radiative transfer calculations. However, we will not consider the effect of viscosity for the first calculations presented in this chapter. The angular momentum transport is governed by gravitational torques.

In the following section, we will discuss the basic equations that the code solves. Most importantly, we address the technique of implementing each of the physical modules in the standard PLUTO code.

5.3 Method

The dynamics of the inner accretion disks around young massive stars are studied in view of the following radiation-hydrodynamical (RHD) equations (Kuiper et al. 2010b) -

$$\frac{\partial \rho}{\partial \mathrm{t}} + \nabla \cdot (\rho \vec{u}) = 0, \tag{5.1}$$

$$\rho(\frac{\partial \vec{u}}{\partial t} + (\vec{u} \cdot \nabla)\vec{u}) = -\nabla P + \vec{f}, \tag{5.2}$$

$$\frac{\partial}{\partial t}(E) + \nabla \cdot [E + P]\,\vec{u} = \vec{u} \cdot \vec{f} - \nabla \vec{\mathcal{F}}_{\rm tot}, \tag{5.3}$$

$$\frac{\partial}{\partial t} E_{\rm R} + f_{\rm c} \nabla \cdot \vec{\mathcal{F}}_{\rm tot} = \mathcal{H}. \tag{5.4}$$

Comparing to the standard HD equations (see Table A.1), the above set of equations has an additional equation (5.4), which governs the evolution of the radiation energy density. Note that E is *not* the specific total energy as the factor of density is absorbed within. The internal energy density $E_{\rm int}$ that contributes to the total energy can be related to the gas pressure P via equation of state $(\gamma - 1)E_{\rm int}$, where γ is the adiabatic index.

The collection of all the source terms in the momentum equation is represented by a force density, $\vec{f}$. The exact form of $\vec{f}$ depends on the physical modules included for solving the problem and for the current problem it is given by

$$\vec{f} = -\rho \nabla \Phi - \mathcal{L} \nabla E_{\rm R} - \nabla \cdot (\vec{F}_*/c)\hat{r}. \tag{5.5}$$

The gravitational potential includes the central star and the self-gravitating massive disk - $\Phi = \Phi_* + \Phi_{\rm sg}$. The potential associated with self-gravity is,

$$\nabla^2 \Phi_{\rm sg} = 4\pi G \rho. \tag{5.6}$$

The PLUTO code has a module that handles the central gravity (i.e. Φ_*). Additionally, a Poisson solver has been implemented as a separate module to study the effects of self-gravity. This module basically solves the equation (5.6) using the diffusion ansatz. This algorithm involves solving a matrix equation via matrix inversion using standard iterative methods (Kuiper et al. 2010a).

The acceleration due to radiative forces has contributions from the thermal radiation pressure and irradiation from the central star. The term that corresponds to the acceleration due to the radiation pressure depends on the flux limiter $\mathcal{L}$, which is prescribed according to Levermore &

Pomraning (1981). The total flux $\vec{\mathcal{F}}_{\rm tot}$ comprises the *gray* thermal radiation flux $\vec{\mathcal{F}}$ and stellar irradiation flux $\vec{\mathcal{F}}_*$.

The frequency dependent stellar irradiation depends on the optical depth $\tau(\nu, r)$ along the radial distance r as it traverses from the central star (with radius R_*) through a density distribution,

$$\vec{\mathcal{F}}_*(\nu, r)/\vec{\mathcal{F}}_*(\nu, R_*) = (R_*/r)^2 \exp(-\tau(\nu, \mathrm{r})). \tag{5.7}$$

The optical depth in addition is a function of the density and the opacity.

The evolution of the radiation energy density (equation 2.66) derived from the first principles in Chapter 2 is written in a more general form using equation (5.4). All sources and sinks of energy are represented by $\mathcal{H}$. The expression of the factor $f_{\rm c}$ is obtained by combining the equations that controls the temporal evolution of the internal energy density $E_{\rm int}$ and radiation energy density, $E_{\rm R}$. In doing so, we obtain $f_{\rm c} = (c_{\rm V}\rho/(4aT^3) + 1)^{-1}$.

In Chapter 2, the relation between the radiative flux density and energy density was derived mainly for optically thick regions ($\tau >> 1$, see equation 2.65). This relation forms the basis of the flux-limited diffusion. In numerical problems we encounter optically thin as well as optically thick regions. Thus, for the FLD module in the code, a more general form of equation (2.65) is implemented. In the code, the radiation flux density is given by -

$$\vec{\mathcal{F}} = -D\nabla E_{\rm R}, \tag{5.8}$$

where $D = \mathcal{L}c/\kappa_{\rm R}\rho$ is the diffusion coefficient. The Rosseland mean opacity, $\kappa_{\rm R}$ is defined in Sect. 2.4.1. The form for the flux limiter $\mathcal{L}$ implemented in the code is,

$$\mathcal{L} = (2 + R)/(6 + 3R + R^2), \tag{5.9}$$

where $R = |\nabla E_{\rm R}|/(\rho\kappa_{\rm R}E_{\rm R})$. This form of the flux limiter ensures that the radiative flux density becomes either $\vec{\mathcal{F}} = -cE_{\rm R}\nabla E_{\rm R}/|\nabla E_{\rm R}|$ for highly optically thin region (free-streaming limit) or $\vec{\mathcal{F}} = -c\nabla E_{\rm R}/(3\rho\kappa_{\rm R})$ when the region is optically thick (diffusion limit).

The flux due to stellar irradiation $\vec{\mathcal{F}}_*$ depends on the mass and the luminosity of the central star. The final temperature of the dust can be obtained by taking into account the contributions from the thermal radiation flux $\vec{\mathcal{F}}$ and the stellar irradiation flux $\vec{\mathcal{F}}_*$. This final temperature is calculated using the following equation,

$$aT^4 = E_{\rm R} + \frac{\kappa_\nu}{\kappa_{\rm P}}\frac{\vec{\mathcal{F}}_*}{c}. \tag{5.10}$$

Here $\kappa_{\rm P}$ is the Planck mean opacity defined in Sect. 2.4.1 and κ_ν is the frequency dependent opacity. The speed of light is c and a is the radiation constant. Standard serial and parallel performance tests for the radiative transfer module has been done and described in Kuiper et al. (2010b). Also, detailed comparison with existing Monte-Carlo codes have shown robust results.

5.4 Numerical Setup

The major goal of this ongoing work is to comprehend the dynamical evolution of the inner accretion disks around young massive stars. In the present section, we will briefly explain the grid setup along with the initial and boundary conditions. The simulations are carried out using the hydrodynamics module of the PLUTO code (Mignone et al. 2007). The standard hydrodynamical equations are solved in presence of radiative transfer and self-gravity (equations 5.1-5.7). The implementation of the additional modules of radiative transfer and self-gravity in the code is described in the section above (Sect. 5.3).

5.4.1 Grid Setup

The dynamics of an accretion disk around a central massive star is numerically investigated in three dimensions (in some cases axisymmetric two dimensions) using spherical coordinates (r, θ and ϕ). The mid-plane of the disk lies at $\theta = 90^\circ$ in these coordinates. We have modelled the system in both hemispheres, i.e. the θ values range from 9° to 171°. This range of θ values are resolved with an uniform grid having 64 (or 32) cells. The disk is also uniform in the azimuthal direction. We cover the full range of $2\,\pi$ for the disk with 64 cells.

An important aspect of the disk is its scale height. In realistic simulations, one has to ensure that the scale height in the disk is well resolved. In all our simulation runs, the initial disk scale height is a linear function of its radius and the constant of proportionality is 0.1. This implies that the disk scale height is well resolved with 3 cells for runs with 64 cells in θ direction.

The radial extent of the disk is resolved using a logarithmically expanded grid with 128 (or 64) cells. In the present setup, we model the disk from 1 to 120 AU. Logarithmically expanded grids have an advantage over an uniform grid particularly in the radial direction. The bulk of disk dynamics in the radial direction originates from the inner region. Thus it is imperative to have high resolution in the inner radial regions. The logarithmic grid using 128 cells allows us to resolve the inner-most regions much better as compared to a uniform grid with the same number of cells.

5.4.2 Initial conditions

Here, we describe a fiducial model for an accretion disk around a young massive star. We chose to model the disk from 1 AU which physically could be the inner disk radius (or inner jet launching radius, see Sect. 4.2). This disk is surrounding a central massive star of mass 10 $M_\odot$, radius of

Table 5.1: Summary of disk simulations

Runs [a]	Dims.	Physical Size [Grid size [b]]			Physics [c]	EOS [d]
		r [e]	θ	ϕ		
SGIso	3	1 - 120 [128]	9° - 171° [64]	0 - 2π [64]	SG + HD	Isothermal
Rad1	3	1 - 120 [64]	9° - 171° [32]	0 - 2π [64]	RAD	Polytropic
SGRad1	3	1 - 120 [64]	9° - 171° [32]	0 - 2π [64]	SG + HD	Polytropic
Full2d1	2	1 - 120 [128]	9° - 171° [64]	Axisymmetric	RAD + SG + HD	Polytropic

[a]All the runs are done in a spherical grid.
[b]The radial grid is logarithmically expanding while the θ and ϕ grid are uniform for all runs.
[c]Different physical modules are abbreviated as follows - HD : Hydrodynamics, SG: Self gravity, RAD : Radiation.
[d]Equation of state
[e]The radial range is 1 - 120 AU for all runs.

$R_* = 6\ \mathrm{R}_\odot$ and zero age main sequence (ZAMS) luminosity of $L_* = 5179\ \mathrm{L}_\odot$. This luminosity is the upper bound for a 10 $\mathrm{M}_\odot$ star. In our future runs we will adopt luminosity and size from a realistic model of massive star evolution (Hosokawa & Omukai 2009). The velocity $u_0 = \sqrt{GM_*/l_0}$, is the Keplerian velocity at the inner edge l_0. Its value turns out to be 94 $\mathrm{km\,s^{-1}}$ for the stellar mass considered here.

The disk is initially set to have a constant scale height to radius ratio of 0.1. The surface density of the disk is chosen to be $\Sigma = \Sigma_0/r$, where r is the spherical radius. The constant Σ_0 is proportional to the density scale at the inner edge of the disk. The value of the density scale can be obtained from our previous calculations using semi analytical modeling of thin disks around massive stars (Vaidya et al. 2009). The density at $l_0 = 1$ AU is estimated to be in the range of $10^{-9}-10^{-8}\ \mathrm{g\,cm^{-3}}$. Alternatively, the value of Σ_0 determines the mass of the disk. Using the density of $10^{-8}\ \mathrm{g\,cm^{-3}}$, we obtain the mass of the disk to be 3.0 $\mathrm{M}_\odot$ and thus the disk mass to stellar mass ratio is 0.3. In the vertical direction, we choose that the disk density extends up to 5 scale heights. Beyond this there exists a non-rotating stationary corona with a density of $10^{-15}\ \mathrm{g\,cm^{-3}}$.

The rotation velocity at the mid-plane of the disk is slightly sub-Keplerian. This account for the force due to pressure gradient to support the disk in a radial balance. The form of u_ϕ prescribed in our simulation is given by

$$u_\phi = \sqrt{\left(\frac{1}{r}\left(1.0 - \frac{3H_0^2}{\sin\theta}\right)\right)}. \tag{5.11}$$

Here, H_0 is the constant scale height to radius ratio of 0.1.

The most important initial quantity that has to be prescribed is the temperature profile (or sound

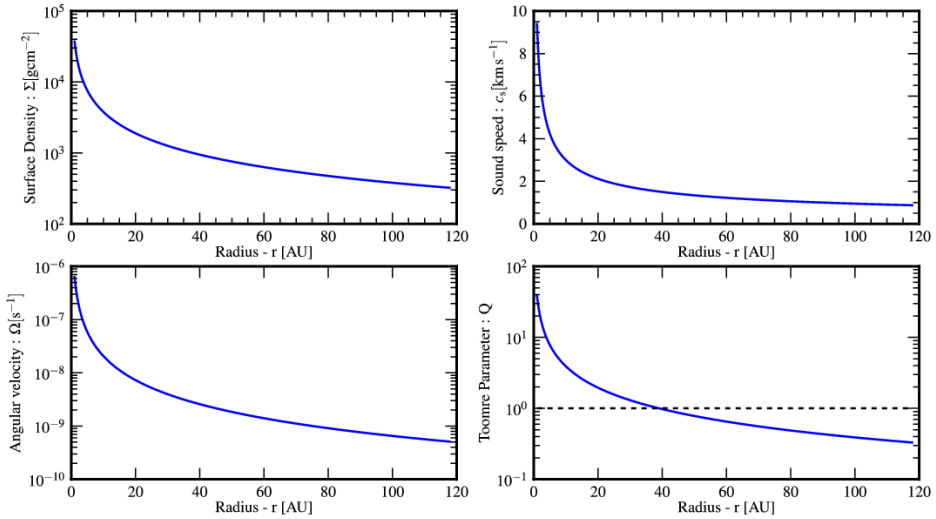

Figure 5.2: Initial radial profiles of various disk quantities for run SGIso. All the physical quantities are obtained after vertical averaging over the disk scale height. The *dashed line* in the curve of Toomre parameter marks the region of gravitational instability.

speed) in the disk. We will vary the temperature profile in the disk for the runs described in this chapter. This will help to study the evolution of the disk density structure in presence of changing thermal structure.

For our run SGIso (see Table 5.1), we have chosen an isothermal equation of state. In such a case, the thermal pressure is linearly related to the density, $P = \rho c_s^2$, where the sound speed has the following radial profile

$$c_s = \frac{H_0}{\sqrt{r \sin\theta}}. \tag{5.12}$$

The choice of $H_0 = 0.1$ ensures that the value of sound speed at the inner edge is 9.4 km s^{-1}. This amounts to a temperature in the mid-plane of $\sim 10^4$ K at 1 AU. Such a profile of sound speed would remain constant along the vertical direction and the disk is *locally isothermal*.

In the other run SGRad1, the initial temperature profile is derived consistently from *pure* radiation run Rad1. The pure radiation run Rad1 is described in details in Sect. 5.5.1. In this run, only the thermal pressure of the disk is evolved via radiative transfer calculations. The disk is kept stationary throughout this run. The irradiation from the central star and the appropriate flux diffusion in the disk will heat and cool the disk eventually determining the final thermal structure of the disk. Thus, by *pure* radiation, we mean that only the thermal structure of the disk is allowed to evolve without any hydrodynamical or self-gravitational feedback.

With the above choice of profiles of various disk quantities for the run SGIso, we can estimate the initial radial profile of Toomre parameter which is defined by (also see equation 2.46)

$$Q(r) = \frac{c_s(r)\Omega_{epi}(r)}{\pi G\Sigma(r)}. \tag{5.13}$$

In case Keplerian rotation, $\Omega_{epi} \approx \Omega_{kep}$. We obtain the initial radial profile with $Q(r) \sim 1/r$ with $Q_{min} = 0.3$ at r = 120 AU. Thus, the disk is gravitationally instable right from the beginning which makes it suitable to transport matter and fragment. The initial profiles of disk quantities pertaining to the run SGIso are shown in Fig. 5.2

5.4.3 Boundary conditions

Boundary conditions form an integral part of numerical simulations. A careful investigation of the boundary effect is imperative. Since the accretion disk considered for the present setup evolves in a multi-physical environment, we need to prescribe boundary conditions for variables appearing in each of these modules. For our 3 D setup we have to deal with six boundaries (two for each r, θ and ϕ).

In case of hydrodynamical setup, the boundaries at θ_{min} and θ_{max} are chosen to be outflow. Boundaries for the azimuthal direction are periodic. The radial boundaries are crucial as they are associated with the accretion flow in the disk. The problem requires the disk to be continuously fed with mass. Thus, we choose an inflow boundary at the outer radius of the disk. The matter is forced to inflow from the outer boundary with a velocity derived from a steady accretion rate of 10^{-3} $M_\odot\,yr^{-1}$. We essentially copy the density from the last grid cell. Using this density and a steady mass accretion rate, we derive the velocity of the inflow. A zero gradient is used for the pressure and the rotational velocity is extrapolated from the disk into the boundary. At the inner edge, we prescribe boundary conditions to allow the matter to accrete onto the central star.

In runs involving self-gravity, proper boundary conditions need to be prescribed for the self gravitating potential Φ_{sg}. The values of Φ_{sg} at the inner radial and θ_{min} and θ_{max} boundaries are obtained using zero gradient between the ghost cells and last grid cell. Periodic values are prescribed in the azimuthal direction. The self gravitating potential at the outer radial boundary is determined by a multipole expansion as derived by Black & Bodenheimer (1975),

$$\Phi_{sg,bound} = -G\sum_{l=0}^{\infty}\left(\frac{P_l(\cos\theta)}{r^{l+1}}\left[\int_{V'}\rho(r',\theta')r'^{l}P_l(\cos\theta')dV'\right]\right), \tag{5.14}$$

where $P_l(\cos\theta)$ are Legendre polynomials of order l. On account of assumed spherical symmetry, it can be shown that all odd moments vanish and only even moments survive. In our case we go up to fourth order (i.e. l = 4).

The radiation energy density has to be prescribed in the boundaries when dealing with the radiative transfer module of the code. For the present setup, we have chosen Dirichlet boundaries for the inner radial boundary. We prescribe a constant Dirichlet temperature ($T_{\rm diri} = 20\,K$) at these boundary. Using this temperature the radiation energy density in the boundary zones is determined using $E_{\rm R,bound} = aT^4_{\rm diri}$. A zero gradient of the radiation flux is used for the outer radial boundary. While for the boundaries in θ directions, zero gradient of the radiation energy density is applied. This ensures that no flux is allowed over this interface.

5.5 Results and Discussions

Our basic approach is to evolve the 3 D self gravitating disk which is perturbed by injecting mass from outer boundary. Further, we investigate the nature of instability by modifying the thermal structure in the disk. The run SGIso (see Table 5.1) is a run including self gravity and hydrodynamics assuming a locally *isothermal* disk. For the run SGRad1, the temperature profile is self consistently estimated via pure radiative transfer calculations (run Rad1).

5.5.1 Estimating the Disk Temperature

The thermal structure of the disk plays a vital role in determining the evolution of the disk. The spectral profile of the disk is also governed by the thermal structure of the disk. The disk can be heated by many sources like viscosity, stellar irradiation, reprocessed star light by the dust, cosmic rays, shocks etc.

We aim to consistently derive a temperature structure of the disk density profile. The heating and cooling is mainly due to radiation transport. We have performed a low resolution 3 D run - Rad1 which essentially derives the temperature profile in the disk. The initial surface density of the disk is given by $\Sigma = \Sigma_0/r$ and the initial temperature throughout the disk is constant and set to T=20 K. The initial disk mass is set to $\sim$ 3 $M_\odot$ around a central mass of 10 $M_\odot$. The idea is to derive the steady temperature profile for such a density distribution in presence of heating due to stellar irradiation and without any compression due to hydrodynamical effects.

The mean opacities used for this pure radiative calculation are obtained from Semenov et al. (2003). The time series of temperature at the mid-plane is shown in Fig. 5.3. A striking peak in the temperature profile is seen for $N_{\rm rot} = 1$ as the temperature reaches $\sim 10^4$ K from 20 K in the first grid cell. This is an effect of strong stellar radiation. In addition the outer disk surface is also exposed to the central stellar radiation as it streams through the optically thin corona.

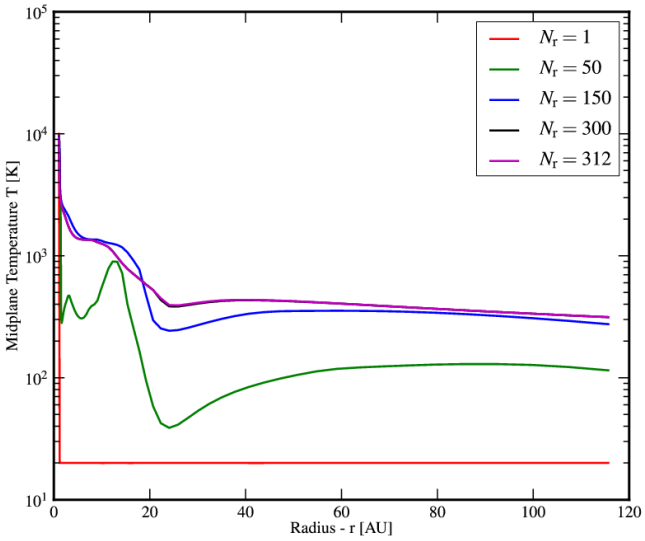

Figure 5.3: Evolution of the temperature along the mid-plane in the disk for run Rad1. In this *pure* radiation run, only the thermal structure of the disk is evolved due to influence of radiation transport from a central star with mass 10 $M_\odot$. The colors represents number of inner disk rotations as shown in the key.

The disk region just behind the first cell would see this cell as a source of radiation. Based on the optical depth, the flux will either stream or diffuse along the density distribution to achieve a steady and consistent temperature profile. The criteria for the radiative diffusion solver to converge is set as the relative decrease in the residual norm is $< 0.1\%$. Gradually, the flux from the inner cell diffuses into the disk, causing it to heat up. Along with FLD in the mid-plane, the disk is also heated as part of the flux diffuses from the surface to the interior. This is seen as a bulge in the temperature profile at the outer parts of the disk. Eventually, the steady state profile of the temperature is obtained after $N_{\rm rot} \sim 310$. Beyond this state no further evolution of the temperature profile is observed.

This steady state temperature profile for the prescribed disk density obtained in a presence of a central star with mass $M_* = 10\ M_\odot$ is used as an initial condition for run SGRad1.

5.5.2 Effects of Self Gravity

We describe our reference run, SGIso, which includes hydrodynamics and self-gravity. The initial setup of the disk for this run is described in Sect. 5.4.2. The disk is *locally isothermal* and the heating from the viscous effects are neglected. The mechanism that is responsible for the transfer of matter is simply, gravitational instability. The snapshots of the density in the r-θ and

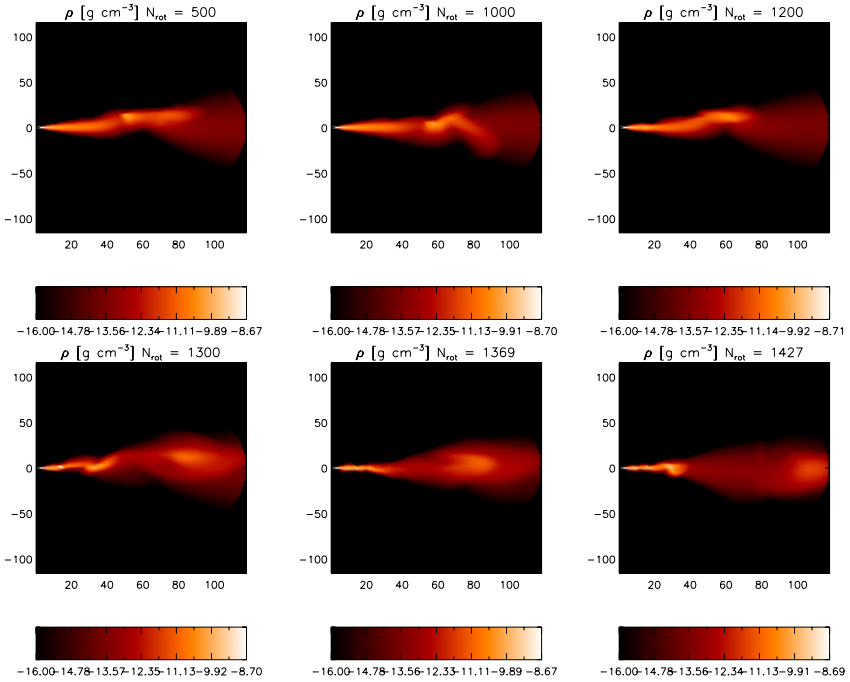

Figure 5.4: Time snapshots of the logarithmic values of the density at $\phi = 57°$ in the r-θ plane.

r-ϕ plane of the disk are shown in Fig. 5.4 and Fig. 5.5 respectively.

At the beginning, the disk was set in balance with gravity, centrifugal force and thermal pressure force. On adding the acceleration due to self gravity, the disk becomes unsteady. The disk in this phase forms regions of high and low density *or rings* as seen in Fig. 5.5. This is a transient phase of the disk evolution. The disk is continuously fed with a steady mass accretion rate of $\sim 10^{-3}$ $M_\odot\,yr^{-1}$ from the outer $X1_{END}$ boundary as shown in Fig. 5.6. As the matter is added on to the disk, its surface density, $\Sigma(r)$, increases and the radial value of the Toomre parameter, $Q(r)$, steadily approaches unity. A spiral arm is developed in the disk after about 1200 inner disk rotations (see Fig. 5.5). The gravitational torques produced due to formed spiral arms transfer the angular momentum and thus distribute matter in the disk. After 400 years (one orbital time at the outer disk radius of 120 AU), the disk begins to fragment forming short lived clumps particularly close to the inner edge (see Fig. 5.4). This leads to enhanced accretion rate on to the star ($X1_{BEG}$ boundary) as seen from Fig. 5.6. The spikes seen in the mass accretion rate are due to rapid in-falling of very low mass clumps on the star. When the disk reaches this *gravo-turbulent* stage matter is also seen to move out from the disk. The mass flux leaving the outer boundary is shown as a *green* line in the bottom panel of Fig. 5.6.

In the end, the disk settles into a state with two large spiral arms that distribute matter in the disk. The evolution of the disk mass is shown in Fig. 5.7. After $\sim$ 400 years, about 0.03 $M_\odot$ of mass is added onto the star, while about 0.35 $M_\odot$ is added onto the disk. Thus, we see an efficiency

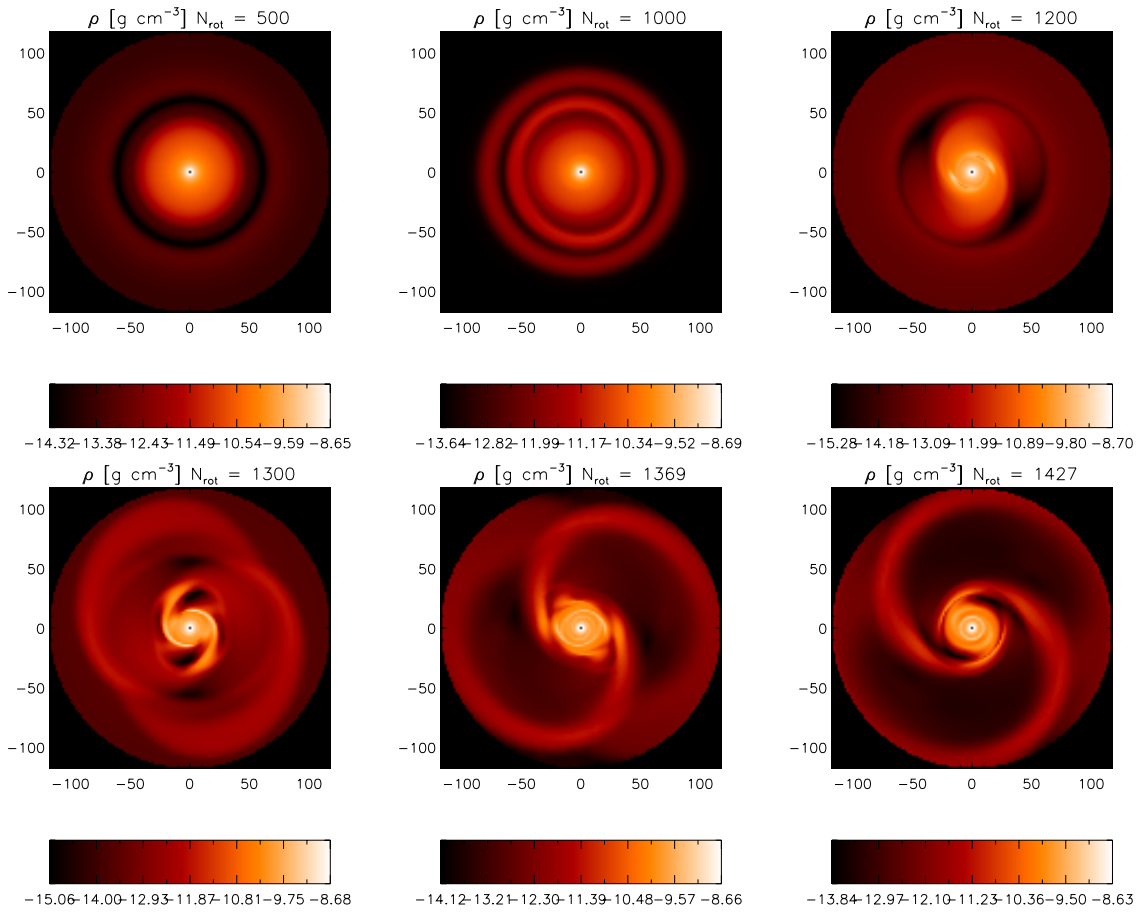

Figure 5.5: Time snapshots of the logarithmic values of the density at the disk mid-plane in the r-ϕ plane.

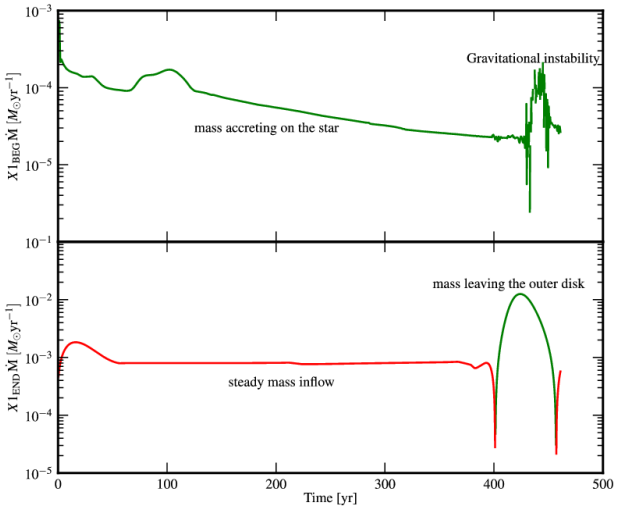

Figure 5.6: Mass flux leaving the inner boundary $X1_{\rm BEG}$ on to the star is shown om the top panel. The *bottom* panel shows the mass entering [*in red*] and leaving [*green*] the domain from the outer boundary.

of 0.1 in mass transfer for this simulation. Hence, in absence of any viscous heating source, a locally isothermal disk with initial minimum Toomre parameter < 1, develops large spiral arms and also fragments leading to a gravo-turbulent stage.

The condition for a disk to fragment depends on the cooling time (see equation (2.48) of Chapter 2). For an isothermal disk the cooling time is ideally zero, which is much shorter than the dynamical time in the disk. Hence, isothermal conditions make the disks most vulnerable to fragmentation. This is also seen in simulations which study giant planet formation (e.g. Rafikov 2005, Durisen et al. 2007).

We have also performed a run, SGRad1, where we evolve the disk in an adiabatic setup. This run is similar to the initial setup of SGIso run, with a difference only in the temperature profile. The initial temperature profile for the run SGRad1 is derived via pure radiative simulation as described in Sect. 5.5.1. A comparison of the initial radial profile of the vertically averaged sound speed for runs SGIso and SGRad1 is shown in Fig. 5.8. A significant deviation from the locally isothermal sound speed profile is seen particularly at the outer parts of the disk. However, the two profiles are similar near the inner edge of the disk.

In the run SGRad1, the disk is evolved in presence of hydrodynamics and self-gravity but with an initial temperature profile which is estimated consistently from pure radiative transfer runs. We see significant changes in the outcome of both of these runs. One of the striking difference between these runs is seen in the radial profile of the Toomre paramater after 300 years (see

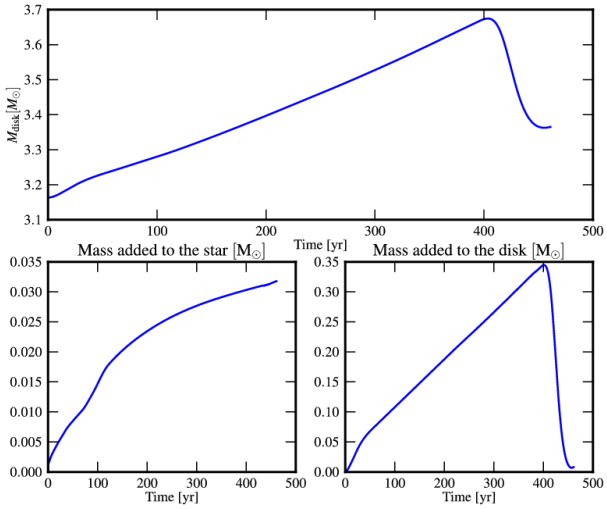

Figure 5.7: The *top* panel shows the evolution of the total disk mass. This disk is being fed from outer (massive core) boundary at a constant rate. The mass is also accreted from the inner boundary, however, the mass accreted on to the star is 0.1 times mass added to the disk.

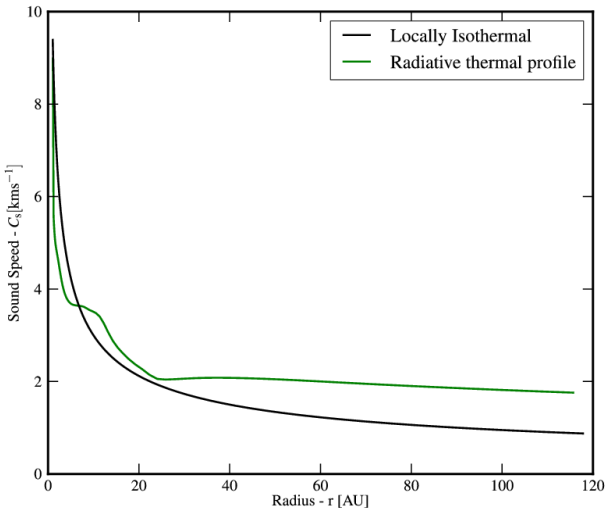

Figure 5.8: Comparison of initial vertically averaged sound speed for runs SGIso and SGRad1. The *black* line is the radial profile for a locally isothermal setup in run SGIso, and the *green* line is obtained after pure radiative run described in Sect. 5.5.1. The initial temperature for the run SGRad1 is obtained from the *green* line.

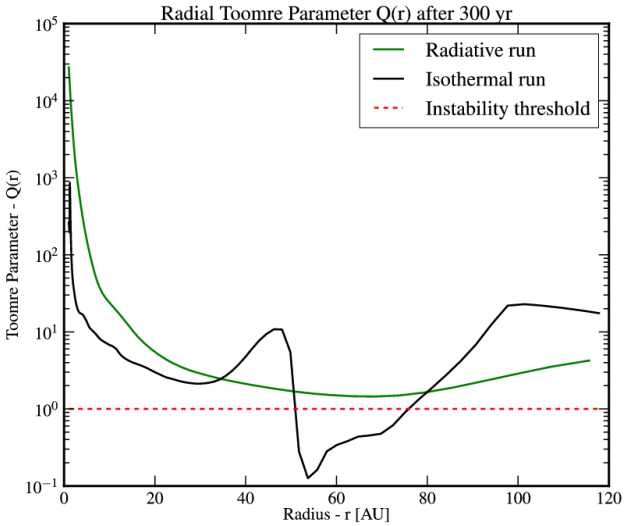

Figure 5.9: Radial variation of the Toomre parameter for runs SGRad1 (*green line*) and SGIso (*black line*) after 300 years. The *red dashed line* marks the threshold of the gravitational instability in the disk.

Fig. 5.9). The value of $Q(r)$ never falls below the threshold value of unity for the run SGRad1. While, the Toomre parameter is well below unity for the run with isothermal conditions. Even in run SGRad1, we do not find any signatures of fragmentation. The reason could be either physical or numerical.

The ability of the disk to efficiently cool down controls the amount of fragmentation in the disk. The cooling time for the simulation run SGRad1 with adiabatic index $\gamma = 5/3$ is not zero as is the case with an isothermal disk. Absence of fragmentation in the disk would imply that the cooling time is longer than the dynamical time. Also, the most unstable wavelength in an self-gravitating disk is proportional to its scale height ($\lambda_{\rm m} \propto 6H$). The effects of gravitational instability can be seen if at least the most unstable wavelength is resolved. Since the run SGRad1 has half the number of cells in radial and vertical directions as compared to SGIso, we do not resolve the scale height of the disk sufficiently.

If we simply apply the equation (3.13) to calculate the cooling time, we find short cooling times that should fragment the disk. Thus, it follows that the low resolution of the run hides the physical nature of fragmentation. Nevertheless, we see accretion of matter within the disk due to gravitational torques. One needs to perform high resolution runs to investigate this fact in more detail. This is what we intent to do in the near future.

5.6 Summary : Massive Disks

In this chapter, we have shown first results obtained en route to understand dynamical evolution of inner disk around a young massive star. We address this problem using three dimensional hydrodynamical simulations of an accretion disk in presence of radiative transport and self gravity. In particular, we have discussed the role of stellar irradiation and flux limited diffusion in shaping the thermal structure of the disk. Additionally, we have described hydrodynamical evolution of the self- gravitating disk with different thermodynamics.

Our first results indicate that the disk with mass $\sim$ 3 $M_\odot$ around a 10 $M_\odot$ star would develop large spiral arms and fragment after about 400 years. Such a disk was fed with mass from the outer boundary at a steady rate of 10^{-3} $M_\odot\,yr^{-1}$ and was evolved with an isothermal equation of state. As the disk fragments into small clumps, they either accrete onto the star or leave the domain from the outer boundary. We find an accretion efficiency of 10%. In summary, a locally isothermal disk would develop spiral arms and fragment as it is fed with a steady mass flow from the massive core (outer boundary). The low resolution run, SGRad1, however does not show any signatures of fragmentation. The differences in these runs lies in the resolution and the initial thermal structures. Also, the disk in the run SGRad1 is evolved using an adiabatic equation of state.

In principle, radiation pressure from a young massive star could influence the thermal structure of the inner accretion disk. This influence on the thermodynamics of the inner disk could play an important role in its dynamical behavior. The impact of radiative transfer on a self gravitating disk is currently under investigation. In Table 5.1, one of the first runs, Full2d1, that includes all three modules is listed. However, this is done in an axisymmetric setup and a reflective boundary is applied at the outer edge. This run basically allows the disk to reach an equilibrium state in presence of self gravity and radiation effects. The axisymmetric profiles for each of the physical quantities would then be projected into three dimensions and used as initial conditions to further study the dynamics of these inner regions around young massive stars.

We summarize that in the absence of any viscous heating, gravitational instability could transfer matter in a locally isothermal massive disk which is fed from outer core. However, in this case only 10% of the mass added onto the disk is accreted onto the central star.

There are in fact two things, science and opinion; the former begets knowledge, the latter ignorance.

Hippocrates (460 BC-370 BC)

6

Summary and Outlook

6.1 Summary

Massive stars play a crucial role in shaping the ISM by injecting mass and energy throughout their short life time. The main focus of this thesis was to understand the dynamics of inner regions (< 100 AU) around young massive stars. The thesis follows the notion that massive stars form in a similar fashion like low mass stars. However, the scales involved are different than their low mass counterparts. The formation of young massive stars via disk accretion involves numerous physical phenomena particularly close to the central star. Among them the important ones are, (i) radiation pressure from the central luminous star, (ii) powerful molecular outflows, (iii) strong stellar winds, (iv) magnetically driven jets and (v) rapid accretion via a massive disk. This thesis has investigated the interplay between these processes using a semi-analytical and numerical approach.

In the following, I will summarize the important findings of this thesis. I will begin with results from the semi-analytic modeling of the inner accretion disk using proper gas and dust opacities around young massive stars. Further, I will discuss the interplay of magneto-hydrodynamics and radiation force in the perspective of jet formation from young massive stars. I will then discuss first results from a full three dimensional modeling of inner accretion disk improving the previous semi-analytic model. Finally, I will outline future pathways that can be developed from the results presented in this thesis.

A Global accretion disk model around young massive stars - semi-analytic approach

The inner most regions around a young massive star have high extinction ($A_V \sim$ 100-1000 mag) and thus observing them is difficult. As a result, most of the physical quantities for these inner regions are not known (e.g density, temperature). For understanding the interplay between var-

ious physical processes it is therefore imperative to have an estimate of these quantities in such inner regions. In doing so, we have adopted a steady state standard disk model for accretion disks around a luminous high-mass star. We have essentially solved a set of steady accretion disk equations with proper gas and dust opacity. Implementing proper opacities is a crucial step as the influence of radiation pressure on disks around massive stars is of critical importance. In particular we have considered Rosseland mean dust opacities given from Ruden & Pollack (1991) and the gas opacities from the OPAL opacity tables (Iglesias & Rogers 1996). The analysis not only provided a measure of physical quantities in the region close to the central luminous star but also provided a link between the inner region and observationally accesible outer parts of the disk.

In view of this semi-analytic calculations, we found high temperatures ($\sim 10^5$ K) in the mid-plane of the disk around stars with mass $10\,M_\odot$. The major implication of such high temperatures is seen in the radial distance of the dust sublimation front from the central star. The main finding from this work is the *self-sublimation* of the dust at a much larger radii then caused from the stellar irradiation. Efficient transport of angular momentum is required to transfer matter at rates of $10^{-3} - 10^{-5}\,M_\odot yr^{-1}$, typically seen in disks around young high-mass stars. A highly turbulent disk would ensure such an efficient transport of angular momentum. In our models, we have prescribed turbulence in the form of standard α_v viscosity. We found that the heating in the mid-plane is dominated by viscous effects and the temperature reaches 1500 K around 10 AU from the central star of ten solar mass. At this temperature most of the dust grains sublimate and the disk is now simply gaseous. The *dust sublimation radius* obtained due viscous heating is three times higher than caused by heating from stellar irradiation alone.

Thus, we observed that the dust sublimates much further away from the central star using one-dimensional analysis for standard disk models and applying mean opacities due to dust and gas. Destruction of dust grains at large radii results in a significant reduction of opacity. This aided in an efficient accretion in the gas phase. The inner *hot* gas disk forms a launching base of the outflow. Hence, the stability of the inner disk is critical to achieve long-lasting outflows.

We have investigated the hydrodynamical stability of the disk using the physical quantities obtained from the above semi-analytical model. Inside 100 AU (around a $10\,M_\odot$ star), the disk is hot enough to resist gravitational instability. The cooling in the disk is very efficient for higher α_v values. We have proposed that inner disks are stable up to 100 AU to gravitational torques and fragmentation for $\alpha_v < 0.1$. The radial velocities estimated from typical values of steady mass accretion rates can be used to compute the ram pressure and further compare it with the radiation pressure from the central star. We found that the ram pressure wins over the radiation pressure in the inner stable region thereby proving the fact that radiation pressure is not important to halt accretion on to the central star. These results are published in Vaidya et al. (2009).

Jets around young massive stars : An interplay of magneto-hydrodynamics and radiation pressure

One-dimensional calculations to derive the physical quantities in the region close to the massive star provides a stable inner disk. Such a disk forms an ideal launching base for large scale molecular outflows. Powerful jets and molecular outflows are ubiquitous in massive star forming regions. In low mass stars, they are believed to be magnetically driven. The presence of magnetic fields around young massive stars is evident from maser and polarimetric observations. This points to the fact that even the jets from young high-mass stars could be magnetically driven. However, effects due to strong radiative forces have to be considered to study jet formation in these objects consistently.

To this end, we have done a numerical study of the interplay of MHD and radiative forces to explore the acceleration and collimation of jets for young high-mass stars. Our approach was to launch a pure magnetically driven jet from an underlying accretion disk until it achieves a steady state. Then, we switched on the radiative force from the central star or inner hot accretion disk to see its influence on the existing MHD jet. In our approach, we have considered the radiative line driving force derived using the Castor, Abbot and Klein approximation (CAK model).

Our main result from this work is that *the line driven force from the central star for the parameters considered does play a significant role in modifying the dynamics in terms of collimation and acceleration of the outflow.* For our reference run considering a $30\,M_{\odot}$ star, we found that the outflow velocity is increased by a factor of 1.5 - 2 by radiative forces as compared to the pure MHD flow. Typical values obtained are $\sim 200\,\mathrm{km\,s^{-1}}$. Also, the degree of collimation is decreased, visible as a 30%-change in the opening angle of the magnetic field lines.

To get a qualitative picture of the jet formation around young high-mass stars, we have investigated how the dynamics of the jet is altered by means of an extensive survey of physical parameters in our model. We have mainly varied three physical parameters - (i) the central stellar mass (or luminosity) (ii) the strength of the magnetic field and (iii) the line force parameter α, that governs the contribution of radiative acceleration from optically thick lines. We found that as the central mass of the star is increased, the radiative force also increases which causes the outflow to accelerate to high velocities and also make it morphologically wider. Weaker magnetic fields have less Lorentz force thereby reducing its effect in comparison to the radiative force. Thus jets launched in a weaker magnetic field environment are more de-collimated due enhanced influence of the radiative force as compared to jets with strong fields. The value of the line force parameter α gives a measure of self shadowed lines. A lower value implies fewer self shadowed lines that would result in efficient line driving force, which eventually leads to a wider and faster outflow.

Our results from this numerical study are in qualitative agreement with the *evolutionary sequence of massive outflows* put forward by Beuther & Shepherd (2005). On basis of this empirical

picture, the outflow becomes wider in shape as the mass (or luminosity) grows with time. Our numerical study has given a detailed physical understanding of this empirical trend.

Line forces due to the hot accretion disk do not play a significant role in controlling the dynamics of the MHD outflow, simply because they are orders of magnitude smaller than all other forces that affect the flow dynamically. Implementing high disk radiation forces (by taking into account the inner hotter part of the disk), has resulted into a flow in which intermittent shells are ejected typical of the so called *line driven instability*.

In summary, our study of the interplay between the magnetically driven jets and the radiative line driving force from the central star and underling hot disk has given a physical base to the qualitative evolutionary picture of outflows from young high-mass stars. These results are accepted for publication in the Astrophysical Journal (Vaidya et al. 2011).

The dynamics of massive inner accretion disk

The semi-analytic one-dimensional modeling of the disk provided a headway by estimating essential physical quantities in inner regions of young high-mass star. However, both the treatment of radiation and dynamics were highly simplified. A more realistic perspective of inner dynamics can be obtained in a full three-dimensional radiative transfer analysis. The ongoing numerical study of a massive disk inside of 120 AU aims to understand the evolution of disks with complex radiative transfer analysis. In addition, effects due to self gravity are also considered for this full 3D study of massive accretion disks around high-mass stars.

We aim to study the transport of material under the influence of radiation. The material is in falling at a rapid rate from the outer (outside of 120 AU) core onto the disk. In our initial attempts we assume that the transport of angular momentum is purely due to gravitational effects (no $\alpha_{\rm v}$ viscosity as used for 1D model). Our first results using an isothermal equation of state indicates the formation of spiral arms and fragmentation in the inner disk regions. We find vigorous transport of matter on to the star in form of *short lived clumps* (or fragments). This is expected as indicated by similar previous studies pertaining to planet formation by gravitational instability (e.g Rafikov 2005, Durisen et al. 2007, Meru & Bate 2010).

Our next step for this problem is to relax the isothermal assumption and consistently solve the disk hydrodynamics with radiative transfer effects. The results from the simulations will give important clues about transport of matter in realistic accretion disks around young high-mass stars. These results would also provide insight into the multiple nature of massive stars via disk fragmentation.

6.2 Future Work

Despite revolutionary progress in our understanding of massive star formation over the last decade, there are many fundamental questions that are yet unresolved. In particular, concerning the inner disk around young massive stars. These regions are difficult to understand from a theoretical as well as an observational point of view. High optical depths due to dust and gas makes it difficult to observe and thus obtain any constraints on essential physical quantities like the density, velocity etc. Theoretically, one has to include numerous physical processes that are present at these small scales. The work in this thesis was an attempt to study the interplay between the complex physical processes involved in such close by regions around young high-mass stars. However, the lack of observational constraints on the physical parameters leads to a huge parameter set to explore. Even though this thesis has included most of the important physical processes, some issues are yet to be integrated for a thorough numerical study as discussed here.

The detailed numerical study of the complex inter-relation of radiative and magnetic forces has confirmed the qualitative picture of outflows from young massive stars. While a complete analysis of jet acceleration and collimation was presented, the underlying accretion disk was treated as a boundary. In future, we would like to include consistently the disk and the central star inside the numerical domain for such a study. Also, it would be interesting to see the effects of stellar winds that might be important during the later stages of high-mass stellar evolution. These strong high-velocity stellar winds could as well contribute in deflecting the MHD driven jet leading to a wide angle outflow.

The ongoing disk simulations rely on the fact that transport of angular momentum is mainly due to gravitational torques. In our future study, we would like to also include effects to $\alpha_{\rm v}$ viscosity as carried out in our semi-analytical model. Such an inclusion could prove essential to transport matter in the inner most regions. The physical explanation for such a transport could be related to possible magneto-rotational instability. We also plan to perform post-processing routines on our disk simulations so as to give observers a template for the future observations with Atacama Large Millimeter Array (ALMA) and European Very Large Array (EVLA). The advent of ALMA would surely give better handle on some essential parameters at such scales which could be compared to results from the work presented in this thesis.

In a nutshell, our understanding concerning the dynamics of inner regions around young massive stars can be improved with following contributions from observers and modelers in the future.

- **Observations** -
  - Better constraints on the physical parameters from high resolution observations with future telescopes and interferometers.

- **Theory and Simulations** -
  - Modeling the impact of stellar winds on MHD driven outflow.
  - Launching large-scale outflows by consistently modeling a massive accretion disk.
  - Adopting full magneto-hydrodynamical radiative transfer calculations in studying the dynamics in these regions.

To summarize, this work has provided estimates of essential dynamical quantities for the launching base of jets from stars with mass $> 10\,M_{\odot}$, particularly the presence of high temperatures. Ongoing complex three-dimensional simulations will give direct clues for future observations. Numerical studies of jet formation from young high-mass stars has revealed the importance of the radiative force from the central star in controlling the acceleration and collimation of magnetically driven jet. Finally, I would conclude that this study has opened a new vista to the complex physics involved in the accretion and outflow processes around young high-mass stars and end with words from Max Planck :

Anybody who has been seriously engaged in scientific work of any kind realizes that over the entrance to the gates of temple of science are written the words : YE MUST HAVE FAITH !

A

Appendix : Basic Equations

Table A.1: Set of standard HD and MHD equations solved by the PLUTO code. [a]

Name	Equations
A. Hydrodynamics	
Mass conservation	$\frac{\partial \rho}{\partial t} + \nabla \cdot (\rho \vec{u}) = 0$
Momentum conservation	$\rho(\frac{\partial \vec{u}}{\partial t} + (\vec{u} \cdot \nabla)\vec{u}) = -\nabla P - \rho \nabla \Phi$
Energy conservation	$\frac{\partial}{\partial t}(\rho E) + \nabla \cdot \left[\rho E + P\right] \vec{u} = -\rho \nabla \Phi \cdot \vec{u}$
Total specific energy	$E = \epsilon + \frac{u^2}{2}$
Equation of state	$P = (\gamma - 1)\rho\epsilon$
B. Magneto-Hydrodynamics	
Mass conservation	$\frac{\partial \rho}{\partial t} + \nabla \cdot (\rho \vec{u}) = 0$
Momentum conservation	$\rho(\frac{\partial \vec{u}}{\partial t} + (\vec{u} \cdot \nabla)\vec{u}) = -\nabla P - \rho \nabla \Phi + \frac{1}{4\pi}(\nabla \times \vec{B}) \times \vec{B}$
Energy conservation	$\frac{\partial}{\partial t}(\rho E) + \nabla \cdot \left[\rho E \vec{u} + (P + \frac{B^2}{8\pi})\vec{u}\right] - \vec{B}(\vec{u} \cdot \vec{B}) = -\rho \nabla \Phi \cdot \vec{u}$
Total specific energy	$E = \epsilon + \frac{u^2}{2} + \frac{B^2}{8\pi\rho}$
Equation of state	$P = (\gamma - 1)\rho\epsilon$
Induction equation	$\frac{\partial \vec{B}}{\partial t} = \nabla \times \left(\vec{u} \times \vec{B}\right)$
Solenoidal condition	$\nabla \cdot \vec{B} = 0$

[a] In the above equations,

- ρ is the mass density which is related to pressure P through an equation of state with an adiabatic index γ.

- Φ is the gravitational potential.
- The total specific energy E comprises of the internal specific energy ϵ along with the specific kinetic energy which is related to the flow velocity $\vec{u}$ and in addition there a contribution from specific magnetic energy for the MHD module .
- The magnetic field in the ideal MHD equations is denoted by $\vec{B}$.

B

List of Symbols

Symbol	Description	CGS Units	Page Ref.
ρ	Gas density	$\mathrm{g\,cm^{-3}}$	16
P	Pressure	$\mathrm{dyne\ cm^{-2}}$	16
γ	Adiabatic index		16
Φ	Gravitational potential		16
$\vec{u}$	Fluid velocity field	$\mathrm{cm\,s^{-1}}$	16
E	Total specific energy	$\mathrm{erg\,g^{-1}}$	16
ϵ	Internal specific energy	$\mathrm{erg\,g^{-1}}$	16
$\vec{B}$	Total magnetic field	gauss	16
a	Magnetic stream function	$\mathrm{gauss\,cm^2}$	17
$\vec{J}$	Current density	$\mathrm{statampere\ cm^{-2}}$	25
I	Total current	statampere	25
$\vec{F}_{\mathrm{L}}$	Lorentz force	dyne	25
Σ	Disk surface density	$\mathrm{g\ cm^{-2}}$	26
H	Disk scale height	cm	26
Ω	Angular velocity	$\mathrm{s^{-1}}$	26
c_{s}	Sound speed	$\mathrm{cm\,s^{-1}}$	26
T	Temperature	K	26
ϑ	Viscosity	poise	26
$\dot{M}$	Mass accretion rate	$\mathrm{gm\ s^{-1}},\ \mathrm{M_\odot yr^{-1}}$	40
M_*	Mass of the central star	$\mathrm{kg},\ \mathrm{M_\odot}$	40

Symbol	Description	CGS Units	Page Ref.
$\alpha_{\rm v}$	Viscocity parameter		26
κ	Opacity	$\rm cm^2\,g^{-1}$	26
Q	Toomre parameter		28
$\Omega_{\rm epi}$	Epicylcic frequency	$\rm s^{-1}$	28
ν	Frequency	hertz (Hz)	29
$\mathcal{F}$	Total flux	erg $\rm cm^{-2}$ $\rm s^{-1}$	30
B_ν	Planck function		30
τ	Optical depth	cm	30
$M(\mathcal{T})$	Force multiplier		34
$\mathcal{T}$	Optical depth parameter		34
η	Line strength		34
$\hat{n}$	Unit vector along line of sight		34
α	Line force parameter (Gayley 1995)		34
$\bar{Q}, Q_0$	Line force constant (Gayley 1995)		34
k	Line force constant (Castor et al. 1975)		34
I_ν	Intensity	erg $\rm s^{-1}$ $\rm cm^{-2}$ $\rm sr^{-1}$ $\rm Hz^{-1}$	31
E_ν	Radiation energy density	erg $\rm cm^{-3}$ $\rm Hz^{-1}$	31
$\mathcal{P}_\nu$	Radiation pressure energy density	erg $\rm cm^{-3}$ $\rm Hz^{-1}$	31
χ_ν	Absorbtion coefficient	$\rm cm^{-1}$	32
j_ν	Emission coefficient	erg $\rm s^{-1}\,cm^{-3}$ $\rm sr^{-1}$ $\rm Hz^{-1}$	32

C

Acknowledgments

I am greatly indebted to my supervisor, Dr. Christian Fendt, for being extremely supportive and helpful right from the day I arrived in Heidelberg. He has been a constant source of energy and has always inspired me to work hard. He has not only improved my scientific vision but also played a vital role in developing my overall personality. He has always found time for me admist his very busy schedule. I would like to sincerely thank him for showing faith and patience in me during these three years.

I would also like to forward my thanks to my co-supervisor, Dr. Henrik Beuther. Henrik has always motivated me to strive harder to achieve the goal. He has always enligtened me with his inputs from the observational side. He has been very supportive especially in checking silly grammatical errors in the papers. I really enjoyed fruitful discussions with him during the Monday meetings and others in the group - Javier Rodon, Cassie Fallscheer, Tatiana Vasyunina, Yuan Wang and Jochen Tackenberg.

Next, I would like to thank Oliver Porth who has always been a supportive friend and a wonderful colleague to work with. I am greatly benefitted from his enthusiasm for science. I have learnt a great deal from the long discussions with him on the white boards and sometimes even on the walls. I would also like to forward my sincere thanks to Somayeh Sheikhnezami for having enlightening discussions.

I sincerely thank Prof. Mark Krumholz for his hospitality during my visit to Santa Cruz. I have learned a great deal from him during my short stay. I have also learned new numerical techniques from discussions with Rolf Kuiper.

Further, I would like to forward my thanks to Prof. Sandra Klevansky and Gesine Heinzelmann for all their support. I sincerely acknowledge the financial support from the Klaus Tschira Foundation and Graduate Academy during my PhD.

I could not have had better office mates and friends than Mario Gennaro, Mauricio Cisternas, Kasper Schmidt and Gisella de Rosa. I should thank them for bearing my occasional 'melodious' singing in the office and also the BBs. They have been a constant support for me particularly during my bad times. I will sincerely miss the trash talks and Gees's laughter during the table soccer matches. They have played a central role in helping me adopt to the culture during my stay in Germany. I will always cherish the wonderful time I had with them. I really enjoyed my time in Germany in the company of the IMPRS Generation 4 fellow mates.

In addition, I would also like to thank all my Indian friends Rahul Kannan, Bala Ramkumar, Siddhart Hegde, Sharanya Sur, Debarati Chatterjee, Jayanta Dutta, Chintan Trivedi who have been on my side through thick and thin. I have really enjoyed being with them specially during the Friday night outs and I will try my best to extent my sleep mode time.

I would like to forward my sincere thanks to Rahul Kannan, Sharanya Sur, Rolf Kuiper and Oliver Porth for helping me with language corrections for the thesis. I am also thankful to Thomas Gerner for translating the abstract. I also would like to acknowledge Min Fang and Javier Rodon for helping me with IDL and Linux installations.

I really cannot imagine myself here without the love and efforts from my family back in India. My mom and dad have always supported me in all walks of my life. I am also grateful to have blessings from my grand-parents.

D

List of Publications

Refereed Papers

[a]**Vaidya, Bhargav**; Fendt, Christian; Beuther, Henrik., 2009, The Astrophysical Journal, Volume 702, 567-579: *Accretion Disks Around Massive Stars: Hydrodynamic Structure, Stability, and Dust Sublimation*

Porth, Oliver; Fendt, Christian; Meliani, Zakaria; **Vaidya, Bhargav**., 2011, The Astrophysical Journal, Volume 737, 42: *Synchrotron Radiation of Self-collimating Relativistic Magnetohydrodynamic Jets*

[a]**Vaidya, Bhargav**; Fendt, Christian; Beuther, Henrik; Porth, Oliver., 2011, accepted for publication in The Astrophysical Journal: *Jet formation around young massive stars : Magnetohydrodynamics vs radiation pressure*. Preprint version available on http://arxiv.org/abs/1108.4924

Conference Proceedings

Fendt, Christian; **Vaidya, Bhargav**; Porth, Oliver; Nezami, Somayeh Sheikh., 2011, in: Jets at all Scales, Proceedings of the International Astronomical Union, IAU Symposium, Volume 275, 383-391: *MHD simulations of jet formation - protostellar jets & applications to AGN jets*

[a]Results from these papers are included in this thesis

E

Bibliography

Abbott, D. C. 1982, ApJ, 259, 282

Abramowicz, M. A., Czerny, B., Lasota, J. P., & Szuszkiewicz, E. 1988, ApJ, 332, 646

Akeson, R. L., Ciardi, D. R., van Belle, G. T., Creech-Eakman, M. J., & Lada, E. A. 2000, ApJ, 543, 313

Akeson, R. L., Walker, C. H., Wood, K., Eisner, J. A., Scire, E., Penprase, B., Ciardi, D. R., van Belle, G. T., Whitney, B., & Bjorkman, J. E. 2005, ApJ, 622, 440

Anderson, J. M., Li, Z.-Y., Krasnopolsky, R., & Blandford, R. D. 2003, ApJ, 590, L107

Andre, P., Montmerle, T., Feigelson, E. D., Stine, P. C., & Klein, K. 1988, ApJ, 335, 940

Arce, H. G., Shepherd, D., Gueth, F., Lee, C., Bachiller, R., Rosen, A., & Beuther, H. 2007, Protostars and Planets V, 245

Balbus, S. A. & Hawley, J. F. 1998, Reviews of Modern Physics, 70, 1

Bally, J. & Lada, C. J. 1983, ApJ, 265, 824

Bally, J. & Zinnecker, H. 2005, AJ, 129, 2281

Banerjee, R. & Pudritz, R. E. 2007, ApJ, 660, 479

Batchelor, G. 1967, An Introduction to Fluid Mechanics (Cambridge: Cambridge University Press)

Bell, K. R. & Lin, D. N. C. 1994, ApJ, 427, 987

Beuther, H. 2007, arXiv:0712.1109B

Beuther, H., Churchwell, E. B., McKee, C. F., & Tan, J. C. 2007, Protostars and Planets V, 165

Beuther, H., Schilke, P., & Gueth, F. 2004, ApJ, 608, 330

Beuther, H., Schilke, P., Gueth, F., McCaughrean, M., Andersen, M., Sridharan, T. K., & Menten, K. M. 2002a, A&A, 387, 931

Beuther, H., Schilke, P., Sridharan, T. K., Menten, K. M., Walmsley, C. M., & Wyrowski, F. 2002b, A&A, 383, 892

Beuther, H. & Shepherd, D. 2005, in Cores to Clusters: Star Formation with Next Generation Telescopes, ed. M. S. N. Kumar, M. Tafalla, & P. Caselli, 105–119

Beuther, H., Vlemmings, W. H. T., Rao, R., & van der Tak, F. F. S. 2010, ApJ, 724, L113

Bisnovatyi-Kogan, G. S. & Ruzmaikin, A. A. 1976, Ap&SS, 42, 401
Black, D. C. & Bodenheimer, P. 1975, ApJ, 199, 619
Blandford, R. D. 1976, MNRAS, 176, 465
Blandford, R. D. & Payne, D. G. 1982, MNRAS, 199, 883
Bogovalov, S. V. 1997, A&A, 323, 634
Bonnell, I. A. & Bate, M. R. 2006, MNRAS, 370, 488
Bonnell, I. A., Bate, M. R., Clarke, C. J., & Pringle, J. E. 1997, MNRAS, 285, 201
—. 2001, MNRAS, 323, 785
Bonnell, I. A. & Davies, M. B. 1998, MNRAS, 295, 691
Bonnell, I. A., Vine, S. G., & Bate, M. R. 2004, MNRAS, 349, 735
Boss, A. P. 1998, ApJ, 503, 923
—. 2000, ApJ, 536, L101
Bouvier, J., Alencar, S. H. P., Boutelier, T., Dougados, C., Balog, Z., Grankin, K., Hodgkin, S. T., Ibrahimov, M. A., Kun, M., Magakian, T. Y., & Pinte, C. 2007, A&A, 463, 1017
Brooks, K. J., Garay, G., Mardones, D., & Bronfman, L. 2003, ApJ, 594, L131
Carr, J. S. 1987, ApJ, 323, 170
Carrasco-González, C., Rodríguez, L. F., Anglada, G., Martí, J., Torrelles, J. M., & Osorio, M. 2010, Science, 330, 1209
Casse, F. & Keppens, R. 2002, ApJ, 581, 988
Castor, J. I. 2004, Radiation Hydrodynamics, ed. Castor, J. I.
Castor, J. I., Abbott, D. C., & Klein, R. I. 1975, ApJ, 195, 157
Cesaroni, R., Felli, M., Jenness, T., Neri, R., Olmi, L., Robberto, M., Testi, L., & Walmsley, C. M. 1999, A&A, 345, 949
Cesaroni, R., Galli, D., Lodato, G., Walmsley, C. M., & Zhang, Q. 2007, Protostars and Planets V, 197
Cesaroni, R., Neri, R., Olmi, L., Testi, L., Walmsley, C. M., & Hofner, P. 2005, A&A, 434, 1039
Chandrasekhar, S. 1960, Radiative transfer, ed. Chandrasekhar, S.
Clark, P. C., Klessen, R. S., Bonnell, I. A., & Smith, R. J. 2008, in Astronomical Society of the Pacific Conference Series, Vol. 387, Massive Star Formation: Observations Confront Theory, ed. H. Beuther, H. Linz, & T. Henning, 208–+
Collins, T. J. B., Helfer, H. L., & van Horn, H. M. 1998, ApJ, 502, 730
Courant, R., Friedrichs, K., & Lewy, H. 1928, Mathematische Annalen, 100, 32
D'Alessio, P., Canto, J., Calvet, N., & Lizano, S. 1998, ApJ, 500, 411
Davis, C. J., Varricatt, W. P., Todd, S. P., & Ramsay Howat, S. K. 2004, A&A, 425, 981
Del Popolo, A. & Ekşi, K. Y. 2002, MNRAS, 332, 485
Drew, J. E., Proga, D., & Stone, J. M. 1998, MNRAS, 296, L6+
Dullemond, C. P., Dominik, C., & Natta, A. 2001, ApJ, 560, 957

Dullemond, C. P. & Monnier, J. D. 2010, ARA&A, 48, 205
Durisen, R. H., Boss, A. P., Mayer, L., Nelson, A. F., Quinn, T., & Rice, W. K. M. 2007, Protostars and Planets V, 607
Edgar, R. & Clarke, C. 2003, MNRAS, 338, 962
Fallscheer, C., Beuther, H., Sauter, J., Wolf, S., & Zhang, Q. 2011, ApJ, 729, 66
Feldmeier, A. & Shlosman, I. 1999, ApJ, 526, 344
Fendt, C. 2006, ApJ, 651, 272
—. 2009, ApJ, 692, 346
Fendt, C. & Čemeljić, M. 2002, A&A, 395, 1045
Ferguson, J. W., Alexander, D. R., Allard, F., Barman, T., Bodnarik, J. G., Hauschildt, P. H., Heffner-Wong, A., & Tamanai, A. 2005, ApJ, 623, 585
Ferraro, V. C. A. 1937, MNRAS, 97, 458
Ferreira, J. 2002, in EAS Publications Series, Vol. 3, EAS Publications Series, ed. J. Bouvier & J.-P. Zahn, 229–277
Frank, J., King, A., & Raine, D. 1992, Accretion power in astrophysics. (Camb. Astrophys. Ser., Vol. 21,)
Gammie, C. F. 2001, ApJ, 553, 174
Garay, G., Brooks, K. J., Mardones, D., & Norris, R. P. 2003, ApJ, 587, 739
Gardiner, T. A. & Stone, J. M. 2005, Journal of Computational Physics, 205, 509
Gayley, K. G. 1995, ApJ, 454, 410
Gibb, A. G., Hoare, M. G., Little, L. T., & Wright, M. C. H. 2003, MNRAS, 339, 1011
Girart, J. M., Beltrán, M. T., Zhang, Q., Rao, R., & Estalella, R. 2009, Science, 324, 1408
Goldsmith, P. F., Snell, R. L., Hemeon-Heyer, M., & Langer, W. D. 1984, ApJ, 286, 599
Grave, J. M. C. & Kumar, M. S. N. 2009, A&A, 498, 147
Hachiya, M., Tajima, Y., & Fukue, J. 1998, PASJ, 50, 367
Hartigan, P., Edwards, S., & Pierson, R. 2004, ApJ, 609, 261
Hartigan, P. & Morse, J. 2007, ApJ, 660, 426
Hartigan, P., Morse, J. A., & Raymond, J. 1994, ApJ, 436, 125
Hartmann, L. 1998, Accretion Processes in Star Formation, ed. Hartmann, L.
Helling, C., Winters, J. M., & Sedlmayr, E. 2000, A&A, 358, 651
Hirth, G. A., Mundt, R., & Solf, J. 1994, A&A, 285, 929
Hofner, P., Cesaroni, R., Rodríguez, L. F., & Martí, J. 1999, A&A, 345, L43
Hofner, P., Delgado, H., Whitney, B., Churchwell, E., & Linz, H. 2002, ApJ, 579, L95
Hollenbach, D. J., Yorke, H. W., & Johnstone, D. 2000, Protostars and Planets IV, 401
Hosokawa, T. & Omukai, K. 2008, in Astronomical Society of the Pacific Conference Series, Vol. 387, Massive Star Formation: Observations Confront Theory, ed. H. Beuther, H. Linz, & T. Henning, 255

Hosokawa, T. & Omukai, K. 2009, ApJ, 691, 823
Hsu, W.-H., Hartmann, L., Heitsch, F., & Gómez, G. C. 2010, ApJ, 721, 1531
Iglesias, C. A. & Rogers, F. J. 1996, ApJ, 464, 943
Jijina, J. & Adams, F. C. 1996, ApJ, 462, 874
Kahn, F. D. 1974, A&A, 37, 149
Keto, E. 2007, ApJ, 666, 976
Keto, E. & Wood, K. 2006, ApJ, 637, 850
King, A. R., Pringle, J. E., & Livio, M. 2007, MNRAS, 376, 1740
Komissarov, S. S., Barkov, M. V., Vlahakis, N., & Königl, A. 2007, MNRAS, 380, 51
Krasnopolsky, R., Li, Z., & Blandford, R. 1999, ApJ, 526, 631
Krumholz, M. R., Klein, R. I., & McKee, C. F. 2007, ApJ, 656, 959
Krumholz, M. R., Klein, R. I., McKee, C. F., Offner, S. S. R., & Cunningham, A. J. 2009, Science, 323, 754
Krumholz, M. R., McKee, C. F., & Klein, R. I. 2005a, ApJ, 618, L33
—. 2005b, Nature, 438, 332
Kudritzki, R. & Puls, J. 2000, ARA&A, 38, 613
Kuiper, R., Klahr, H., Beuther, H., & Henning, T. 2010a, ApJ, 722, 1556
—. 2011, ApJ, 732, 20
Kuiper, R., Klahr, H., Dullemond, C., Kley, W., & Henning, T. 2010b, A&A, 511, A81+
Lang, K. R. 1992, Astrophysical Data I. Planets and Stars. (Astrophysical Data I. Planets and Stars, X, 937 pp. 33 figs.. Springer-Verlag Berlin Heidelberg New York)
Levermore, C. D. & Pomraning, G. C. 1981, ApJ, 248, 321
Lin, D. N. C. & Papaloizou, J. 1985, in Protostars and Planets II, ed. D. C. Black & M. S. Matthews, 981–1072
Lodato, G. & Rice, W. K. M. 2005, MNRAS, 358, 1489
López-Sepulcre, A., Cesaroni, R., & Walmsley, C. M. 2010, A&A, 517, A66+
López-Sepulcre, A., Codella, C., Cesaroni, R., Marcelino, N., & Walmsley, C. M. 2009, A&A, 499, 811
Lovelace, R. V. E. 1976, Nature, 262, 649
McKee, C. F. & Tan, J. C. 2003, ApJ, 585, 850
Menten, K. M. & van der Tak, F. F. S. 2004, A&A, 414, 289
Meru, F. & Bate, M. R. 2010, MNRAS, 406, 2279
Michel, F. C. 1969, ApJ, 158, 727
—. 1973, ApJ, 180, L133+
Mignone, A., Bodo, G., Massaglia, S., Matsakos, T., Tesileanu, O., Zanni, C., & Ferrari, A. 2007, ApJS, 170, 228
Monnier, J. D. & Millan-Gabet, R. 2002, ApJ, 579, 694

Montmerle, T. 2007, in IAU Symposium, Vol. 243, IAU Symposium, ed. J. Bouvier & I. Appenzeller, 23–30

Morfill, G. E. & Wood, J. A. 1989, Icarus, 82, 225

Moscadelli, L., Cesaroni, R., & Rioja, M. J. 2005, A&A, 438, 889

Mundy, L. G., Looney, L. W., & Welch, W. J. 2000, Protostars and Planets IV, 355

Murphy, G. C., Ferreira, J., & Zanni, C. 2010, A&A, 512, A82+

Murray, S. D., Castor, J. I., Klein, R. I., & McKee, C. F. 1994, ApJ, 435, 631

Nelson, A. F., Benz, W., & Ruzmaikina, T. V. 2000, ApJ, 529, 357

Norris, R. P., Byleveld, S. E., Diamond, P. J., Ellingsen, S. P., Ferris, R. H., Gough, R. G., Kesteven, M. J., McCulloch, P. M., Phillips, C. J., Reynolds, J. E., Tzioumis, A. K., Takahashi, Y., Troup, E. R., & Wellington, K. J. 1998, ApJ, 508, 275

Ossenkopf, V. & Henning, T. 1994, A&A, 291, 943

Ouyed, R., Clarke, D. A., & Pudritz, R. E. 2003, ApJ, 582, 292

Ouyed, R. & Pudritz, R. E. 1997, ApJ, 482, 712

Owocki, S. 2009, in American Institute of Physics Conference Series, Vol. 1171, American Institute of Physics Conference Series, ed. I. Hubeny, J. M. Stone, K. MacGregor, & K. Werner, 173–186

Parker, E. N. 1958, ApJ, 128, 664

Patel, N. A., Curiel, S., Sridharan, T. K., Zhang, Q., Hunter, T. R., Ho, P. T. P., Torrelles, J. M., Moran, J. M., Gómez, J. F., & Anglada, G. 2005, Nature, 437, 109

Pelletier, G. & Pudritz, R. E. 1992, ApJ, 394, 117

Pereyra, N. A., Kallman, T. R., & Blondin, J. M. 2000, ApJ, 532, 563

Pestalozzi, M. R., Elitzur, M., & Conway, J. E. 2009, A&A, 501, 999

Peters, T., Banerjee, R., Klessen, R. S., Mac Low, M.-M., Galván-Madrid, R., & Keto, E. R. 2010, ApJ, 711, 1017

Phillips, C. J., Norris, R. P., Ellingsen, S. P., & McCulloch, P. M. 1998, MNRAS, 300, 1131

Pickett, B. K., Durisen, R. H., Cassen, P., & Mejia, A. C. 2000, ApJ, 540, L95

Porth, O. & Fendt, C. 2010, ApJ, 709, 1100

Pravdo, S. H., Tsuboi, Y., Suzuki, Y., Thompson, T. J., & Rebull, L. 2009, ApJ, 690, 850

Proga, D. 2003, ApJ, 585, 406

Proga, D. & Kallman, T. R. 2004, ApJ, 616, 688

Proga, D., Stone, J. M., & Drew, J. E. 1998, MNRAS, 295, 595

—. 1999, MNRAS, 310, 476

Proga, D., Stone, J. M., & Kallman, T. R. 2000, ApJ, 543, 686

Pudritz, R. E., Ouyed, R., Fendt, C., & Brandenburg, A. 2007, Protostars and Planets V, 277

Puls, J., Springmann, U., & Lennon, M. 2000, A&AS, 141, 23

Rafikov, R. R. 2005, ApJ, 621, L69

Ray, T., Dougados, C., Bacciotti, F., Eislöffel, J., & Chrysostomou, A. 2007, Protostars and Planets V, 231

Rice, W. K. M., Armitage, P. J., Bate, M. R., & Bonnell, I. A. 2003, MNRAS, 339, 1025

Ruden, S. P. & Pollack, J. B. 1991, ApJ, 375, 740

Rybicki, G. B. & Hummer, D. G. 1978, ApJ, 219, 654

Sakurai, T. 1987, PASJ, 39, 821

Schatzman, E. 1962, Annales d'Astrophysique, 25, 18

Schreyer, K., Semenov, D., Henning, T., & Forbrich, J. 2006, ApJ, 637, L129

Schulz, A., Henkel, C., Beckmann, U., Kaseman, C., Schneider, G., Nyman, L. A., Persson, G., Gunnarsson, L. G., & Delgado, G. 1995, A&A, 295, 183

Semenov, D., Henning, T., Helling, C., Ilgner, M., & Sedlmayr, E. 2003, A&A, 410, 611

Shakura, N. I. & Sunyaev, R. A. 1973, A&A, 24, 337

—. 1976, MNRAS, 175, 613

Shakura, N. I. & Syunyaev, R. A. 1973, A&A, 24, 337

Shepherd, D. S. & Churchwell, E. 1996, ApJ, 457, 267

Shepherd, D. S., Claussen, M. J., & Kurtz, S. E. 2001, Science, 292, 1513

Shu, F. 1991, Physics of Astrophysics: Volume I Radiation, ed. Shu, F. (University Science Books)

Snell, R. L., Scoville, N. Z., Sanders, D. B., & Erickson, N. R. 1984, ApJ, 284, 176

Spruit, H. C. 1996, ArXiv Astrophysics e-prints

Spruit, H. C. 2010, in Lecture Notes in Physics, Berlin Springer Verlag, Vol. 794, Lecture Notes in Physics, Berlin Springer Verlag, ed. T. Belloni, 233–+

Sridharan, T. K., Williams, S. J., & Fuller, G. A. 2005, ApJ, 631, L73

Stahler, S. W. & Palla, F. 2005, The Formation of Stars (The Formation of Stars, by Steven W. Stahler, Francesco Palla, pp. 865. ISBN 3-527-40559-3. Wiley-VCH , January 2005.)

Stanke, T., McCaughrean, M. J., & Zinnecker, H. 2002, A&A, 392, 239

Stepinski, T. F. 1998, Icarus, 132, 100

Stepinski, T. F., Reyes-Ruiz, M., & Vanhala, H. A. T. 1993, Icarus, 106, 77

Toomre, A. 1964, ApJ, 139, 1217

Toro, E. F., Spruce, M., & Speares, W. 1994, Shock Waves, 4, 25

Torrelles, J. M., Gómez, J. F., Garay, G., Rodríguez, L. F., Curiel, S., Cohen, R. J., & Ho, P. T. P. 1998, ApJ, 509, 262

Torrelles, J. M., Patel, N. A., Curiel, S., Estalella, R., Gómez, J. F., Rodríguez, L. F., Cantó, J., Anglada, G., Vlemmings, W., Garay, G., Raga, A. C., & Ho, P. T. P. 2011, MNRAS, 410, 627

Turner, N. J., Quataert, E., & Yorke, H. W. 2007, ApJ, 662, 1052

Vaidya, B., Fendt, C., & Beuther, H. 2009, ApJ, 702, 567

Vaidya, B., Fendt, C., Beuther, H., & Porth, O. 2011, ArXiv e-prints

Vlemmings, W. H. T. 2008, A&A, 484, 773

Vlemmings, W. H. T., Surcis, G., Torstensson, K. J. E., & van Langevelde, H. J. 2010, MNRAS, 404, 134

Weber, E. J. & Davis, Jr., L. 1967, ApJ, 148, 217

Wheelwright, H. E., Oudmaijer, R. D., de Wit, W. J., Hoare, M. G., Lumsden, S. L., & Urquhart, J. S. 2010, MNRAS, 408, 1840

Whitney, B. A., Wood, K., Bjorkman, J. E., & Cohen, M. 2003, ApJ, 598, 1079

Wolf, S., Schegerer, A., Beuther, H., Padgett, D. L., & Stapelfeldt, K. R. 2008, ApJ, 674, L101

Wolfire, M. G. & Cassinelli, J. P. 1987, ApJ, 319, 850

Wright, M. C. H., Plambeck, R. L., Mundy, L. G., & Looney, L. W. 1995, ApJ, 455, L185+

Wu, Y., Wei, Y., Zhao, M., Shi, Y., Yu, W., Qin, S., & Huang, M. 2004, A&A, 426, 503

Yorke, H. W. 2004, in IAU Symposium, Vol. 221, Star Formation at High Angular Resolution, ed. M. G. Burton, R. Jayawardhana, & T. L. Bourke, 141

Yorke, H. W. & Bodenheimer, P. 1999, ApJ, 525, 330

Yorke, H. W. & Sonnhalter, C. 2002, ApJ, 569, 846

Zanni, C., Ferrari, A., Rosner, R., Bodo, G., & Massaglia, S. 2007, A&A, 469, 811

Zhang, Q. 2005, in IAU Symposium, Vol. 227, Massive Star Birth: A Crossroads of Astrophysics, ed. R. Cesaroni, M. Felli, E. Churchwell, & M. Walmsley, 135–144

Zhang, Q., Hunter, T. R., Brand, J., Sridharan, T. K., Cesaroni, R., Molinari, S., Wang, J., & Kramer, M. 2005, ApJ, 625, 864

Zhang, Q., Hunter, T. R., & Sridharan, T. K. 1998, ApJ, 505, L151

Zinnecker, H. & Yorke, H. W. 2007, ARA&A, 45, 481